# Investigation of the Multiscale Constitutive Behavior of Ferroelectric Materials Using Advanced Diffraction Techniques

Thesis by

Robert C. Rogan

In Partial Fulfillment of the Requirements

for the Degree of

Doctor of Philosophy

California Institute of Technology

Pasadena, California

2004

(Defended May 14, 2004)

## Acknowledgments

Thanks to my advisor, Dr. Ersan Üstündag, for constant support and motivation in completing the work which led to this thesis. I would also like to thank the multitude of national laboratory scientists and postdocs who were subjected to long days, late nights, and early morning phone calls whenever I came to perform an experiment. Special thanks to Mark Daymond, Bjørn Clausen, Nobumichi Tamura, and Ulrich Lienert, without whose continual input I would most certainly have not completed this thesis. I would also like to thank Mike Vondrus for saving more than a few of my experiments at the last minute with an oddly shaped chunk of aluminum. The rest of my research group has been instrumental in obtaining the data presented in this thesis, and without their energy, insight, and tolerance these experiments would not have worked. Can Aydiner, Geoff Swift, Michal Brown, Seung-Yub Lee, Greg Welsh, and Maziar Motahari, I am indebted to you all.

I would also like to thank my college research supervisors Dr. Hong Ding and Dr. James Richardson Jr., who gave me my first taste of real science research, and my unofficial college advisor, Dr. Michael Graf, whose second year physics course set me on the path to graduate school, and who was also very frank about what I could expect when I got there. He was right about everything. A special thanks to Judy Lebryk, the best teacher I've ever had, who insisted that I learn how to write properly even if I was going to be a scientist. I fear she would have more than a few red marks to add to this text.

I would like to thank my family, who has supported me my whole life and still has absolutely no idea what I do. Last, but foremost, my soon-to-be-wife Stephanie; without you none of this would have been possible.

## Abstract

Ferroelectric ceramics are widely used in a diverse set of devices including sensors, actuators, and transducers. The technological importance of ferroelectrics originates from their large electromechanical coupling. Ferroelectric materials exhibit a complicated behavior in response to both electrical and mechanical loads which produce large internal stresses that eventually lead to failure. Efforts to model and predict the behavior of ferroelectrics have been hindered by the lack of suitable constitutive relations that accurately describe the electromechanical response of these materials. While many measurements have been conducted on the macroscopic response of single-crystals or polycrystals, multiaxial (and multiscale) data about the *in situ* internal strain and texture response of these materials is lacking; this information is critical to the development of accurate models, and diffraction techniques which directly measure internal crystal strains and material texture are aptly suited to supply it.

A neutron diffraction technique was employed which allowed for the simultaneous measurement of material texture and lattice strains in directions parallel and transverse to an applied mechanical load. By comparing the behaviors of single-phase tetragonal, single-phase rhombohedral, and dual-phase morphotropic compositions, information concerning mechanics of average *macroscopic* behavior was inferred. In an effort to probe more of the multiaxial constitutive behavior, a high-energy X-ray diffraction technique was employed. Using transmission geometry and a 2-D image plate detector, 36 different directions of sample behavior were measured simultaneously. Polychromatic scanning X-ray microdiffraction was used to investigate the *microscale* three-dimensional strain tensor in single-crystals. One investigation yielded the first ever

direct measurement of the tri-axial strain fields associated with single domain walls in ferroelectrics. The second investigation recorded the domain switching mechanisms activated to accommodate indentation-induced fracture stresses. Finally, 3-D XRD was used to probe the *mesoscale* constitutive behavior of single, embedded grains of $BaTiO_3$ within a polycrystalline matrix.

The experimental methods described in this thesis provide access to *two-dimensional and three-dimensional multiaxial* constitutive strain behavior in ferroelectrics for each of the *microscopic, mesoscopic, and macroscopic* length scales. Results from each of these length scales will provide critical data for models attempting to accurately describe the behavior of ferroelectric materials.

# Contents

# Chapter 1

# Introduction

## 1.0 Ferroelectric Materials and Their Constitutive Behavior

Ferroelectric ceramics are widely used in a diverse set of devices including sensors, actuators, transducers, and ultrasonic motors [1]. The technological importance of ferroelectrics originates from their large electromechanical coupling and their ability to be easily manufactured into complex geometries via powder processing and other advanced fabrication techniques. The phenomena of ferroelectricity, ferroelasticity and piezoelectricity are here presented with reference to the commonly found perovskite crystal structure [2]. What will become clear in this discussion is that the unusual electromechanical macroscopic properties found in these materials can only be understood through an appreciation of the physical mechanisms operating in a multiaxial fashion at a range of microstructure dependent length scales. The interaction of anistoropic mechanisms at multiple length scales leads to complicated behavior dependent on the specific application of external forces and the microstructure of the specimen in question.

Figure 1-1 illustrates the perovskite structure for many ferroelectrics including $BaTiO_3$ (BTO) and $Pb(Zr_xTi_{1-x})O_3$ (PZT). Here, only the tetragonal structure is discussed, however orthorhombic, rhombohedral, and monoclinic crystal structures are also known to exist in these materials [2-6]. Above the Curie temperature $T_c$, the material

is paraelectric with a cubic, centro-symmetric structure. As it is cooled below $T_c$ it undergoes a phase transformation from the cubic to tetragonal phase. Notice that the previously centered Ti ion has been displaced towards one face of the tetragonal cell. The direction of this ion displacement is also the direction of the spontaneous polarization of the material, $P_s$, and is aligned with the *c* axis of the tetragonal cell (formerly the [001] cubic direction). Below $T_c$ the material is both piezoelectric and ferroelectric, and the piezoelectric properties of the crystal are aligned with the spontaneous polarization direction. Rhombohedral phase ferroelectrics possess ion displacements and polarizations along the [111] cubic direction, and orthorhombic phase along the [110].

The piezoelectric, dielectric and elastic responses of the tetragonal material are illustrated on the first row of Fig. 1-1. If a small electric field is applied in the direction of the spontaneous polarization, then the polarization will increase (dielectric effect) together with strain (piezoelectric effect). Alternatively, if a compressive stress is aligned with the spontaneous polarization direction, then the strain will decrease (elastic effect) and the polarization will decrease (piezoelectric effect).

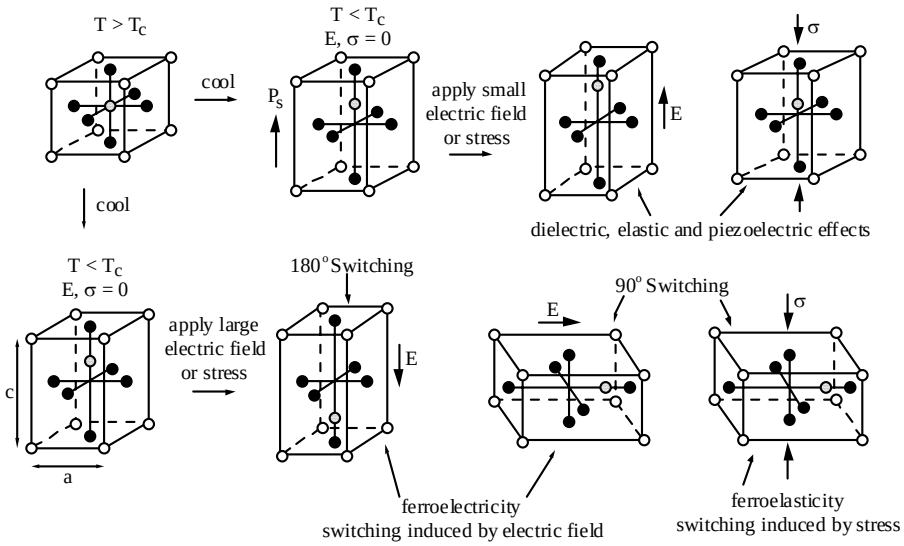


**Figure 1-1**. The perovskite crystal structure common to many ferroelectric ceramics. For BTO the white ions at the corners are $Ba^{+2}$ ions, the black ions on the faces are $O^{-2}$ ions and the central ion is $Ti^{+4}$. The top set of figures illustrates the phase change through the Curie temperature, the spontaneous polarization, and the linear response of the crystal. The bottom set of figures illustrates the spontaneous shape change of the crystal, and 180˚ and 90˚ switching due to applied electric field or stress. The magnitudes of the ion displacements have been exaggerated for clarity. Courtesy of C. Landis

The ferroelectric response of the material is illustrated on the second row of Fig. 1-1 where ferroelastic switching has been differentiated from ferroelectric switching [2]. Note that a change in spontaneous strain, i.e., the orientation of the *c* axis, accompanies the polarization change during 90° switching but not during 180° switching. For the tetragonal structure shown in Fig. 1-1 there are four possible 90° switches that can be driven by combinations of stress and electric field and one 180° switch that can be driven only by electric field. The middle two schematics on the second row of Fig. 1-1 illustrate 180° and 90° switching induced by applied electric field alone. The last schematic illustrates 90° switching due to the application of a compressive stress parallel to the polarization direction. Note that for this compressive stress a switch to any one of the four energetically equivalent 90° domain variants can be activated.

A thorough understanding of the electromechanical mechanisms illustrated in Fig. 1-1, including linear piezoelectricity and non-linear switching, is necessary for the explanation of most of the macroscopic phenomena observed in ferroelectrics. However, the depiction of switching that is obtained from the consideration of a single lattice cell is deceptively simplified. In real single crystals (including single grains of a polycrystal), there exist multiple domain variants separated by domain walls formed by twin boundaries [2-4]. Across a domain wall the spontaneous polarization is discontinuous. Switching of a domain is not a homogenous process as the single unit cell depiction would suggest, but rather proceeds as a result of domain wall motion which converts one domain variant to another [2-4, 7]. Even within a single crystal different concentrations of the six possible domain variants can coexist such that the irreversible (or remanent) polarization and hence the piezoelectric properties of the crystal can be oriented in any of these six directions through application of a large electric field to induce domain switching; this process is called “poling.” The ability of ferroelectric single crystals to be poled in certain directions is of significant technological importance, as it allows for the piezoelectric response to be oriented for use in applications. Successful poling of a single crystal depends on the relative concentrations of the initial domain variants, crystal purity (any impurities can impede domain wall motion), and the direction and strength of the applied electric field.

Let us now consider macroscopic phenomena that result from microscopic, i.e., domain level, mechanisms averaged over volumes which are associated with the polycrystals used in most ferroelectric devices. When the material is cooled below the Curie temperature spontaneous polarization, spontaneous strain and piezoelectricity must

exist at the individual domain level. However, when averaged over all possible orientations of the domains and grains within the polycrystal, the macroscopic polarization, strain, and piezoelectric effect of the ceramic are initially zero. In order to make the polycrystal piezoelectric, and therefore useful in actuator or sensor applications, a strong electric field must be applied. In the case of a polycrystal, the initially homogenous orientation distribution of the ceramic implies that the specimen may be poled in an arbitrary direction.

As the electric field is applied, domain walls move such that domains aligned with the field grow at the expense of domains opposing the field. However, the randomized grain and domain configuration established during preparation limits the possible orientations of any domain variant relative to the externally applied field. Thus during poling, domains will attempt to switch their polarizations into orientations aligned with the macroscopic field, but the fixed grain structure may severely limit switching ability [1]. The poling process, then, occurs gradually and over a range of applied electric fields due to the variation in local electromechanical boundary conditions (intergranular constraints). In certain grain orientations, domains may switch temporarily to minimize the total energy during the application of electric field. After the field is removed, some domain walls will move back towards their original positions, due to residual stresses and local electric fields in the material. However, this reverse switching is incomplete and there exists a net polarization, strain and piezoelectric effect aligned in the direction of the original applied electric field. The material is now “poled” and suitable for use as an actuator or sensor.

Many of the most industrially successful ferroelectric compositions possess grains of multiple crystal structures, such as the rhombohedral-tetragonal phase combination found in the morphotropic region of the PZT phase diagram [3]. As such, ferroelectrics can exhibit a complicated behavior in response to both electrical and mechanical loads which produce large internal stresses that eventually lead to failure. Efforts to model and predict the behavior of ferroelectrics have often been hindered by the lack of suitable constitutive relations that accurately describe the electromechanical response of these materials. While many measurements have been conducted on the *macroscopic* response of large single crystals or polycrystals, there is lack of multiaxial (and multiscale) data about the *in situ* internal strain and texture response of these materials; this information is critical to the development of accurate models, and it can only be provided by diffraction techniques which directly measure internal crystal strains.

### 1.1 Review of Diffraction Techniques Applied to the Study of Ferroelectrics

The formulation of robust models for ferroelectric materials requires knowledge of their crystallographic behavior under applied mechanical and electrical loading. Specifically, it is desirable to obtain, as a function of applied electromechanical loads, quantitative data of the microscopic strain states which are functions both of single crystal elastic properties and domain switching. Many investigations of PZT's (and other ferroelastic and ferroelectric materials) have been undertaken to study the macroscopic stress-strain response via traditional mechanical testing (too many to recount here, but see [1] for a review, and also [8-11]). While macroscopic measurements have been invaluable for outlining the behavior of multiphase materials and isolating technologically useful

compositions, they offer no insight into the crystallographic behavior which is valuable to the modeling community. X-ray studies have been particularly useful in ascertaining crystal structure and observing the texture effects of domain switching, both *in situ* and *ex situ* [12-17]. Given the wide variety of ferroelectric materials available today, a complete review of all X-ray diffraction studies concerning ferroelectrics is outside the scope of this introduction. Instead a brief tour of studies on certain concentrations is given below.

Fernandes *et al.* used high resolution synchrotron diffraction to analyze the proportion of rhombohedral and tetragonal phases present in morphotropic compositions of PZT processed under various conditions [14]. Floquet and colleagues used X-ray diffraction data of $BaTiO_3$ to construct a model for domain wall structure [18]. Numerous important studies by Noheda *et al*. established the presence of a third, monoclinic phase in the morphotropic region of the PZT diagram for sub-room temperatures [6, 19]. Additional novel phase transitions under several GPa of hydrostatic pressure were observed using angle-dispersive X-ray diffraction by Rouquette *et al.* [20]. Electric field induced phase transitions have also been observed for the relaxor type ferroelectric 92% $Pb(Zn_{1/3}Nb_{2/3})O_3$ – 8% $PbTiO_3$, in addition to a correlation between *in situ* crystallographic strain and macroscopically measured strain [21]. Several authors used X-ray diffraction to measure the ferroelectric and piezoelectric crystallographic strains in PZT materials of rhombohedral, tetragonal, and morhpotropic (dual-phase) microstructures induced by application of electric fields [12, 13, 15-17, 22]. Recently, Glkazounov and Hoffmann employed X-ray techniques to study ceramic fracture behaviors in ferroelectrics subjected to cyclic mechanical loads [23, 24].

The majority of the existing literature presents data obtained using  radiation on the order of ~8 keV, or the energy of Cu *Kα* (though exceptions such as the 67 keV energy used in [25] are noted) .  Because many of the most important ferroelectrics contain significant quantities of heavy elements such as Pb and Ba, these XRD experiments are confined to near-surface regions due to the limited penetration depth achievable with low-energy X-rays.  For an X-ray beam incidence angle normal to the sample surface, the penetration of Cu *Kα* radiation  is around 5 μm in PZT (anywhere from 1-5 grains of depth), and this value drops sharply as the incident angle is moved to the ranges of standard reflection measurements.  Noheda reports that even for 18 keV radiation impacting 92% $Pb(Zn_{1/3}Nb_{2/3})O_3$ – 8% $PbTiO_3$, only a 1 μm penetration depth is achieved at scattering angles relevant for obtaining structural data in reflection geometry [25].  Given that the boundary conditions for grains at or near a free surface will be very different than those confined in the bulk, resulting in inhomogenous strains in these regions (“skin effect”) [25], it is questionable that results obtained using low-energy X-rays can be truly correlated to the macroscopic material response.

Neutron diffraction, on the other hand, offers much deeper penetration and superior grain averaging in heavy element materials.  Neutron diffraction is thus an ideal probe of the bulk crystallographic behavior of ferroelectrics, but presently work using this technique has largely concentrated on probing the temperature–composition–structure relationships to obtain a clear understanding of the nature of the various phase transitions.  Glazer and Mabud were the first to use neutron diffraction to obtain the structures for the tetragonal, high- and low-temperature rhombohedral phases of the PZT system [26, 27].  In later years, numerous authors have used neutron diffraction to study

the specific distortions in space groups corresponding to various compositions of PZT and other ferroelectric materials (for example [28-30]). Zaou *et al*. [31] and Misture *et al*. [32] both used neutron diffraction to determine the electrostrictive coefficients of Pb-Mg-Nb-O based relaxor materials. A neutron diffraction study [33] is also noted for the investigation the ferroelastic behavior of a single crystal $LaNbO_4$ under compressive stress. Although this study did provide valuable insight about the crystallographic domain switching mechanism in $LaNbO_4$, it did not involve a polycrystalline material and, therefore, could not probe the interactions between various domains and grain orientations. A study of the ferroelastic response of non-ferroelectric zirconia using neutron diffraction was performed by Cain *et al.* [34], and illuminated the possibility of applying the technique to ferroelectrics.

### 1.2 Motivation for Thesis Work and Roadmap of Experiments

In order to probe the bulk behavior of ferroelectric materials, the penetration power of high-energy synchrotron X-rays (> 60 keV) or neutrons are needed. In addition, it is desirable to obtain diffraction data from multiple orientations to measure more thorough coverage of the anisotropic material behavior. This last distinction is critical, as ferroelectrics become anisotropic after the poling process. Consequently, lattice parameters measured parallel to the poling field will differ from those measured normal to the field [35]. In other words, lattice strain information from a single direction does not provide a complete measurement of the constitutive behavior of ferroelectrics. Most X-ray instruments usually measure lattice parameters from a single scattering direction, and thus ignore much desirable information. As of this time, no known studies have

addressed the simultaneous measurement of multiple directions of strain responses in ferroelectrics using diffraction. The primary focus of the work presented in this thesis is the development of *multiaxial* diffraction techniques for measuring the *in situ* constitutive strain behavior in ferroelectrics at multiple length scales.

While there is considerable information available in the literature concerning the bulk average behavior of ferroelectric materials (as outlined in the studies above), there is a relative dirth of information from the mesoscale (a few grains) and microscale (single crystal). In the case of PZT materials, this is due to the extreme difficulty of growing single crystals (none of appreciable size has ever been created). For other materials such as BTO, single crystals can be grown to large dimensions. Several methods for qualitatively studying the micromechanics of single crystal ferroelectrics will be reviewed in Chapter 4, but none provide a direct method of measuring the strain states which govern the constitutive behavior. In the case of mesoscale studies, experimental techniques for measuring strain accurately are even more limited, as isolating independent grain behavior from a bulk specimen is difficult. The secondary focus of this thesis work will emphasize the development of techniques to capture multiaxial strain data at *multiple length scales*. Through the application of several novel diffraction techniques, significant inroads have been made into studying ferroelectric constitutive behavior in the macroscopic, mesoscopic, and microscopic arenas. The common theme among all presented experiments is the ability to observe multiple dimensions of behavior simultaneously, and the differences in the techniques outline specialized methods of examining different length scales.

The first experiments presented in Chapter 2 are studies of the *in situ* response of several PZT compositions to mechanical stress [35]. A neutron diffraction technique was employed which allowed for the simultaneous measurement of material texture (domain switching) and crystal lattice strains in directions parallel and transverse to the loading axis . By comparing the behaviors of single-phase tetragonal, single-phase rhombohedral, and dual-phase morphotropic compositions, information concerning material micromechanics may be inferred. While neutron diffraction offers superior penetration depths in PZTs, the relatively long acquisition times necessary to capture accurate data are prohibitive to performing a complete probing of the multiaxial response through sample rotations. Due to the geometrical limitations of the loading apparatus and detector geometry, significant strain and texture information is only observed in one detector bank. Thus neutron diffraction offers only a selected probing of constitutive behavior, essentially using two separate one-dimensional probes. The experiments in Chapter 2 thus provide *limited two-dimensional* constitutive strain data for the *macroscopic* scale.

In an effort to probe more of the multiaxial constitutive behavior (e.g., the effects of grain orientation on ferroelectric response), a high-energy X-ray diffraction experiment will be presented in Chapter 3. A complicated PZT-based relaxor material was chosen for this work in order to present ample opportunity to take advantage of the multiaxial data. Using transmission geometry and a 2-D digital image plate detector, complete Debye rings could be captured representing the crystallographic state of all grains lying in a sample plane. By creating “virtual detectors”, these Debye rings could be broken down to study 36 different directions of sample behavior simultaneously; a

considerable increase over the two directions available for neutron diffraction experiments. The specimen was then poled *in situ* using high electric fields, and subsequently cycled through positive and negative electric fields. The technique employed in Chapter 3 yields *fully two-dimensional* constitutive strain data at the *macroscopic* scale.

Chapter 4 focuses on a polychromatic X-ray diffraction technique capable of measuring the full three-dimensional strain tensor in single crystal and large grained materials. Experiments in this chapter used single crystal specimens of BTO. One investigation yielded the first ever direct measurement of the tri-axial strain fields associated with single domain walls in ferroelectrics. The second investigation outlines the domain switching mechanisms activated to accommodate indentation-induced fracture stresses. The experiments described in Chapter 4 yield *fully three-dimensional* constitutive strain data at the *microscopic* scale.

Chapters 2 and 3 deal with *two-dimensional* multiaxial ferroelectric constitutive behavior on a *macroscopic* scale (or polycrystalline average). Chapter 4 presents data from a completely *microscopic* scale (or single domain variant behavior). In the "Future Work" section of Chapter 5, a newly developed high-energy X-ray technique capable of probing the constitutive response of single grains within a polycrystal (*mesoscale*) will be described. Preliminary results for the electrical loading of polycrystalline BTO will be reported. Isolating the strain and domain variant information within a single, embedded grain in the polycrystal was possible with this technique. The technique described in Chapter 5 will bridge the gap between the macro- and micro-scales, yielding *fully three-dimensional* constitutive strain data at the *mesoscopic* scale. Taken as a whole, the

experimental methods described in this thesis provide access to *two-dimensional and three-dimensional multiaxial* constitutive strain behavior in ferroelectrics for each of the *microscopic, mesoscopic, and macroscopic* length scales.

**Chapter References**


1. Bhattacharyta, K. and G. Ravichandran, *Ferroelectric Perovskites for Electromechanical Actuation.* Acta Materialia, 2003. **51**: p. 5941-5960.

2. Jona, F. and G. Shirane, *Ferroelectric Crystals*. 1962, New York: Pergamon Press.

3. Jaffe, B., W.R. Cook, and H. Jaffe, *Piezoelectric Ceramics*. 1971, London: Academic Press.

4. Lines, M.E. and A.M. Glass, *Principles and Applications of Ferroelectrics and Related Materials*. 1977, New York: Oxford University Press.

5. Cross, L.E., *Ferroelectric Ceramics: Tailoring Properties for Specific Applications*, in *Ferroelectric Ceramics*, N. Setter and E.L. Colla, Editors. 1993. p. 1-86.

6. Noheda, B., J.A. Gonzalo, L.E. Cross, R. Guo, S.-E. Park, D.E. Cox, and G. Shirane, *Tetragonal-to-Monoclinic Phase Transition in a Ferroelectric Perovskite: The Structure of $PbZr_{0.52}Ti_{0.48}O_3$.* Physical Review B, 2000. **61**(13): p. 8687-8695.

7. Munoz-Saldana, J., G.A. Schneider, and L.M. Eng, *Stress Induced Movement of Ferroelastic Domain Walls in $BaTiO_3$ Single Crystals Evaluated by Scanning Force Microscopy.* Surface Science, 2001. **480**(1-2): p. L402-L410.

8. Calderon-Moreno, J.M., *Stress Induced Domain Switching of PZT in Compression Tests.* Materials Science and Engineering a-Structural Materials Properties Microstructure and Processing, 2001. **315**(1-2): p. 227-230.

9. Calderon-Moreno, J.M., *Stress-Induced Domain Switching of PZT Subjected to Cyclic Uniaxial Compression*, in *Euro Ceramics Vii, Pt 1-3*. 2002. p. 1445-1448.

10. Huber, J.E., N.A. Fleck, C.M. Landis, and R.M. McMeeking, *A Constitutive Model for Ferroelectric Polycrystals.* Journal of the Mechanics and Physics of Solids, 1999. **47**(8): p. 1663-1697.

11. Hwang, S.C., C.S. Lynch, and R.M. McMeeking, *Ferro Electric/Ferroelastic Interactions and a Polarization Switching Model.* Acta Metallurgica Et Materialia, 1995. **43**(5): p. 2073-2084.

12. Bedoya, C., C. Muller, J.L. Baudour, V. Madigou, M. Anne, and M. Roubin, *Sr-doped PbZr1-xTixO3 Ceramic: Structural Study and Field- Induced Reorientation of Ferroelectric Domains.* Materials Science and Engineering B-Solid State Materials for Advanced Technology, 2000. **75**(1): p. 43-52.

13. Endriss, A., M. Hammer, M.J. Hoffmann, A. Kolleck, and G.A. Schneider, *Microscopic and Macroscopic Ferroelectric-Ferroelastic and Piezoelectric Behavior of PZT Ceramics.* Journal of the European Ceramic Society, 1999. **19**(6-7): p. 1229-1231.

14. Fernandes, J.C., D.A. Hall, M.R. Cockburn, and G.N. Greaves, *Phase Coexistence in PZT Ceramic Powders.* Nuclear Instruments & Methods in Physics Research Section B- Beam Interactions with Materials and Atoms, 1995. **97**(1-4): p. 137-141.

15. Ogawa, T. and K. Nakamura, *Poling Field Dependence of Ferroelectric Properties and Crystal Orientation in Rhombohedral Lead Zirconate Titanate Ceramics.* Japanese Journal of Applied Physics Part 1-Regular Papers Short Notes & Review Papers, 1998. **37**(9B): p. 5241-5245.

16. Tanaka, K., Y. Akiniwa, Y. Sakaida, and H. Kimachi, *Lattice Strain and Domain Switching Induced in Tetragonal PZT by Poling and Mechanical Loading.* JSME International Journal, 2000. **43**(4): p. 351-357.

17. Tsurumi, T., Y. Kumano, N. Ikeda, N. Ohashi, and O. Fukunaga, *XRD Measurement of 90 Degrees Domain Reorientation and Domain Contribution to the Electric-Field-Induced Strain in PZT Ceramics*, in *Electroceramics in Japan I*. 1999. p. 73-79.

18. Floquet, N., C.M. Valot, M.T. Mesnier, J.C. Niepce, L. Normand, A. Thorel, and R. Kilaas, *Ferroelectric Domain Walls in $BaTiO_3$: Fingerprints in XRPD Diagrams and Quantitative HRTEM Image Analysis.* Journal De Physique Iii, 1997. **7**(6): p. 1105-1128.

19. Noheda, B., D.E. Cox, G. Shirane, R. Guo, B. Jones, and L.E. Cross, *Stability of the Monoclinic Phase in the Ferroelectric Perovskite $PbZr_{1-x}Ti_xO_3$.* Physical Review B, 2000. **63**.

20. Rouquette, J., V. Bornand, J. Haines, P. Papet, and F. Gorelli, *Structural Trnsformation and Pressure-Induced Phase Transition in PZT.* Integrated Ferroelectrics, 2002. **48**: p. 53-58.

21. Durbin, M.K., E.W. Jacobs, J.C. Hicks, and S.-E. Park, *In Situ X-ray Diffraction Study of an Electric Field Induced Phase Transition in the Single Crystal Relaxor Ferroelectric 92%$PbZn_{1/3}Nb_{2/3}O_3$-8%$PbTiO_3$.* Applied Physics Letters, 1999. **74**(19): p. 2848-2850.

22. Reszat, J.T., A.E. Glazounov, and M.J. Hoffmann, *Analysis of Intrinsic Lattice Deformation in PZT-Ceramics of Different Compositions.* Journal of the European Ceramic Society, 2001. **21**(10-11): p. 1349-1352.

23. Glazounov, A.E. and M.J. Hoffmann, *Investigation of Domain Switching in Fractured Ferroelectric Ceramics by using Imaging of X-ray Diffraction.* Journal of the European Ceramic Society, 2001. **21**: p. 1417-1420.

24. Glazounov, A.E., H. Kungl, J.T. Reszat, M.J. Hoffmann, A. Kolleck, G.A. Schneider, and Wroblewski, *Contribution from Ferroelastic Domain Switching Detected Using X-ray Diffraction to R-Curves in Lead Zirconate Titanate Ceramics.* Journal of the American Ceramic Society, 2001. **84**(12): p. 2921-2929.

25. Noheda, B., D.E. Cox, G. Shirane, S.-E. Park, L.E. Cross, and Z. Zhong, *Polarization Rotation viea a Monoclinic Phase in the Piezoelectric 92%$PbZn_{1/3}Nb_{2/3}O_3$-8%$PbTiO_3$.* Physical Review Letters, 2001. **86**(17): p. 3891-3894.

26. Glazer, A.M., S.A. Mabud, and R. Clarke, *Powder Profile Refinement of Lead Zirconate Titanate at Several Temperatures.1. Pbzr0.9ti0.1o3.* Acta Crystallographica Section B-Structural Science, 1978. **34**(APR): p. 1060-1065.

27. Glazer, A.M. and S.A. Mabud, *Powder Profile Refinement of Lead Zirconate Titanate at Several Temperatures. 2. Pure Pbtio3.* Acta Crystallographica Section B-Structural Science, 1978. **34**(APR): p. 1065-1070.

28. Wilkinson, A.P., J. Xu, S. Pattanaik, and S.J.L. Billinge, *Neutron Scattering Studies of Compositional Heterogeneity in Sol-Gel Processed Lead Zirconate Titanates.* Chemistry of Materials, 1998. **10**(11): p. 3611-3619.

29. Frantti, J., S. Ivanov, J. Lappalainen, S. Eriksson, V. Lantto, S. Nishio, M. Kakihana, and H. Rundlof, *Local and Average Structure of Lead Titanate Based Ceramics.* Ferroelectrics, 2002. **266**: p. 73-90.

30. Corker, D.L., A.M. Glazer, R.W. Whatmore, A. Stallard, and F. Fauth, *A Neutron Diffraction Investigation Into the Rhombohedral Phases of the Perovskite Series*

*PbZr1-xTixO3.* Journal of Physics-Condensed Matter, 1998. **10**(28): p. 6251-6269.

31. Zhao, J., A.E. Glazounov, Q.M. Zhang, and B. Toby, *Nuetron Diffraction Study of Electrostrictive Coefficients of Prototype Cubic Phase of Relaxor Ferroelectric* $PbMg_{1/3}Nb_{2/3}O_3$. Applied Physics Letters, 1998. **72**(9): p. 1048-1050.

32. Misture, S.T., S.M. Pilgrim, J.C. Hicks, C.T. Blue, E.A. Payzant, and C.R. Hubbard, *Measurement of the Electrostrictive Coefficients of Modified Lead Magnesium Niobate Using Neutron Powder Diffraction.* Applied Physics Letters, 1998. **72**(9): p. 1042-1044.

33. Horiuchi, H., T. Kobayashi, and A.J. Schultz, *Time-of-Flight Pulsed Neutron-Diffraction Study on Uniaxial Stress-Induced Domain Switching in LaNbO4.* Japanese Journal of Applied Physics Part 1-Regular Papers Short Notes & Review Papers, 1991. **30**(9A): p. 2035-2039.

34. Cain, M.G., S.M. Bennington, M.H. Lewis, and S. Hull, *Study of the Ferroelastic Transformation in Zirconia by Neutron Diffraction.* Philisophical Magazine B, 1994. **69**(3): p. 499-507.

35. Rogan, R.C., E. Ustundag, B. Clausen, and M.R. Daymond, *Texture and Strain Analysis of the Ferroelastic Behavior of Pb(Zr,Ti)O-3 by In Situ Neutron Diffraction.* Journal of Applied Physics, 2003. **93**(7): p. 4104-4111.

# Chapter 2

## Macroscopic Neutron Diffraction Experiments

### 2.0 Neutron Diffraction Study of PZT Materials

Neutron diffraction is an ideal probe of bulk crystallographic structure due to neutrons' large penetration depth, which allows for true bulk characterization of material properties. This is especially useful for compositions which contain heavy elements such as PZT, where neutrons can fully penetrate several millimeters of material. In comparison, traditional laboratory X-ray sources using copper *K*α radiation can only penetrate ~ 5 μm in PZT, and thus diffracted information is relegated to a few surface grains where mechanical and electrical boundary conditions may differ greatly from the bulk average. The following experiments represent the first *in situ* bulk crystallographic study of the ferroelastic behavior of both single- and multiphase polycrystalline PZT compositions under compressive loading. Simultaneous extraction of the crystal lattice strains and quantitative texture effects (domain switching) was possible through a careful whole-pattern Rietveld analysis.

### 2.1 Strain and Texture Measurements

For the current work, time-of-flight (TOF) neutron diffraction was employed to measure lattice strain and texture in ferroelectric materials under *in situ* compressive loads. TOF neutron diffraction relies on the production of neutrons from a heavy element target

bombarded by pulsed high energy protons [2]. The collision of protons with nuclei in the target induces the emission of neutrons with a large spectrum of wavelengths, which then pass through a moderator that filters out neutrons outside of the thermal spectra. These thermal wavelengths are not known *a priori* to the diffraction events they produce. Instead, the neutrons' *time-of-flight* is accurately measured in order to reverse calculate their wavelengths [2]. This is accomplished through a series of rotating gates called "choppers" which are synchronized with the incoming proton pulses. The choppers' frequencies are tuned so that only a "packet" of neutrons consisting of a known range of velocities is allowed to pass. A single neutron in this packet travels a known distance (the path length) from the moderator, through the diffraction angle determined by the sample crystal lattice, and finally to impact with the detector. The time of a neutron's impact with a detector element is also carefully measured with reference to the initial proton pulse, yielding the time-of-flight from the moderator to the detector. Using these data, a time-dependent definition of the neutron's wavelength can be formed. In order to relate the known diffraction angle (defined by the sample-detector geometry) to a particular *d*-spacing of the crystal sample, Bragg's law must be modified to account for this time-dependent definition of wavelength. If $L$ is the neutron path length and $v$ its velocity, then the time-of-flight $t$ is

$$t = \frac{L}{v} = \frac{\lambda m}{h} L \tag{2.1}$$

where $h$ is Plank's constant and $m$ the neutron mass.

Bragg's law for the diffraction angle $\theta$ can now be rewritten in terms of time-of-flight parameters:

$$\lambda = 2d \sin\theta \tag{2.2}$$

$$\text{or} \qquad t = \frac{2Lmd \sin\theta}{h} \tag{2.3}$$

This allows for the direct relation between neutron time-of-flight and *d*-spacing of a specimen. The lattice strain of a sample under stress may then be calculated in the standard fashion as the normalized change in the *d*-spacing between any (*hkl*) lattice planes with reference to a zero-strain state. Due to the fact that an incident neutron packet possesses a distribution of velocities, a large range of the crystal structure's *d*-spacing information is probed simultaneously. Though the diffracted intensity from a single packet is minimal, the superposition of many neutron packet diffraction events produces a pattern which is analogous to the standard laboratory X-ray $\theta$ - $2\theta$ scan.

Recently, several TOF neutron diffraction spectrometers have been designed for the specific function of *in situ* engineering studies of materials. The work described in this chapter employed three such devices. The SMARTS spectrometer [3] is part of the Los Alamos Neutron Science Center (Los Alamos National Laboratory, Los Alamos, USA), while both the ENGIN spectrometer and its successor, ENGIN-X, reside at ISIS Facility (Rutherford Appleton Laboratory, Didcot, UK). Each of these devices is configured to incorporate a load frame, which may be used to apply compressive (or tensile) stresses to test specimens. Of critical importance to engineering studies are these spectrometers' detector geometry with respect to the loading apparatus (Fig. 2-1).

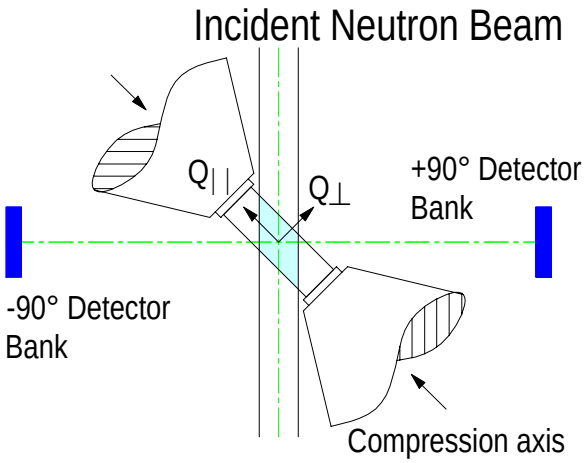


**Figure 2-1**: TOF neutron diffraction geometry for engineering spectrometers. The detector positions define two diffraction vectors, one which measures the longitudinal strain, the other the transverse strain. The detectors are not "point" detectors; each covers an in-plane solid angle of 32°.

The loading fixture orients a test specimen at 45° to the incoming neutron beam, and two detector banks are positioned at ± 90° to the beam. This configuration defines two diffraction vectors, $Q_{||}$ and $Q_{\perp}$, which correspond to diffraction occurring from longitudinal and transverse lattice planes, respectively. Thus the two detectors can separately measure longitudinal and transverse crystal strain, providing a two-dimensional measurement of the micromechanical response of crystalline materials under applied loads. In the specific case of ferroelectric materials which possess domains of different orientations, these longitudinal and transverse detector banks have the ability to measure strain information from domains in two orthogonal orientations at the same time. This is a tremendous advantage over standard laboratory X-ray diffraction techniques, which can only measure the response from a single domain orientation. As will be outlined in the following sections, the anisotropy of ferroelectric materials requires a minimum of two orthogonal detectors to obtain a cohesive understanding of domain switching and lattice strain evolution in these materials.

The final general issue of using TOF neutron diffraction to study ferroelectrics has to do with the effect of domain alignment on diffraction spectra. Grain (or domain) alignment within a polycrystalline sample on a significant level implies a macroscopic material texture. Within a textured polycrystal, a disproportionate amount of grains oriented along the same direction will produce discrepancies in the observed intensity of an (*hkl*) reflection with respect to a true powder average (in which grains orientations are completely random). Depending on the type of texture present in a material and sample orientation within the diffractometer, intensities of certain (*hkl*) reflections may appear stronger or weaker than expected. In the case of ferroelectrics, alignment of domains as a result of electrical poling usuually induces a macroscopic material texture which is cylindrically symmetric with respect to the poling axis. In the presented TOF neutron experiments, the poling direction of ceramic samples was always aligned with the compression axis (longitudinal direction). Due to the sample-detector geometry and the poling symmetry of the ceramic samples, domain alignment will be manifested as fiber texture as viewed from the longitudinal detector bank.

In order to correctly interpret diffraction patterns exhibiting the effects of fiber texture, the March-Dollase function can be applied to adjust the intensities of certain relevant diffraction peaks. The March–Dollase function was designed to correct peak intensities for the effects of fiber texture in cylindrically symmetric samples [4-6]:

$$I_{hkl} = P_{hkl}(\alpha) F^2{}_{hkl} \tag{2.4}$$

where $$P_{hkl}(\alpha) = \left[ r^2 \cos^2(\alpha) + r^{-1} \sin^2(\alpha) \right]^{-3/2} \tag{2.5}$$

Here $I_{hkl}$ is the intensity of a given diffraction peak, $F_{hkl}$ is the structure factor, and $P_{hkl}$ is the March function. This function is a true distribution function and describes the density of poles at a given angle $0 \leq \alpha \leq \pi/2$ (Figure 2-2). Once the relevant (*hkl*) reflection is chosen, only the March coefficient *r* need be defined to yield a complete description of the texture in the sample (provided that the texture does in fact conform to cylindrical symmetry). In other words, the entire orientation distribution function can be collapsed in this special case of fiber texture in a cylindrical sample. The March-Dollase model is also very flexible in that it can be used to define distributions which have a maximum at $\alpha = 0$ ($r < 1$) or a maximum at $\alpha = 90$ ($r > 1$) (see Fig. 2-2).

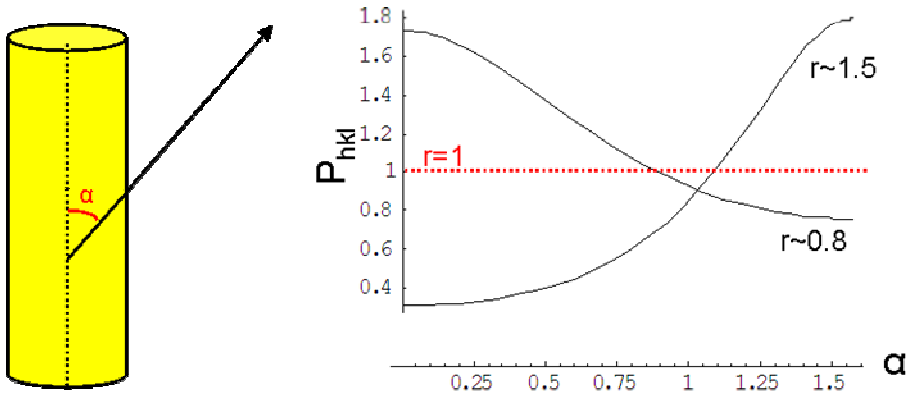


**Figure 2-2:** a) Angle α of the March-Dollase function is measured from the sample cylindrical axis, b) March-Dollase distribution functions defined by various March coefficients *r*.

A March coefficient of unity corresponds to a flat (random) distribution of orientations, implying that a particular crystal pole (*hkl*) does not prefer one direction in the sample versus another. Values less than unity imply a preferred orientation weighted toward the cylindrical axis, and values greater than unity indicated a distribution of poles weighted normal to the cylindrical axis. The relative difference of the March coefficient from

unity indicates the strength of the texture alignment, i.e. an $r = 0.5$ distribution indicates tighter alignment of the specified (*hkl*) pole than an $r = 0.9$ distribution. Specifics of applying the March-Dollase texture model to the diffraction data are given in the following sections, though it should be noted that results for all March coefficients are given for the longitudinal detector only, where strict cylindrical symmetry holds.

## 2.2 Rietveld Refinement Methodology

All TOF neutron diffraction data were analyzed using the GSAS [7] software program to perform whole pattern Rietveld refinements [8]. In general, all Rietveld refinements employed in the analysis for this study proceeded through a careful iteration process. In the case of powder samples, first, single parameters were allowed to vary in an isolated, independent fashion. For example, lattice parameters would be refined and then fixed before allowing the background function to vary. The order of these independent variable refinements was generally as follows: lattice parameters, histogram scaling factor, background function, peak width, and absorption parameter. After 3 successive cycles of convergent independent refinements, variables were refined in mixed pairs. Finally, all of these factors were refined simultaneously to produce a convergent fit. Subsequent to general variable refinement, atomic positions and isotropic thermal parameters ($u_{Pb}$, $u_{Zr}$, etc.) were refined in a similar independent fashion. The culmination of this process resulted in a stable, convergent refinement employing the simultaneous refinement of all the above variables. For the case of atomic site occupancy refinement, no significant deviations (< 2% at.) from the idealized chemistry of any sample was observed. Because these small deviations did not yield an appreciable improvement in

residual fitting errors, sample chemistry was fixed at the idealized composition for each specimen (see below for further details).

For polycrystalline specimens, unit cell atomic positions were assumed to be the same as those of the powder specimens. Additionally, atomic occupancies and thermal parameters were not refined. After refining a linear absorption parameter for a single polycrystalline specimen of a certain composition, this value was also fixed since only changes in sample dimension or composition would affect this parameter. Lattice parameters, histogram scaling factors, background function, and peak profile coefficients were refined in an isolated, independent fashion before a simultaneous refinement of all variables. Case specific Rietveld model adjustments and small deviations from this fitting routine were needed throughout the analysis, and are detailed in the relevant sections below.

Final crystal model quality was evaluated by the minimum achievable pattern residual, $R_p$, and the weighted pattern residual, $R_{wp}$, defined as

$$R_p = \frac{\sum |y_i(obs) - y_i(calc)|}{\sum y_i(obs)} \tag{2.6}$$

and

$$R_{wp} = \left\{ \frac{\sum w_i \left( y_i(obs) - y_i(calc) \right)^2}{\sum w_i \left( y_i(obs) \right)^2} \right\}^{1/2} \tag{2.7}$$

where $y_i(obs)$ and $y_i(calc)$ are the observed and calculated intensities for the $i$ step in the diffraction pattern, and $w_i = 1/y_i$ [9]. The total minimization function employed by GSAS, $X^2$, will approach a value of unity for accurate diffraction pattern simulations [7].

### 2.3 Powder Refinement of Single- and Multiphase PZT Compositions

Several ferroelectric $Pb(Zr_xTi_{1-x})O_3$ material compositions were examined in the course of this study. The first specimens consisted of $Pb(Zr_{0.4}Ti_{0.6})O_3$ (40/60 PZT). This Zr/Ti ratio places the crystal structure squarely in the tetragonal region of the phase diagram [10]. Ceramic powders were prepared using the standard oxide mixing method by Ecertec, Ltd. (Barnsley, South Yorkshire, UK). 40/60 PZT powder was placed in a vanadium canister and inserted into the ENGIN-X diffractometer. A thirty-minute exposure to the neutron beam produced a diffraction pattern with sufficient signal-to-noise ratio for a complete Rietveld refinement. The second series of samples examined using TOF neutron diffraction were of composition $Pb(Zr_{0.6}Ti_{0.4})O_3$ (60/40 PZT). This Zr/Ti ratio implies a strictly rhombohedral crystal structure at room temperature [10]. Ceramic powders were prepared in the same manner as the 40/60 composition, and powder diffraction measurements were performed using the ENGIN-X diffractometer. Here again, a thirty-minute exposure to the neutron beam produced a diffraction pattern with sufficient signal-to-noise ratio for a complete Rietveld refinement.

The final material examined was a commercially available morphotropic composition. Several PZT specimens were obtained from American Piezo Ceramics, Inc. (Mackeyville, PA 17750). Samples were cylindrical and measured approximately 6.35 mm in diameter by 16 mm in length. Chemical composition was determined with an electron probe analyzer (Jeol JXA-733 SEM equipped with wavelength-dispersive spectrometers). Average quantitative atomic fractions were found based on measurements taken at seven random, spatially isolated sample locations. The Zr/Ti atomic ratio was measured to be approximately 49/51 (disregarding small amounts of

dopants such as Sr, Ba and Sb, each < 2.0 at. %). At room temperature, this composition places the sample in the traditional morphotropic region of the phase diagram [10]. A powder sample of the dual-phase PZT composition was obtained by crushing some cylinders using a mortar and pestle. A TOF neutron diffraction pattern of this powder was collected using the SMARTS diffractometer. The powder was placed in a vanadium can and data were collected for approximately 12 h to produce a diffraction pattern with sufficient signal-to-noise ratio for an accurate Rietveld refinement.

### 2.3.1 Tetragonal Single-Phase Powder Refinement

For the initial crystal model of the tetragonal 40/60 PZT, the *P4mm* perovskite structure was applied, with initial crystal variables adopted from results for similar compositions in the literature [11]. Atomic positions were strictly related by the symmetry operators of this space group. If the Pb atom defines the origin of the unit cell at (0,0,0), then the Zr and Ti atoms reside at (½, ½, $z_{Zr}$) and (½, ½, $z_{Ti}$), respectively [11]. Two unique oxygen atom positions fill out the unit cell at (½, ½, $z_{O1}$) and (½, 0, $z_{O2}$) [11]. Thus the symmetry operators of the *P4mm* group constrain the atomic positions such that only the *z* component may vary to alter the unit cell shape.

| Atom | x/a | y/b | z/c |
|---|---|---|---|
| Pb | 0 | 0 | 0 |
| Zr | 0.5 | 0.5 | $z_{Zr}$ |
| Ti | 0.5 | 0.5 | $z_{Ti}$ |
| $O_1$ | 0.5 | 0.5 | $z_{O1}$ |
| $O_2$ | 0.5 | 0 | $z_{O2}$ |

**Table 2-1**: Unit cell atomic position relations for the tetragonal *P4mm* space group [10].

Peak shapes were modeled using a back-to-back exponential pseudo-Voigt convolution function (TOF function #3 in GSAS) whose parameters were calibrated for ENGIN-X diffraction geometry. Because of the standard calibration, only the Gaussian contribution to the peak width need be refined to correct peak shape for sample broadening effects. A six-term power series (TOF function #6 in GSAS) simulated the background, which is a standard function for the ENGIN-X diffractometer. A linear absorption correction was also applied.

The fitting methodology outlined in Section 2.2 was employed, with the exception that the Pb atomic location remain fixed at (0,0,0) to define the origin of the unit cell. Results of the final refinement for the longitudinal detector spectra are listed in Table 2-2, and the final fitted pattern is displayed in Figure 2-3 (results for transverse detector are similar).

| | |
|---|---|
| $a$ | 4.029761 |
| $c$ | 4.164864 |
| $z_{Pb}$ | 0.0000 |
| $z_{Zr}$ | 0.53488 |
| $z_{Ti}$ | 0.51968 |
| $z_{O1}$ | 0.09594 |
| $z_{O2}$ | 0.61336 |
| $u_{Pb}$ | 0.02307 |
| $u_{Zr}$ | -0.00806 |
| $u_{Ti}$ | -0.00884 |
| $u_{O1}$ | 0.01769 |
| $u_{O2}$ | 0.01590 |
| $X^2$ | 1.5 |
| $R_p$ | 6.0% |
| $R_{wp}$ | 8.2% |

Table **2-2**: Final refinement results for the tetragonal phase powder diffraction spectra in the longitudinal detector of ENGIN-X. Residual values indicate a satisfactory match to diffraction data.

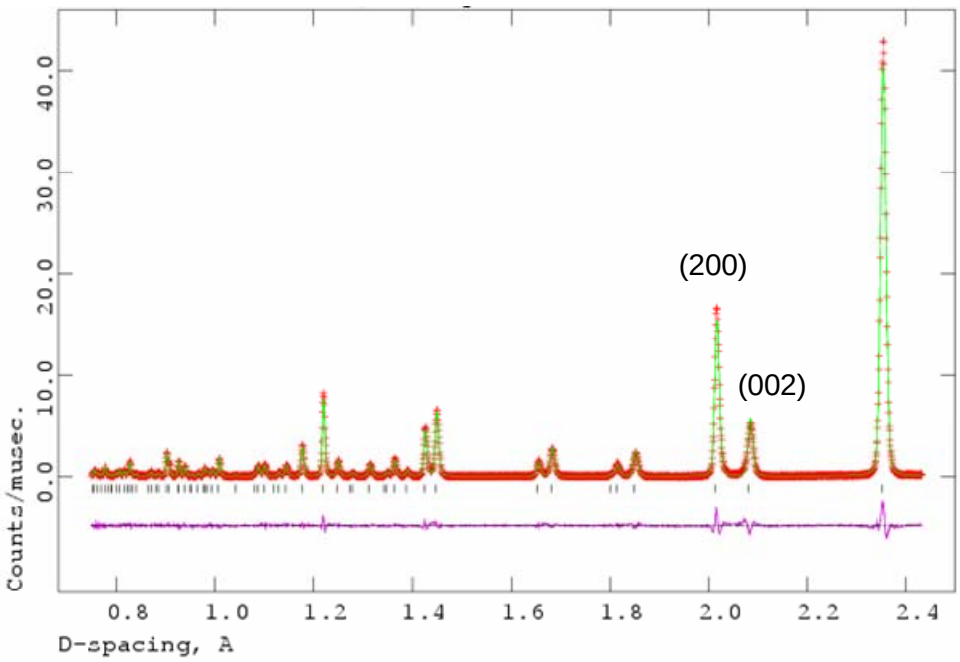


Figure **2-3**: Final simulated diffraction pattern in the longitudinal detector bank of ENGIN-X for the tetragonal phase powder. Crosses are raw TOF neutron data, solid curve is final model simulation, and lower curve is the difference between the two.

While the final crystal model accurately simulates the observed diffraction pattern, thermal parameters for the Zr and Ti atoms are weakly negative. Negative thermal parameters are unphysical, yet this type of thermal parameter discrepancy has been noted in several previous Rietveld refinements of ferroelectric materials. Bedoya *et al.* noted a weakly negative thermal parameter for the O2 atomic site during refinements of Sr doped 53/47 PZT, while Frantti *et al.* observed almost zero thermal parameters for the Pb site in 40/60 PZT [11, 12]. Wilkinson *et al.* reported significantly negative thermal parameters for the Zr and Ti sites during initial refinements of morphotropic PZTs [13]. In general, these various negative thermal parameter results are corrected by introducing constraints on the atomic positions and site fractional occupancies, or by modeling the Pb thermal parameters as anisotropic. By introducing these various constraints, thermal parameters can be forced to conform to estimated "reasonable" non-negative values.

While introducing restraints into the reported model did induce some beneficial effects in the thermal parameter results and limited improvement in fit residuals, "reasonable" positive values of thermal parameters were never observed simultaneously for all atoms. When the reported, more stable model (above) was applied to diffraction patterns obtained from solid ceramic samples, fits converged quickly and with satisfactory results. Attempts to vary the atomic fractions or positions in order to improve thermal parameter results in ceramic specimen diffraction patterns produced a wide variety of results for different samples of the 40/60 PZT composition. Since the ultimate purpose of powder refinements in the context of this study was to form a simple, reliable model for the underlying crystal structure in order to study the lattice strain and

texture response under mechanical load, the unaltered stoichiometric composition of 40/60 PZT exhibiting slightly negative thermal parameters was adopted for the final powder model.

### 2.3.2 Rhombohedral Single-Phase Powder Refinement

While PZT materials may possess two distinct rhombohedral structures at room temperature as a function of Zr/Ti ratio, the 60/40 composition exhibits the *R3m* structure [10]. In accordance with several studies in the literature [1, 11, 12, 14], the *R3m* symmetry for these experiments was constructed through the surrogate space group *R3c* by employing constraints on certain atomic positions. Thus while the *R3c* space group allows for the oxygen octahedral tilting observed in rhombohedral PZT compositions of low Ti content at low temperatures [1], confining the atomic positions of the oxygen atoms to certain planes insures that no tilting occurs and a rigid *R3m* structure is imposed. Specifically, defining the atomic positions of the *R3c* space group as shown in Table 2-3 results in the actual crystal symmetry of *R3m*.

| Atom | *x/a* | *y/b* | *z/c* |
|---|---|---|---|
| Pb | 0.00 | 0.00 | $z_{Pb}$ |
| Zr | 0.00 | 0.00 | $z_{Zr}$ |
| Ti | 0.00 | 0.00 | $z_{Ti}$ |
| O | $x_O$ | $2x_O$ | 1/12 |

**Table 2-3**: Unit cell atomic position relations for the *R3c* space group used in Rietveld refinements. Restricting the oxygen atomic positions as shown enforces an actual symmetry of *R3m*. (*After Corker, et al.* [1])

The benefit of using a simplified *R3c* structure is a more intuitive method of understanding the various angles between polarization directions in the rhombohedral phase in terms of pseudo-cubic unit cell directions. The pseudo-cubic unit cell is defined as the room-temperature distortion in the high-temperature cubic phase unit cell induced by the cubic-to-rhombohedral phase transition. Using pseudo-cubic directions allows for easy comparison to the orthogonal unit cell of the tetragonal phase. The relationship between the rhombohedral *R3c* unit cell lattice vectors (denoted ($h_r$ $k_r$ $l_r$)) and the pseudo-cubic unit cell (denoted ($h_p$ $k_p$ $l_p$)) is the transformation matrix [1]:

$$\begin{pmatrix} 2h_p \\ 2k_p \\ 2l_p \end{pmatrix} \begin{pmatrix} 0.5 & 0 & -0.5 \\ -0.5 & 0.5 & 0 \\ 1 & 1 & 0 \end{pmatrix} = \begin{pmatrix} h_r \\ k_r \\ l_r \end{pmatrix} \tag{2.8}$$

Using this transformation matrix, a simple relationship may be formed between the pseudo-cubic coordinates and the actual rhombohedral coordinates of the crystal structure. In the rhombohedral phase, dipoles form due to ion displacement along the [111] direction in the pseudo-cubic unit cell which corresponds to the [006] direction in the *R*3*c* structure. Domains form at either 71° or 109° angles, reflecting a dipole realignment in one of the [11-1] pseudo-cubic unit cell directions or the [202] directions of the *R*3*c* space group [11, 15-17].

For the initial crystal model of the 60/40 rhombohedral PZT powder, the *R3c* structure was applied, using literature results as initial values for the refinement process [1]. Peak shapes were modeled using a back-to-back exponential pseudo-Voigt convolution function (TOF function #3 in GSAS) whose parameters were calibrated for

ENGIN-X diffraction geometry. Because of the standard calibration, only the Gaussian contribution to the peak width needs to be refined to correct peak shape for sample-dependent effects. A six term power series (TOF function #6 in GSAS) simulated the background, which is a standard function for the ENGIN-X diffractometer. A linear absorption correction was also applied.

Initial inspection of Rietveld refinements for the entire observed *d*-spacing range indicated significant fitting errors in the high *d*-spacing range. These errors were relegated to the (20-4) peak and (006)-(202) doublet regions, where the appearance of broad, diffuse scattering prevented the accurate modeling of peak shape (width) and intensity. The final solution used to interpret rhombohedral phase data was to simply trim these peaks from the analyzed data range. The author acknowledges that removing these peaks may obscure some important crystal information of the fine details of unit cell structure and complex thermal vibration behavior in this phase, however, the end result of reducing the diffraction range had a three fold beneficial impact for the scope of this study: Significant improvement of residual fitting parameters (~10% difference in total *R* values, i.e., from $R_p$ = 22% to 12% ), stabilization of all refinements, and most importantly, recovery of appropriate texture modeling for application to ceramic stress measurements. The harmonic peaks (0,0,12) and (404) remain in the analyzed data, providing equivalent information for the (006)-(202) doublet for textural analysis.

The fitting methodology outlined in Section 2.2 was employed for the reduced data range. The results of the final refinement for the longitudinal detector are listed in Table 2-4, and the final fitted pattern is displayed in Figure 2-4 (transverse detector results are similar).

| | |
|---|---|
| $a$ | 5.801085 |
| $c$ | 14.322429 |
| $z_{Pb}$ | 0.28014 |
| $z_{Zr}$ | 0.01822 |
| $z_{Ti}$ | 0.03199 |
| $x_O$ | 0.17172 |
| $u_{Pb}$ | 0.03136 |
| $u_{Zr}$ | 0.00970 |
| $u_{Ti}$ | -0.01441 |
| $u_O$ | 0.02793 |
| $X^2$ | 2.4 |
| $R_p$ | 5.1% |
| $R_{wp}$ | 6.3% |

**Table 2-4**: Final refinement results for the rhombohedral phase powder diffraction spectra in the longitudinal detector of ENGIN-X. Residual values indicate a satisfactory simulation of the diffraction pattern.

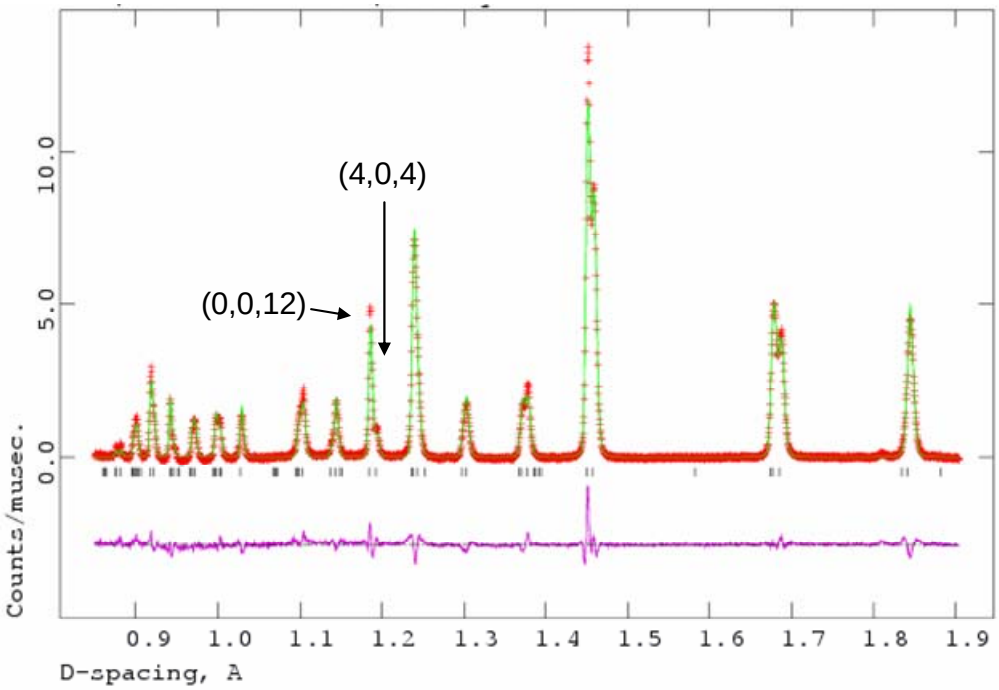


**Figure 2-4**: Final simulated diffraction pattern in the longitudinal detector bank of ENGIN-X for the rhombohderal phase powder. Crosses are raw TOF neutron data, solid curve is final model simulation, and lower curve is the difference between the two.

### 2.3.3 Morphotropic Dual-Phase Composition Powder Refinement

Cursory preliminary analysis of the morphotropic composition data collected on the SMARTS diffractometer indicated that this material was most likely a two-phase system, as evidenced by the presence of intensity between tetragonal phase peak doublets [11-13, 18]. Thus in addition to the standard single-phase refinement variables, the phase fraction (tetragonal vs. rhombohedral) of the morphotropic composition was also refined to scale the relative intensity contributions from each phase. Crystallographic data obtained from previous studies on PZTs were employed as a starting point in the analyses [11, 12]. As in the single-phase composition refinements, space groups *P*4*mm* and *R*3*c* were used for the tetragonal and rhombohedral phases, respectively. The average atomic occupancies were determined from the electron microprobe analysis and were initially assumed to be the same for both phases. The Zr/Ti ratio found by the microprobe analysis was 49/51 (disregarding small amounts of Sr, Ba, and Sb dopant atoms, which were present in amounts less than 1.5% at. each). Atomic positions and isotropic thermal parameters were constrained to be the same for chemically identical sites; i.e., dopant atoms were required to mimic the atoms they replaced. Restricting chemically identical sites to have the same properties was necessary due to the extremely small amounts of dopants present (refinement of these atomic parameters independently resulted in catastrophically unstable refinements). Restrictions were not applied to the Zr and Ti positions and thermal parameters, which were allowed to refine independently. The background function was modeled using a ten-term power series (TOF function No. 6 in GSAS) which is the regular function for the SMARTS diffractometer. A Von Dreele–Jorgensen–Windsor convolution function (TOF function No. 1 in GSAS) was used for

the peak profiles of each phase. The Gaussian peak widths for both phases were refined independently.

All atomic positions were refined except for the Pb position in the tetragonal phase (to preserve the origin of the space group), and the oxygen positions for the rhombohedral phase were constrained to preserve the actual *R3m* symmetry (no octahedral tilting in the *R3c* surrogate space group). Some of the previously mentioned problems generally associated with Rietveld refinements of PZTs were also noted in this analysis [1, 11-13]. The introduction of anisotropic thermal parameters induced significant instabilities due to the complexity of the background, and they were subsequently removed from the model. The literature, too, exhibits significant scatter in the various crystallographic parameters describing morphotropic materials [1, 11-13]. Again, since the purpose of the present study was not to perform a detailed crystallographic analysis of PZT as a function of composition, but to systematically investigate the effects of mechanical loading on the material, the current analysis was considered satisfactory.

The fitting methodology outlined in Section 2.2 was employed individually for the tetragonal and rhombohedral component phases, with the addition of phase fraction refinement. The results of the final refinement for the longitudinal detector diffraction spectra of the morphotropic composition powder are listed in Table 2-5, and the final fitted pattern is displayed in Figure 2-5 (transverse detector results are similar). Note that the exceptionally large value of $X^2$ for the final refinement is a result of the complicated low *d*-spacing background of the SMARTS diffractometer (Figure 2-5). $R_p$ and $R_{wp}$ residuals of ~ 2% indicate an accurate model simulation of the diffraction pattern.

| Tetragonal | | Rhombohedral | |
|---|---|---|---|
| $a$ | 4.048377 | $a$ | 5.744623 |
| $c$ | 4.115473 | $c$ | 14.19382 |
| $z_{Pb}$ | 0.0000 | $z_{Pb}$ | 0.26948 |
| $z_{Zr}$ | 0.55255 | $z_{Zr}$ | 0.01321 |
| $z_{Ti}$ | 0.56427 | $z_{Ti}$ | 0.02770 |
| $z_{O1}$ | 0.08346 | $x_O$ | 0.15700 |
| $z_{O2}$ | 0.60118 | $U_{Pb}$ | 0.01476 |
| $U_{Pb}$ | 0.04505 | $U_{Zr}$ | 0.03566 |
| $U_{Zr}$ | 0.09779 | $U_{Ti}$ | -0.00508 |
| $U_{Ti}$ | 0.02625 | $U_O$ | 0.01792 |
| $U_{O1}$ | 0.02625 | | |
| $U_{O2}$ | 0.02475 | | |
| | $X^2$ | 21.0 | |
| | $R_p$ | 1.7% | |
| | $R_{wp}$ | 2.2% | |

**Table 2-4**: Final refinement results for the both phases of the morphotropic composition powder diffraction spectra in the longitudinal detector of the SMARTS diffractometer. The complicated low *d*-spacing background function of the SMARTS diffractometer produced large $X^2$ for this fit.

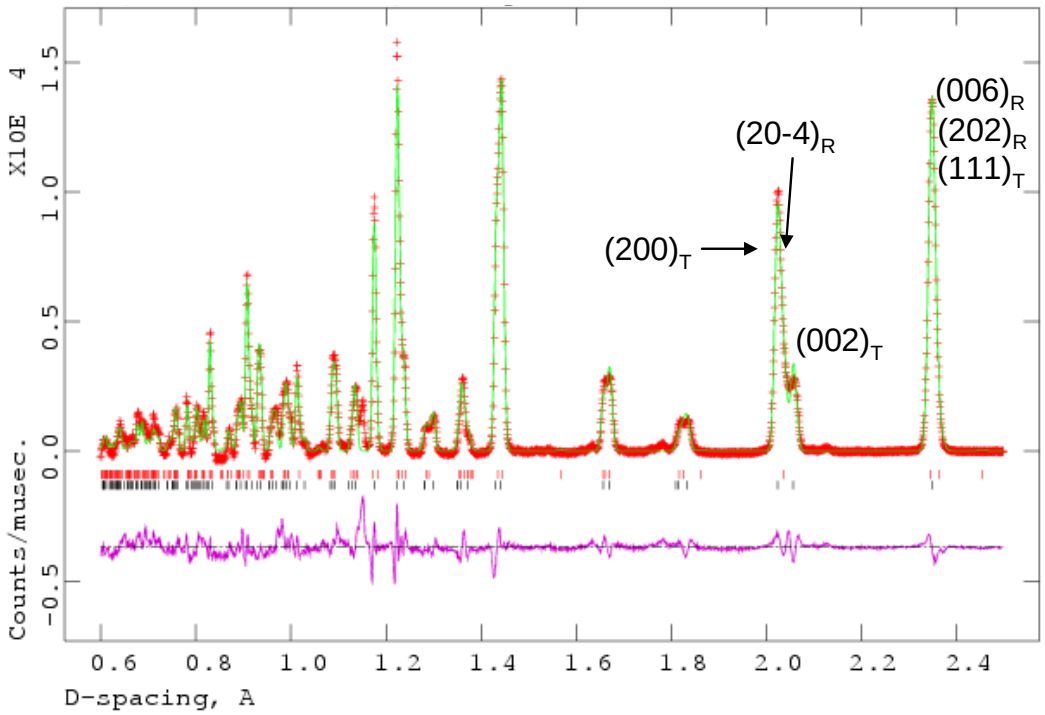


**Figure 2-5**: Final simulated diffraction pattern in the longitudinal detector for the morphotropic composition powder. Crosses are raw TOF neutron data, solid curve is model simulation, and lower curve is the difference between the two. The complicated low *d*-spacing background function of the SMARTS diffractometer produced large $X^2$ for this fit.

The relative peak widths of the two phases were found to differ by only 7% and were thus considered to be the same in further analysis [11]. The Rietveld refinement yielded final volumetric phase fractions of roughly 79% tetragonal and 21% rhombohedral. These numbers confirm that the material is indeed in the morphotropic region of the phase diagram in agreement with the Zr/Ti ratio measured by the electron microprobe analysis. Comprising approximately one-fifth of the sample volume the rhombohedral phase is expected to affect the macroscopic properties of this material. It is important to note, however, that due to the large size of the rhombohedral phase's unit cell, its fractional contribution to the diffracted intensity is much less than its volumetric phase fraction.

## 2.4 Loading Experiments of Single- and Multiphase PZT Ceramics

Pressed, sintered ceramic samples of 40/60 tetragonal and 60/40 rhombohedral single-phase compositions were obtained from Ecertec Ltd. (Barnsley, South Yorkshire, UK), and measured 5 x 5 x 10 $mm^3$. Both sample types were poled under high electric fields prior to diffractometer insertion. Poling conditions were optimized by Ecertec personnel for each phase to yield high values of piezoelectric charge constant ($d_{33}$) and and electromechanical coupling factor ($k_{33}$) without inducing specimen fracture. The tetragonal single-phase (tetragonal-SP) specimens were exposed to a field strength of 3 kV/mm at 80°C for 60 minutes. According to measurements taken by Ecertec, the poling process resulted in an average $d_{33}$ of 5.9 pm/V and a $k_{33}$ of 0.035%. These values, in general, indicate a weak piezoresponse for the tetragonal ceramic specimens.

The rhombohedral single-phase (rhombohedral-SP) samples, on the other hand, exhibited an average $d_{33}$ of 104.5 pm/V and a $k_{33}$ of 0.35% after poling in a field of only 2.5 kV/mm at 125° C for 15 minutes. Because the strength of a ceramic's piezoresponse depends ultimately on the successful alignment of domains within a polycrystal, these results hint that electrical poling aligns significantly more domains in the rhombohedral-SP ceramic relative to the tetragonal-SP specimen.

The dual-phase morphotropic ceramic specimen was supplied by American Piezoceramics, Inc. (Mackeyville, PA 17750). Samples were cylindrical and measured approximately 6.35 mm in diameter by 16 mm in length. The morphotropic phase cylinders were of the same composition as the morphotropic powders. The ceramic cylinder was poled using a proprietary process, which cannot be reported here due to

company policy. American Piezoceramics literature reports a final $d_{33}$ of 400 pm/V and a $k_{33}$ of 0.72%. Thus the morphotropic composition has far superior piezoelectric properties than either of the single-phase compositions, as summarized in Table 2-6.

| Composition | $d_{33}$ (pm/V) | $k_{33}$ (%) |
|---|---|---|
| Single-phase Tetragonal $Pb(Zr_{0.40}Ti_{0.60})O_3$ | 5.9 | 0.035 |
| Single-phase Rhombohedral $Pb(Zr_{0.60}Ti_{0.40})O_3$ | 104.5 | 0.35 |
| Morphotropic $Pb(Zr_{0.49}Ti_{0.51})O_3$ (Tetragonal & Rhombohedral) | 400 | 0.72 |

**Table 2-6**: Piezoelectric charge coefficient and electromechanical coupling factor data supplied by manufactures of the three ceramic specimens tested in compression

Strain gauges were attached to the faces of all specimens to record macroscopic longitudinal (direction parallel to loading) sample strain under applied stress. Loading experiments on the morphotropic composition were carried out on the ENGIN diffractometer, while the tetragonal-SP and rhombohedral-SP samples were studied using the ENGIN-X diffractometer. Samples were subjected to a series of sequential compressive loads. After each load change, the specimens were allowed to relax at constant load for 15 minutes before diffraction information was recorded. Crystallographic data refined during the powder analyses were implemented to fit spectra obtained from loaded ceramic specimens. None of the atomic positions or thermal parameters were refined for these data sets, as these values are not expected to vary greatly between powder samples (loose grain packing) and ceramic samples (tight grain packing). Zero-load patterns of each ceramic PZT composition were used to refine linear absorption coefficients, which were then fixed for diffraction patterns of subsequent

loads. For each point on the loading curves, histogram scaling factor, lattice parameters, background function, Gaussian peak width, and crystal texture variables were refined simultaneously. Case specific details of the refinement process are given in the following sections.

### 2.4.1 Tetragonal Single-Phase Ceramic Loading Experiment

The macroscopic loading curve obtained from strain gauge measurements of a single-phase tetragonal sample under compression is displayed in Figure 2-6. Note that the "zero" strain level corresponds to the poled state, thus ignoring any residual strains present from the pressing, sintering, or poling processes. The material response is predominantly elastic, exhibiting linear stress-strain dependence and virtually no detectable residual strain upon unloading.

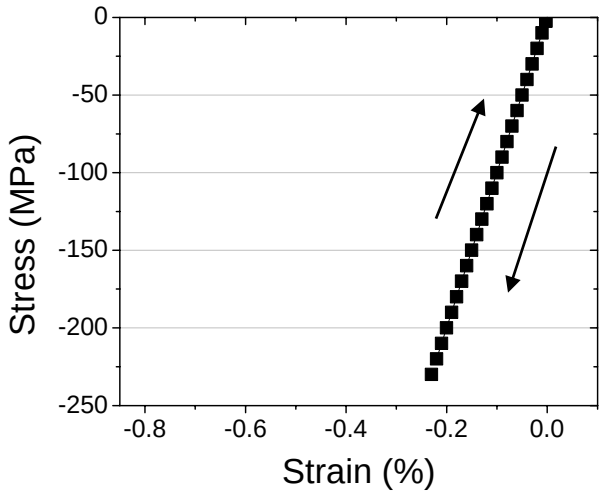


**Figure 2-6**: Macroscopic strain curves for the single-phase tetragonal ceramic sample as measured by a longitudinal strain gauge.

The poled tetragonal ceramic specimen displayed minor evidence of texture effects in the zero load diffraction spectra, as evidenced by the crystal model's slight misappropriation of intensities in the (200)-(002) diffraction peaks. It is well known that tetragonal PZT exhibits polarizations aligned along the [001] direction of the unit cell, and that the diffracted intensities from related reflections can be used to measure extent of domain alignment in these materials [11, 15, 19, 20]. Applying the March–Dollase model to the tetragonal phase was straightforward: the [001] direction corresponds to the crystallographic dipole, and the angle between domains discernable in a diffraction experiment is 90°, so texture in this phase could be modeled easily by tracking the intensity variations between the prominent (200)–(002) doublet (Fig. 2-3) [11, 15, 20, 21]. Using a preferred orientation axis of [001] in GSAS and refining the March coefficient for this family of peaks significantly reduced the $R_p$ and $R_{wp}$ values for all fits (~1.5% reduction in absolute $R$ values). The average fitting results for all loading spectra in the longitudinal detector are displayed in Table 2-7 (transverse bank results are similar).

| | |
|---|---|
| $X^2$ | 1.0 |
| $R_p$ | 9.0% |
| $R_{wp}$ | 12.0% |

**Table 2-7**: Average Rietveld refinement fitting results from the longitudinal detector for all load patterns of the tetragonal ceramic sample.

Results for the March coefficient measured from the TOF neutron diffraction patterns are plotted in Figure 2-7 a. In the initial poled state at zero applied stress, note

that the March coefficient is approximately unity, corresponding to a random texture for the (001) oriented crystallites. This result agrees with the relatively weak piezoresponse observed for this composition. Upon loading, some small changes are observed (beyond the error bars), culminating in a final value of 1.135 at a compressive stress of -240 MPa. After unloading, the value remains above unity at 1.055. These results indicate that some amount of 90° domain switching has been successfully activated during loading, and during unloading some portion of this switching is reversed, though not all domains return to their original configuration. This is an effect of the well-known hysteresis exhibited by these ferroelectric materials.

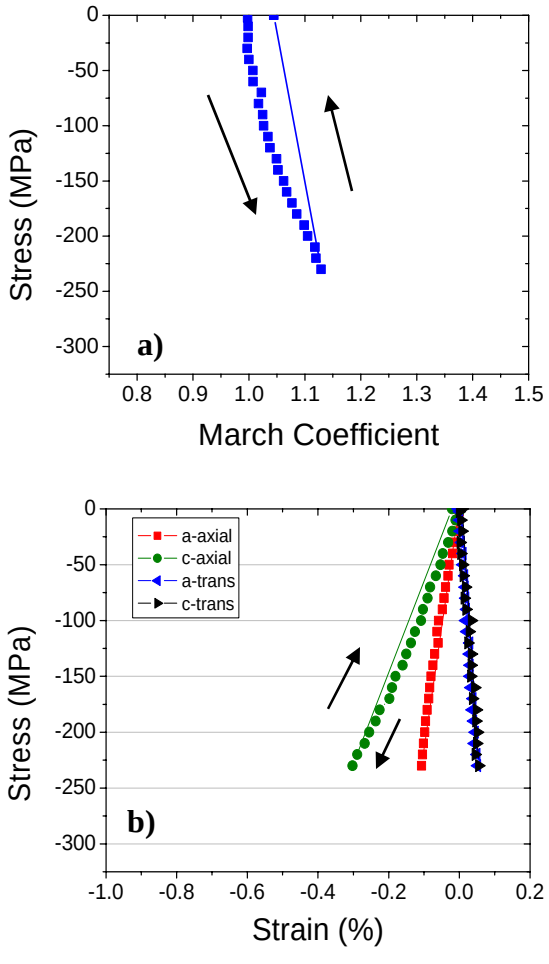


**Figure 2-7**: a) March coefficients measured in the single-phase tetragonal specimen under compression, b) axial and transverse crystal lattice strain results for the same compression test. Error bars for both plots are on the order of the data point symbol size and have been omitted for clarity.

Stress-strain curves for the various recorded lattice parameters are plotted in Figure 2-7 b. All measurements are referenced to the poled sample configuration (the zero-load state). Errors reported by GSAS after convergence (representative only of fitting errors) are on the order of the data point symbol size and have been omitted for clarity. Here the labels ‘‘axial’’ and ‘‘trans.’’ refer to the macroscopic sample directions of the cylindrical axis and the direction perpendicular to it, respectively. One must remember that each detector only measures the spacing between certain crystal planes which fulfill the diffraction condition for that detector. At this point, it will help to consider the evolution of a single, initially poled tetragonal domain throughout the loading procedure. In the zero-load configuration, this hypothetical domain is oriented such that its *c* axis is parallel to the loading axis and the associated planes satisfy Bragg’s law with respect to the longitudinal detector. The planes along the *a* axis in this domain do not. Therefore, only information on the *c* axis is available to the longitudinal detector and no intensity is present from the *a* axis. At some applied load, internal stresses may force this domain to reorient itself, switching by 90°. Now the domain’s *a* axis planes fulfill the diffraction condition and contribute intensity to the pattern in the longitudinal detector; correspondingly the *c* axis information has effectively disappeared from the longitudinal spectra. In terms of the time-of-flight diffraction peaks, this change is manifested during the course of compressive loading by the disappearance of intensity for the (002) peak and appearance of intensity in the (200) peak in the longitudinal detector. An example of this change is shown in Figure 2-8 (not the single-phase tetragonal sample used in this experiment). In the transverse detector, the opposite behavior has been recorded: as the domains switch to reorient their *c* axis in the transverse direction, the

intensity in the (002) peak is introduced and intensity in the (200) peak is lost. In a polycrystalline sample with many domains these effects occur in a continuous manner.

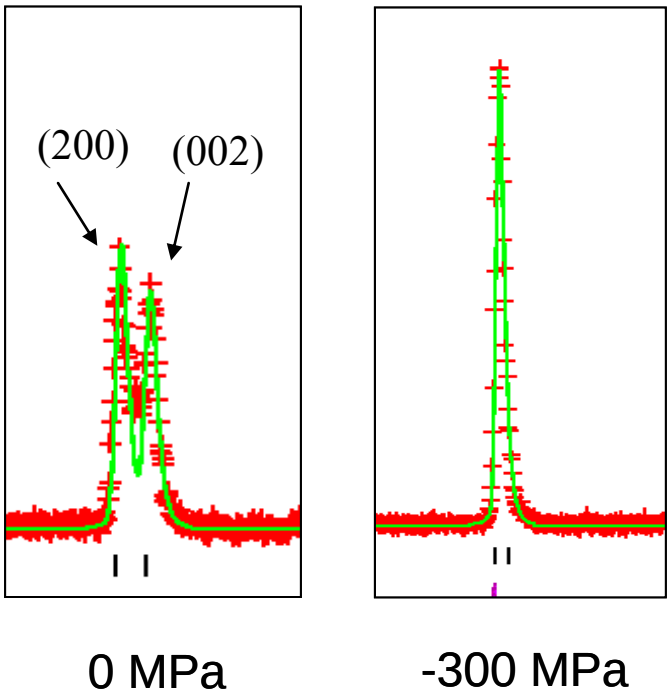


**Figure 2-8**: Example of intensity variations observed in longitudinal detector due to domain switching. (200) peak intensity increases and (002) peak intensity decreases as domains switch from the poled position (*c* axis in diffraction condition) to switched position (*a* axis in diffraction condition).

Returning now to the lattice strain evolution, Fig. 2-7 b shows that domains oriented with their *c* axis parallel to the loading axis (*c*-axial), as measured in the longitudinal detector bank, exhibit the largest compressive strains during loading. The *a*-axial measurement also indicates compressive strains, but of a lower magnitude. Because the March coefficient results indicate that the tetragonal-SP sample does not exhibit significant material texture in the poled state and undergoes only limited domain switching, the strain results may be considered representative of the intrinsic elastic

anisotropy (stiffness) of the polycrystal, rather than the result of complicated domain switching phenomena. The longitudinal strain curves, then, indicate that the *c* direction of the unit cell is more compliant than the *a* direction. While the single crystal elastic constants of PZT are unknown (due to the difficulty of growing single crystals), this is consistent with the single crystal results for the similar ferroelectric $BaTiO_3$, which also possesses the *P4mm* tetragonal structure [22]. The corresponding deformation of these the *c*-axial domains in the transverse direction is captured by the *a*-trans. strains in Figure 2-7 b. Notice that they exhibit the expected Poisson effect and are positive.

### 2.4.2 Rhombohedral Single-Phase Ceramic Loading Experiment

The macroscopic stress-strain curve obtained from strain gauge measurements of the rhombohedral-SP sample under compression is displayed in Figure 2-9. Note that the "zero" strain level corresponds to the poled state, thus ignoring any residual strains present from the pressing, sintering, or poling processes. Significantly higher strains are achieved in the rhombohedral-SP sample as compared to the tetragonal-SP sample (see Fig. 2-6). The rhombohedral-SP stress-strain curve also exhibits the changing slope with increased compressive load which is normally associated with the inelastic effects of domain switching [23, 24]. Because the sample fractured at nearly -350 MPa, it is impossible to speculate if any residual strains would be present in the reported sample. However, similar tests on other rhombohedral-SP specimens (not shown) indicated that larger residual strains occur upon unloading than for the tetragonal-SP ceramics.

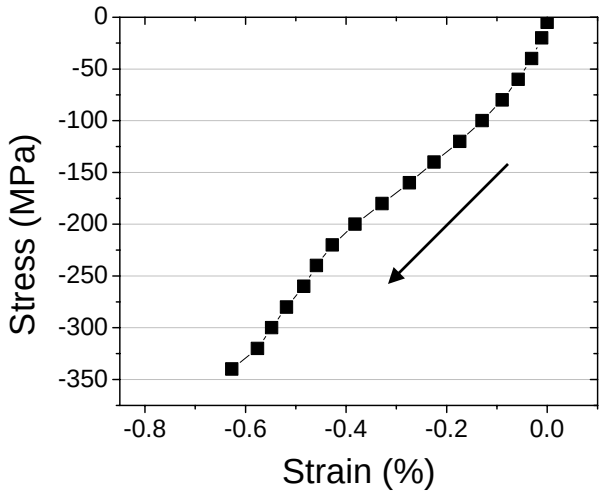


**Figure 2-9**: Macroscopic strain curve for the single-phase rhombohedral ceramic sample as measured by a longitudinal strain gauge.

The rhombohedral-SP specimen diffraction spectra exhibited significant texture effects as a result of the poling process. Applying the March-Dollase texture model to the rhombohedral phase, however, was slightly more complicated than the tetragonal phase case. In the rhombohedral phase, dipoles form due to ion displacement along the [111] direction in the pseudo-cubic unit cell which corresponds to the [006] direction in the *R*3*c* structure (analogous to the [001] direction in the tetragonal phase). Domains form at either 71° or 109° angles, reflecting a dipole realignment in one of the [11-1] directions of the pseudo-cubic cell geometry or the <202> directions of the *R*3*c* space group (analogous to the [100] domain direction of the tetragonal phase) [11, 14]. Similar to the tetragonal phase analysis, only a single texture pole need be defined to apply the March-Dollase model. Using a preferred orientation axis of [006] and refining the March coefficient for this reflection family improved all fits.

| | |
|---|---|
| $X^2$ | 0.9 |
| $R_p$ | 11.8% |
| $R_{wp}$ | 14.9% |

**Table 2-8**: Average Rietveld refinement fitting results from the longitudinal detector for all loading spectra of the rhombohedral ceramic sample.

Results for the March coefficient of the single-phase rhombohedral composition as a function of load are displayed in Figure 2-10 a. The initial value of ~0.6 indicates strong alignment of the (111) dipoles with the longitudinal sample axis (the poling direction). The March coefficient begins to change rapidly near -100 MPa as large scale domain switching is activated, and crosses the random polycrystalline configuration (represented by 1) at -175 MPa of stress. This is in effect the mechanical de-poling of an electrically poled PZT. Beyond -275 MPa of compressive load, the March coefficient begins to stabilize before reaching a final value of ~1.67 prior to sample fracture. Thus as compared to the tetragonal phase March coefficient results, the rhombohedral sample texture exhibits both a higher response to electrical poling and larger susceptibility to mechanical depoling (see Fig. 2-7 a).

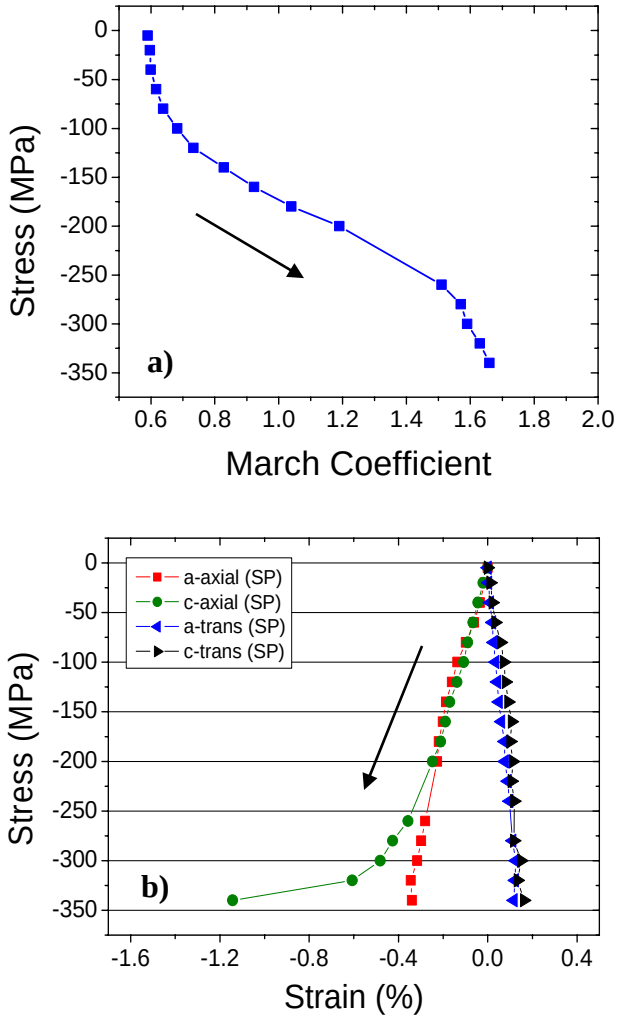


**Figure 2-10**: a) March coefficients measured in the single-phase rhombohedral specimen under compression, b) axial and transverse crystal lattice strain results for the same compression test. Error bars for all curves are on the order of the symbol size, and have been omitted for clarity.

Lattice strain results for the rhombohedral phase are plotted in Figure 2-10 b. Here also, some care must be taken while interpreting the results. The basic rhombohedral lattice parameters *a* and *c* correspond to the (100) and (001) lattice planes of the *R3c* space group. If translated into the pseudo-cubic unit cell geometry, these lattice planes represent the (1-10) and (111) planes, respectively. The *c* lattice parameter of the *R3c* space group, then, is aligned with one possible direction of pseudo-cubic unit

cell dipoles (the [111]), the *a* lattice parameter is not parallel with the possible "switched" domain configurations (the [11-1] directions). In the tetragonal-SP system, on the other hand, both the possible domain orientations will align with their *a* and *c* unit cell axes in positions where they can be recorded by the longitudinal or transverse detector (poled orientation: 0°, switched orientation: 90°). Thus complete analogy between the rhombohedral-SP strain results and the micromechanically simpler tetragonal system cannot be formed. Still, Figure 2-10 b yields much information of the micromechanical state of the rhombohedral phase under load. Here again we see that lattice strains are largely linear, with both the *a*-axial and *c*-axial lattice planes in compression, while the *a*-trans. and *c*-trans. planes exhibit tension.

These results are somewhat unexpected due to the evidence of large scale domain switching in the rhombohedral phase. Domain switching acts as an internal stress relief mechanism, implying that in stress ranges where switching occurs (akin to a plastic regime) the internal resolved stress on a given domain orientation should be different than stress ranges where switching does not occur (a linear elastic regime). Exactly what type of deviation from linear elastic behavior to expect is hard to predict: domain switching may relieve internal stresses on certain domain orientations producing lower relative strain changes between loads, or it may induce load transfer to certain domain orientations and correspondingly large strain changes relative to elastic regions of the stress-strain curve. In either case, a relative compliance difference between the non-switching (elastic) and switching (plastic) regions of the stress-strain curve should be evident. In terms of the strain results in Figure 2-10 b, this means that a relative compliance change should occur in some or all of the lattice parameters between the

stresses of -100 and -240 MPa (where the large changes in the March coefficient indicate domain switching is active (Fig. 2-10 a)). Instead, all of the lattice strains in this stress range are linear, implying that domain switching induces a negligible change on the internal stress state affecting the domains. It is only beyond -240 MPa, after the majority of available domain switching has completed, where a compliance change in the *c*-axial lattice parameter is observed. It is important to remember that this curve represents domains which *do not* switch (pinned) and are still aligned with the initial poling direction so that they continue to contribute to the *c*-axial data in the longitudinal detector. The run-away strain change in the *c*-axial measurement prior to sample fracture (below -340 MPa.) is not well understood at this time, although it is suspected that this may be the source of ultimate fracture of the ceramic.

### 2.4.3 Morphotropic Dual-Phase Composition Ceramic Loading Experiment

Figure 2-11 displays the results for the longitudinal (axial) macroscopic sample strain as measured by the strain gauge during the loading procedure. Strains are referenced from the poled (zero-load) configuration, ignoring any residual strains induced by the pressing, sintering, or poling processes. Here is observed clear evidence of domain switching. It is seen that the initial elastic region is very small, below -25 MPa. Notice the large changes in strain during the stress changes between -25 and -100 MPa, corresponding to domain switching of either one or both phases within the ceramic. Upon reaching -150 MPa, the switching process has saturated and the sample's initial polarization along its cylindrical axis will have largely vanished. At stresses greater than –150 MPa, the material again exhibits nearly linear elastic behavior. During unloading, most of the domains remain in

their switched position (an effect of the electromechanical hysteresis in PZTs). Thus the domain switching produces a large residual strain in the longitudinal direction upon unloading. Texture and lattice strain evolution data obtained from neutron diffraction support these observations.

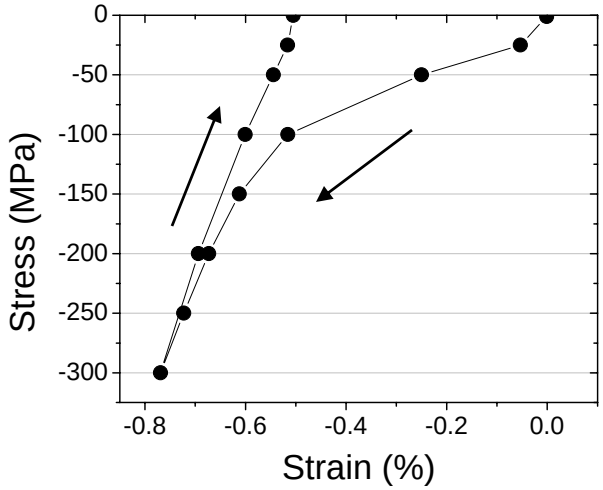


**Figure 2-11**: Macroscopic strain curve for the morphotropic ceramic sample as measured by a longitudinal strain gauge.

GSAS refinements of the ceramic morphotropic sample differed slightly from the single-phase analysis because different diffractometers were employed for the powder and ceramic experiments. Compression testing of the morphotropic ceramic sample was carried out on the ENGIN diffractometer. Atomic positions and thermal parameters for the individual-phases were fixed from the powder results, and the relative volumetric phase fractions remained constant. The peak widths of the two phases were constrained to be the same [11], an assumption which was validated by the analysis of the powder as described above. All other peak profile variables were fixed by standard calibrations of the ENGIN diffraction geometry. The background was modeled using a six-term power series (TOF function #6 in GSAS), which is a standard background function for the

ENGIN diffractometer. Patterns for each load level were refined in a sequential fashion using flags for the lattice parameters, peak widths, histogram scale factor, texture variables (March coefficients), and background function.

Texture analysis for the morphotropic specimen was somewhat complicated by the overlap of diffractions peaks from each phase. For example, the rhombohedral (006)-(202) peak doublet lies in the region of the high-intensity (111) peak of the tetragonal phase, while the (200)-(002) doublet of the tetragonal phase overlaps the (20-4) of the rhombohedral phase (see Fig. 2-5). The convolution of intensities in these regions therefore produces large and misshapen diffraction peaks. Unambiguous assignment of relative intensities in these regions using single-peak fits was not possible due to the destabilizing effects of the instrumental peak width and the relatively low signal-to-noise ratio resulting from short collection times at ENGIN. The constraints imposed on lattice parameters during whole-pattern Rietveld refinements countered these detrimental convolution effects by strictly limiting the uncertainty in the peak positions. Still, the final fit quality for the morphotropic specimens was generally lower than that of the single-phase compositions (Table 2-9):

| | |
|---|---|
| $X^2$ | 1.1 |
| $R_p$ | 16.3% |
| $R_{wp}$ | 18.2% |

**Table 2-9**: Average Rietveld refinement fitting results from the longitudinal detector for all loading spectra from the mophotropic ceramic sample.

While these residuals are generally considered high by Rietveld standards, they are a reflection of the effects of the signal-to-noise ratio, rather than indications of gross miscalculation ( $X^2$ values were approximately 1 for both banks).

The texture observed in the specimen changed significantly over the course of loading and unloading due to domain switching. Figure 2-12 shows the changes in the March coefficient of the tetragonal phase component ($r_T$ ) of the morphotropic composition (tetragonal-M) as a function of applied stress. Here the value of $r_T$ is initially less than 1.0, representative of a large number of crystallographic (001) poles aligned with the sample's cylindrical axis after electrical poling. As the load is increased, $r_T$ quickly passes through the random powder texture value of 1.0 and proceeds to increase dramatically up to a value of about 1.4 between -100 and -150 MPa applied stress. Since $r_T$ values greater than 1.0 correspond to a distribution function with a maximum at $\alpha = \pi/2$, the diffracted intensities detected in the longitudinal bank beyond -150 MPa are indicative of a majority of (001) poles aligned along a direction normal to the sample axis (the transverse direction). This increase is a clear observation of the 90° domain switching in the tetragonal phase, consistent with the switching of domains that initially were oriented with their *c* axis parallel to the loading direction reorienting such that the *c* axis becomes perpendicular to the loading axis. Above -150 MPa, the switching process has saturated, and the $r_T$ value is roughly constant. During the unloading procedure, most of the switched domains remain locked and cannot return to their original configuration, as indicated by the roughly constant value of the March coefficient. Only a slight decrease is noted between -50 MPa and 0 MPa, corresponding to the relaxation of a small fraction of domains.

The rhombohedral phase is a minority phase in the specimens studied. Therefore, the results obtained from this phase should be viewed with caution because of the low counting statistics and the limited data resolution of the ENGIN spectrometer compared to the ENGIN-X spectrometer. However, the rhombohedral March coefficient ($r_R$) is still an accurate measure of the texture of the loaded specimen in the axial direction (Fig. 2-12). Comparing the rhombohedral-M and tetragonal-M results, initial values of $r_R$ (~0.6) and $r_T$ (~0.83) indicate that the rhombohedral phase of this morphotropic PZT was more effectively poled electrically compared to the tetragonal phase (Fig. 2-12). As the load increased, a similar behavior is observed in the rhombohedral-M as was in the tetragonal-M case, only more severe, with a peak $r_R$ value of 1.8 at -300 MPa; indicating that in the mechanical depoling process too, the rhombohedral-M phase domains are more easily reoriented under applied loads.

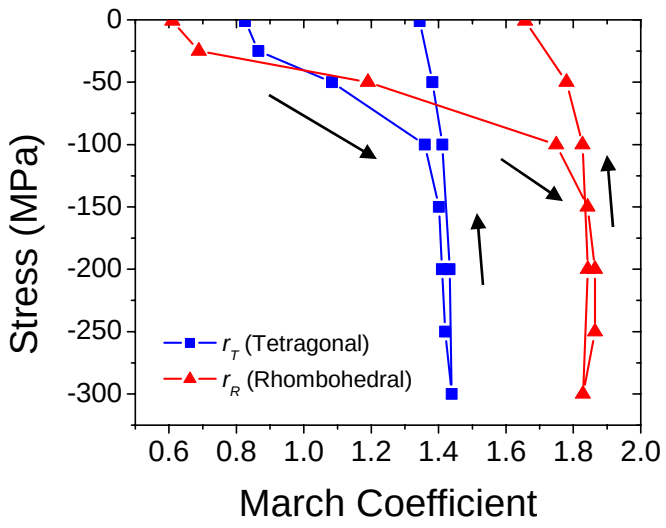


**Figure 2-12**: March coefficient results for the tetragonal and rhombohedral phase portions of morphotropic ceramic sample. Error bars are on the order of symbol size and have been omitted for clarity.

The lattice strain evolution of the tetragonal-M portion of the morphotropic sample is shown in Figure 2-13 a. Domains oriented with their *c* axis parallel to the loading axis (*c*-axial) undergo a large compressive strain change during loading, in addition to an apparent change in the *c* compliance between -25 and -100 MPa. This can be interpreted as lattice shrinkage along the *c* axis due to the domain switching. Since domain switching is mostly inactive during unloading, the axial strain cannot be relaxed. The corresponding deformation of these domains in the transverse direction is captured by the *a*-trans. strain curve in Figure 2-13 a. Notice that they exhibit the expected Poisson effect and are positive. In these lattice planes the *a*-trans. curve appears roughly linear, although there are suggestions of non-linear effects between -25 and -100 MPa which would correspond to the domain switching regime. This is expected since the slope change in the *c*-axial measurement should induce a corresponding change in the *a* lattice parameter strains of the same grain (*a*-trans.) through the Poisson effect.

On the other hand, domains in the switched orientation with their *c* axis perpendicular to the loading direction (and hence contribute to *a*-axial and *c*-trans.) exhibit linear strains in both the axial direction and the transverse direction. This is also expected since the orientation of these domains is already a low-energy configuration, leaving them with no driving force to switch under applied stress. It is interesting to note, however, that there are no clear transient effects of domain switching on the apparent compliances of *a*-axial and *c*-trans. The *c*-axial strain curve is unique then, in that domain switching has a large impact on the internal stress state experienced by the *c* direction of poled tetragonal domains. As tetragonal domains switch to accommodate internal stresses, domains which remain in the poled orientation could be subjected to a

disproportional amount of the macroscopic longitudinal load as evidenced by the apparent softening in the *c*-axial compliance.

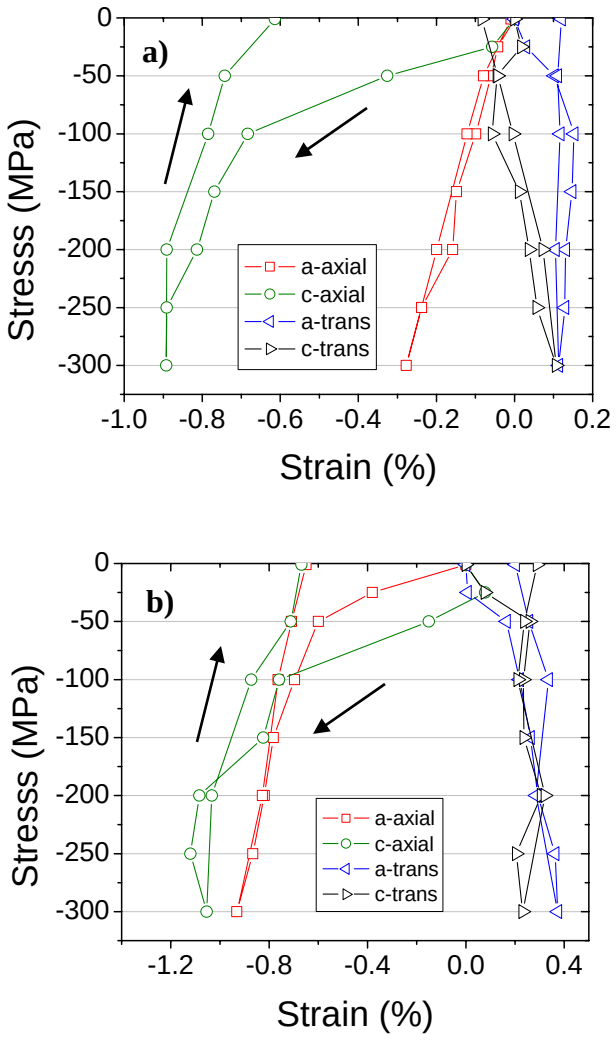


**Figure 2-13**: Axial and transverse lattice strains for the a) tetragonal component and b) rhombohedral component of the morphotropic ceramic sample. Error bars are approximately two times the symbol size and have been omitted for clarity.

Figure 2-13 b shows the lattice strain evolution in the rhombohedral-M phase. Here, the *a* and *c* axes correspond to the [1-10] and [111] directions in the pseudo-cubic unit cell, respectively. It is seen that both *a*-axial and *c*-axial display the expected compressive trend, but for this phase the magnitudes are roughly the same, in contrast to the tetragonal phase. Both of these lattice parameters undergo a relative compliance

change in the domain switching stress range, and exhibit roughly elastic behavior beyond -150 MPa. In the transverse bank where the sampling statistics are hindered, the strain data allow only for the confirmation of a tensile strain trend due to the Poisson effect. Thus for both the tetragonal-M and rhombohedral-M components of the morphotropic composition, the stress range of domain switching corresponds to a differentiated stress state between domains in the pinned and switched configurations. Domains in the pinned orientation undergo a significant softening in the direction of the unit cell aligned with the longitudinal compression axis. Micromechanical interpretation of the tetragonal-M and rhombohedral-M components of the morphotropic compositions must be performed with regard to the single-phase results, and is outlined in the following section.

## 2.5 Conclusions of Neutron Diffraction Studies

A comparison of the behaviors of the individual morphotropic sample components with their single-phase counterparts helps illuminate the complicated internal stress states possible in PZT ceramic materials. These comparisons are summarized in Table 2-10 and displayed graphically in Figures 2-14 and 2-15.

| Symmetry | Single-phase | Morphotropic |
|---|---|---|
| Tetragonal | • Not effectively poled or mechanically de-poled<br>• Lattice strains are linear | • Significant electrical poling and mechanical depoling<br>• *c*-axial lattice strain exhibits softening |
| Rhombohedral | • Effectively poled and mechanically de-poled at sufficiently high stresses<br>• Lattice strains are linear (nearly) | • Switching magnitude similar to single-phase results<br>• Critical stress and "hardness" of the rhombohedral domain switching are both greatly reduced<br>• *a* and *c*-axial lattice strains exhibit softening |

**Table 2-10**: Summary of micromechanical behaviors of the PZT tetragonal and rhombohedral phases in single-phase and morphotropic compositions.

Figure 2-14 a displays the results for the March coefficients of the tetragonal-SP sample along with the tetragonal-M component of the morphotropic sample. In the tetragonal-SP compression test, no evidence of large scale domain switching is present. Thus the relatively extreme switching in the tetragonal-M component of morphotropic sample is surprising. With the presence of a small amount of rhombohedral phase in the ceramic, the tetragonal domains become "unlocked" and exhibit the ability to be poled under electric fields and de-poled by mechanical stress. Additionally, when comparing the strains observed in tetragonal-SP and tetragonal-M specimens under compression (Fig. 2-14 b), we see a clear effect of this domain switching on the stresses experienced by the pinned domains. Domains which are unable to switch in the morphotropic sample (*c* axial) undergo a significant relative softening, presumably due to load transfer from domains which have reoriented themselves in the switched position. The tetragonal-SP specimen exhibits no nonlinearities in the crystal strain response, in accordance with the March coefficient results which indicate no extensive domain switching occurs to initiate

load transfer. The process of domain switching in the tetragonal-M portion of the morphotropic sample, then, has a possible effect of transferring load from domains that switch (in order to accommodate internal stresses) to domains which are pinned in the original poled configuration. Once domains have finished switching, a linear elastic regime is recovered in the pinned orientation.

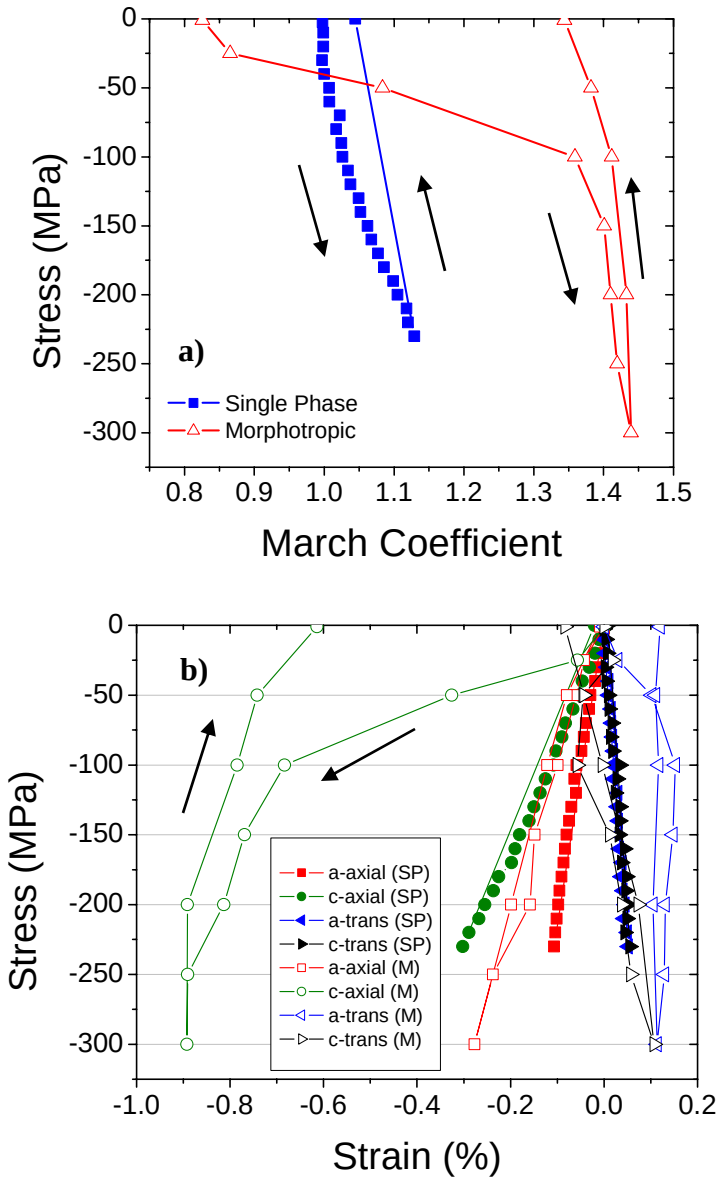


Figure 2-14: Comparison of the tetragonal single-phase (tetragonal-SP) neutron diffraction results with the tetragonal portion of the morphotropic sample (tetragonal-M). a) March coefficients, and b) lattice strains.

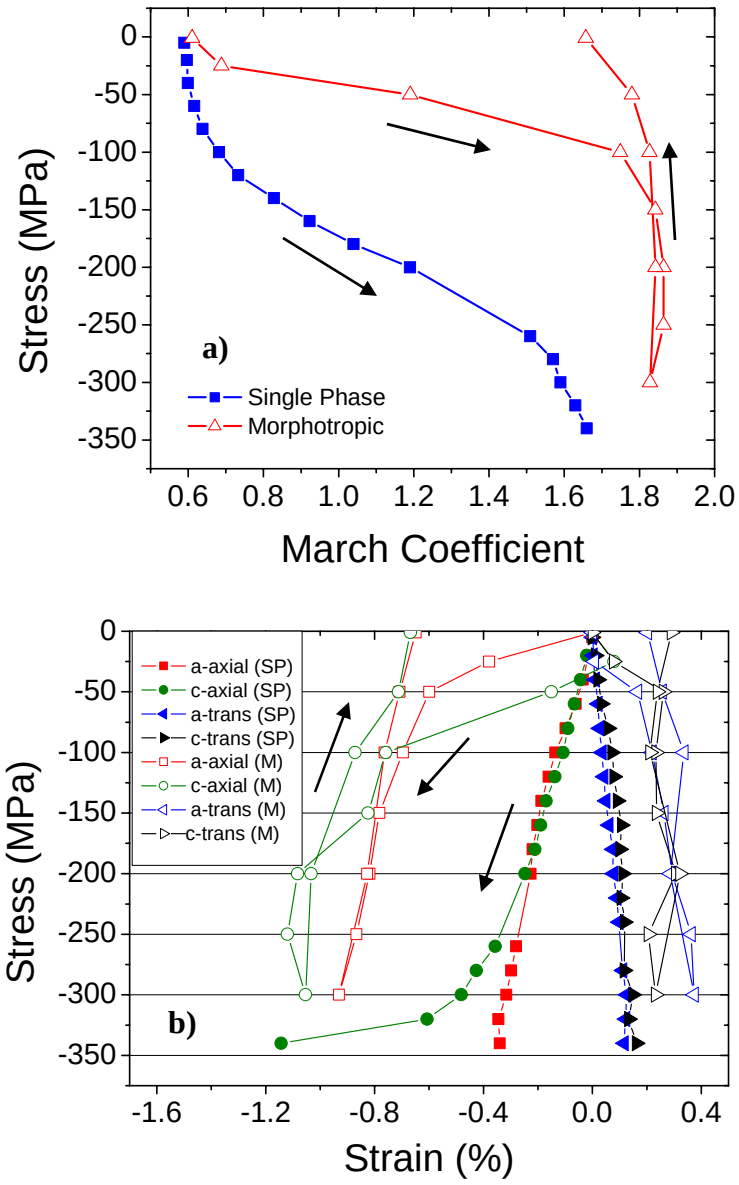


Figure 2-15: Comparison of the rhombohedral single-phase (rhombohedral-SP) neutron diffraction results with the tetragonal portion of the morphotropic sample (rhombohedral-M). a) March coefficients, and b) lattice strains.

Comparing the March coefficient results obtained during the rhombohedral-SP and rhombohedral-M compression tests (Fig 2-15 a), it is clear that both systems undergo large scale domain switching during the poling and de-poling procedures. The rhombohedral-SP specimen, however, requires much larger compressive stresses to

activate domain switching (approximately -125 MPa instead of -25 MPa to induce significant changes in the March coefficient). Once activated, rhombohedral-SP domains do not switch in the "run-away" process observed in the rhombohedral-M sample between -25 and -150 MPa. Instead a more gradual progression of domain switching occurs between -100 and -240 MPa, indicating that the switching behavior of the rhombohedral-SP sample is apparently "harder" than that of the rhombohedral-M sample. Ultimately, conclusive information concerning the differences in constitutive behavior between the single-phase and morpotropic compositions will rely on models (e.g. self-consistent schemes) which accurately reproduce all of the observed diffraction data. Without confirmation of internal micromechanical properties and agreement between model predictions and experiment, final conclusions cannot be absolutely asserted. Still, without the benefit of a micromechanical model, it is possible to sketch a few conceptual mechanisms which may account for all of the observed data.

There are two plausible explanations for the apparent lower stress threshold and softer switching behavior in the morphotropic composition: the presence of tetragonal-M grains in the morphotropic ceramic lowers the energy threshold for switching rhombohedral-M domains (in analogy to lowering the yield strength of a metal), or load transfer from the tetragonal-M phase to the rhombohedral-M phase raises the internal resolved stress on the rhombohedral-M domains. While the first explanation cannot be entirely ruled out, the fact that the tetragonal-M phase comprises 79% of the volume fraction of the morphotropic ceramic would seem to indicate that this phase will dominate the macroscopic stress-strain response of the morphotropic material as well as the internal stress state during loading. The tetragonal-M and rhombohedral-M domain

switching also occur simultaneously in the morphotropic composition (Figure 2-12), which is unexpected given the drastic differences between the tetragonal-SP and rhombohedral-SP switching behavior. Additionally, this switching occurs in a range much lower than the rhombohedral-SP domain switching range (Figure 2-15 a). There are also significant differences between the rhombohedral-SP and rhombohedral-M stress-strain curves (Figure 2-15 b). Strains in the rhombohedral-SP ceramic remain linear during the domain switching process, indicating that the stresses are distributed among domains evenly during loading (i.e., domain switching does not affect the slope of the lattice curves). It is not unreasonable to expect to see the same linear stress-strain relationship during domain switching in the rhombohedral-M component of the morphotropic composition. Instead, in this rhombohedral-M component the *a*-axial and *c*-axial results undergo significant softening during domain switching.

All of these results may be qualitatively accounted for by using the concept of load transfer. If the tetragonal domain switching induces an internal load transfer from switched to unswitched domains in this phase, than this load will also be shared by the rhombohedral component of the system. The internally transferred load raises the resolved stress on the rhombohedral phase domains, inducing domain switching at lower macroscopic stresses than observed in the rhombohedral-SP composition. Additionally, those rhombohedral-M domains which are pinned are subjected to disproportional load in the same way as the tetragonal-M pinned domains. The result is that for the tetragonal-M *c*-axial, rhombohedral-M *a*-axial and *c*-axial lattice strain curves, a relative softening occurs. This cannot be explained as a result of rhombohedral phase domain switching as it is not observed to be a micromechanical property of the rhombohedral-SP ceramic.

While micromechanical modeling will be needed to confirm the presence of load transfer within PZTs, the neutron data seem to indicate that in the morphotropic sample, the addition of the rhombohedral phase allows tetragonal domains to switch in response to the electric poling field. Once mechanically loaded, some of these tetragonal domains switch and transfer load to the entire ceramic system. Apparent compliance changes for lattice directions associated with pinned domains in both the tetragonal-M and rhombohedral-M are a result of this load transfer. As a secondary effect, the load transfer increases the internal resolved stress on the rhombohedral-M domains, effectively lowering the macroscopic mechanical load needed to induce domain switching. The overall effect is a material which can be easily poled electrically, and exhibits superior piezoelectric qualities compared to either the single-phase tetragonal or single-phase rhombohedral composition ceramics.

**Chapter References**

1. Corker, D.L., A.M. Glazer, R.W. Whatmore, A. Stallard, and F. Fauth, *A Neutron Diffraction Investigation into the Rhombohedral Pphases of the Perovskite Series PbZr1-xTixO3.* Journal of Physics-Condensed Matter, 1998. **10**(28): p. 6251-6269.

2. Clausen, B., *Characterisation of Polycrystal Deformation*. PhD. Thesis. 1997, Riso National Laboratory.

3. Bourke, M.A.M., D.C. Dunand, and E. Ustundag, *SMARTS - A Spectrometer for Strain Measurement in Engineering Materials.* Applied Physics A-Materials Science & Processing, 2002. **74**: p. S1707-S1709.

4. March, A., Z. Kristallogr., 1932. **81**: p. 285.

5. Dollase, W.A., *Correction of Intensities for Preferred Orientation in Powder Diffractometry - Application of the March Model.* Journal of Applied Crystallography, 1986. **19**: p. 267-272.

6. Cain, M.G., S.M. Bennington, M.H. Lewis, and S. Hull, *Study of the Ferroelastic Transformation in Zirconia by Neutron-Diffraction.* Philosophical Magazine B-Physics of Condensed Matter Statistical Mechanics Electronic Optical and Magnetic Properties, 1994. **69**(3): p. 499-507.

7. Larson, A.C. and R.B. Von Dreele, *GSAS: General Structure Analysis System*. 1986: Los Alamos National Laboratory, Report No. LAUR 86-748.

8. Rietveld, H.M., *A Profile Refinement Method for Nuclear and Magnetic Structures.* Journal of Applied Crystallography, 1969. **2**: p. 65.

9. Young, R.A., ed. *The Rietveld Method*. 1993, Oxford University Press: New York.

10. Jaffe, B., W.R. Cook, and H. Jaffe, *Piezoelectric Ceramics*. 1971, London: Academic Press.

11. Bedoya, C., C. Muller, J.L. Baudour, V. Madigou, M. Anne, and M. Roubin, *Sr-Doped $PbZr_{1-x}Ti_xO3$ Ceramic: Structural Study and Field- Induced Reorientation of Ferroelectric Domains.* Materials Science and Engineering B-Solid State Materials for Advanced Technology, 2000. **75**(1): p. 43-52.

12. Frantti, J., J. Lappalainen, S. Eriksson, V. Lantto, S. Nishio, M. Kakihana, S. Ivanov, and H. Rundlof, *Neutron Diffraction Studies of $Pb(Zr_xTi_{1-x})O_3$ Ceramics.* Japanese Journal of Applied Physics Part 1-Regular Papers Short Notes & Review Papers, 2000. **39**(9B): p. 5697-5703.

13. Wilkinson, A.P., J. Xu, S. Pattanaik, and S.J.L. Billinge, *Neutron Scattering Studies of Compositional Heterogeneity in Sol-Gel Processed Lead Zirconate Titanates.* Chemistry of Materials, 1998. **10**(11): p. 3611-3619.

14. Rogan, R.C., E. Ustundag, B. Clausen, and M.R. Daymond, *Texture and Strain Analysis of the Ferroelastic Behavior of Pb(Zr,Ti)O-3 by In Situ Neutron Diffraction.* Journal of Applied Physics, 2003. **93**(7): p. 4104-4111.

15. Tsurumi, T., Y. Kumano, N. Ikeda, N. Ohashi, and O. Fukunaga, *XRD Measurement of 90 Degrees Domain Reorientation and Domain Contribution to the Electric-Field-Iinduced Strain in PZT Ceramics*, in *Electroceramics in Japan I*. 1999. p. 73-79.

16. Li, X.P., W.Y. Shih, J.S. Vartuli, D.L. Milius, I.A. Aksay, and W.H. Shih, *Effect of a Transverse Tensile Stress on the Electric-Field- Induced Domain*

*Reorientation in Soft PZT: In Situ XRD Study.* Journal of the American Ceramic Society, 2002. **85**(4): p. 844-850.

17. Berlincourt, D., *Piezoelectric Ceramic Compositional Development.* Journal of the Acoustical Society of America, 1992. **91**(5): p. 3034-3040.

18. Fernandes, J.C., D.A. Hall, M.R. Cockburn, and G.N. Greaves, *Phase Coexistence in PZT Ceramic Powders.* Nuclear Instruments & Methods in Physics Research Section B- Beam Interactions with Materials and Atoms, 1995. **97**(1-4): p. 137-141.

19. Endriss, A., M. Hammer, M.J. Hoffmann, A. Kolleck, and G.A. Schneider, *Microscopic and Macroscopic Ferroelectric-Ferroelastic and Piezoelectric Behavior of PZT Ceramics.* Journal of the European Ceramic Society, 1999. **19**(6-7): p. 1229-1231.

20. Ogawa, T. and K. Nakamura, *Poling Field Dependence of Ferroelectric Properties and Crystal Orientation in Rhombohedral Lead Zirconate Titanate Ceramics.* Japanese Journal of Applied Physics Part 1-Regular Papers Short Notes & Review Papers, 1998. **37**(9B): p. 5241-5245.

21. Berlincourt, D. and H. Jaffe, *Elastic and Piezoelectric Coefficients of Single-Crystal Barium Titanate.* Physical Review, 1958. **111**(1): p. 143-148.

22. Zgonik, M., P. Bernasconi, M. Duelli, R. Schlesser, and P. Gunter, *Dielectric, Elastic, Piezoelectric, Electro-Optic, and Elasto-Optic Tensors of $BaTiO_3$ Crystals.* Physical Review B, 1994. **50**(9): p. 5941-5949.

23. Calderon-Moreno, J.M., *Stress Induced Domain Switching of PZT in Compression Tests.* Materials Science and Engineering a-Structural Materials Properties Microstructure and Processing, 2001. **315**(1-2): p. 227-230.

24. Calderon-Moreno, J.M., *Stress-Induced Domain Switching of PZT Subjected to Cyclic Uniaxial Compression*, in *Euro Ceramics Vii, Pt 1-3*. 2002. p. 1445-1448.

# Chapter 3

## Macroscopic X-ray Diffraction Experiments

### 3.0 Introduction: 2-D Diffraction of PLZT Under Electric Field

The formulation of robust models for ferroelectric materials requires knowledge of their *multiaxial* crystallographic behavior under mechanical and electrical loading. Specifically, it is desirable to obtain, as a function of applied electromechanical loads, quantitative data of the microscopic strain states which are functions of single crystal elastic properties, domain switching, and fatigue effects. While the neutron diffraction experiments described in Chapter 2 are capable of simultaneous probing longitudinal and transverse constitutive behavior, a more thorough coverage of the angularly dependent material response is desired. As part of this ongoing investigation into the constitutive behavior of ferroelectrics, a novel high-energy synchrotron diffraction technique was applied to the study of a complicated relaxor material. Due to the use of transmission geometry and a 2-D detector, complete two-dimensional constitutive behavior of a ferroelectric ceramic under electric field cycling was observed.

$(Pb_{1-x}La_x)(Zr_{1-y}Ti_y)O_3$ (PLZT) crystalline solutions are of interest both for their ferroelectric and electro-optic properties. Increasing amounts of La doping in these materials has been shown to alter ferroelectric responses and produce relaxor behavior, characterized by a frequency dispersion in the dielectric response and slim loop hysteresis behavior in the vicinity of the dielectric maxima [1-3]. Pair distribution function analyses

of time-of-flight neutron diffraction data indicate that the local crystallographic structure of PLZT is affected by the amount of La doping, leading to the break down of the ferroelectric coupling mechanisms which would normally produce long range crystal order [4, 5]. Significant microstructural changes accompany this normal-to-relaxor ferroelectric transition. For the nominally rhombohedral $(Pb_{1-x}La_x)(Zr_{0.65}Ti_{0.35})O_3$ composition, several TEM studies have confirmed the general trend with increased La doping is from μm sized rhombohedral ferroelectric domains ($x < 5$ % at.), toward fine "tweed-like" structures consisting of textured nanodomains ($5 < x < 7$ % at.), and finally to randomly organized polar nanodomains ($x > 7$ % at.) [1, 2, 6-9].

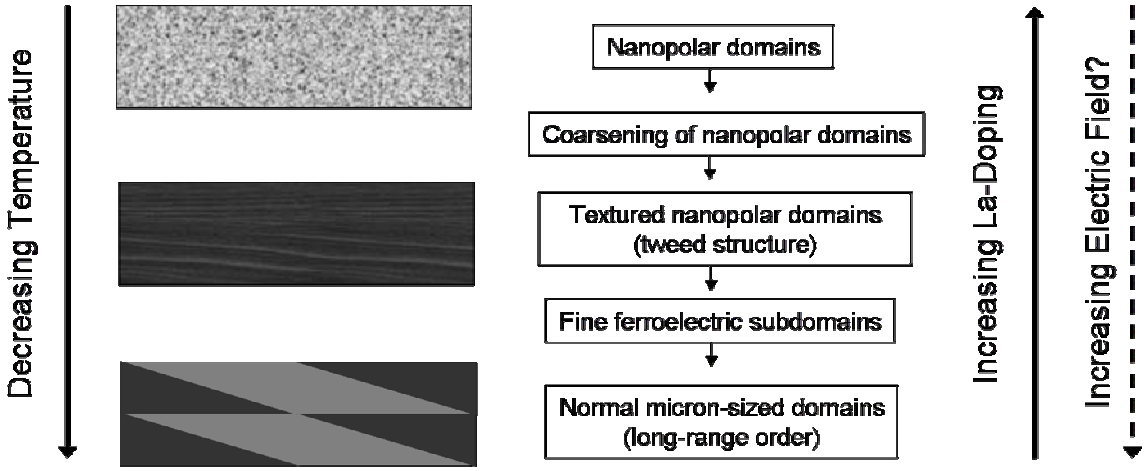


Figure 3-1: *After Tan and Viehland* [3] *and Akbas,* et al. [9]. Schematic indicating the various microstructural states of the PLZT system. Boxes are a cartoon mimicking the general images observed using TEM: nanodomains exhibit mottled contrast (top), tweed structures display organized variation in one direction, but with no strict adherence to periodicity (middle), and normal micro-sized domains form large, clear regions of contrast between domain variants exhibing long-range crystal order (bottom).

The polar nanodomain state is characterized by cubic average symmetry at the macroscopic level (μm), although at the smallest scale it consists of nanometer size

rhombohedral crystallites which are distorted and misoriented due to the presence of oxygen octahedral tilt disorder induced by the addition of La ions (and subsequently vacancies resulting from charge neutrality requirements) [10-13]. Several studies have noted the relative instability of the various microstructural states of x/65/35 PLZT as a function of temperature, La doping, stress, and electric field. Compositions which are associated with nanodomain microstructures at room temperature undergo "coarsening" as temperature is decreased, and eventually a textured nanodomain microstructure will form (tweed) [1-3, 8]. Dai *et al.* found evidence of a long time relaxation process in 6/65/35 PLZT resulting in a transformation from a tweed microstructure (exhibiting relaxor behavior) to a long-range ordered (LRO) ferroelectric state at room temperature [14, 15]. For x > 7% at., however, no evidence for the development of rigorous long-range ferroelectric order as a function of temperature has been found, reflecting a stabilization of relaxor behavior [3, 11, 14]. Thus an 8% at. La content (8/65/35 PLZT) is sufficient to insure that a polycrsytalline specimen will consist of grains possessing only polar nanodomains at room temperature after zero field cooling (ZFC) [2, 9, 11], with the expectation that the nanodomain relaxor state is stable as a function of temperature.

The effect of electric fields on PLZT materials has been studied extensively using TEM analysis and various macroscopic measurements of the electromechanical and dielectric responses. Keve and Bye were the first to suggest that PLZT may undergo a phase transition during electrical poling [16], while early studies by Michel and Sicignano observed a transition under the influence of electric field from a random microstructure to an organized lamellar structure in 8/65/35 PLZT [17]. More recently, the formation of finely aligned domains (or tweed structure) from a random nanodomain

state was directly observed in 8/70/30 PLZT using *in situ* TEM to study the effects under electric field [8]. Xi *et al*. performed dielectric measurements on ZFC PLZT samples heated under a bias field and found evidence for a build up of normal ferroelectric domains from polar nanodomains, which would correspond to the development of long-range rhombohedral crystal structure [10].

In order to investigate the crystallographic response of PLZT to exterior forces, information from a large *d*-spacing range is necessary to observe possible phase transformations. Because ferroelectric materials are by definition non-linear and anisotropic, it is also desirable to record information from as much larger or wider angular space as possible to determine the multiaxial constitutive behavior. This chapter reports the use of high-energy synchrotron radiation for the *in situ,* biaxial study of bulk crystallographic behavior in a polycrystalline PLZT composition under electrical loading at room temperature.

### 3.1 Experimental Procedure

Commercially available PLZT 8/65/35 hot pressed ceramic polycrystal was obtained from Alpha Ceramics Inc., (5121 Winnetka Avenue North, Minneapolis, MN 55428, USA). Grain size of the transparent ceramic material was ~ 3-6 μm, with a Curie temperature of approximately 110°C. The PLZT was obtained in bulk form in the unpoled state and diced using a diamond wafering saw to produce the final specimen size of 2 x 3 x 10 $mm^3$. The two large specimen surfaces were polished to a 1μm finish using diamond paste, and silver electrode paint was applied to yield surface electrodes that would induce electric fields across the 3 mm sample direction.

A $CeO_2$ powder standard was attached to the sample for calibration purposes. The specimens were suspended in the path of the X-ray beam in transmission geometry at end station 1-ID-C of the Advanced Photon Source (Argonne National Laboratory, USA). The sample's large surfaces were aligned normal to the X-ray transmission axis, thus the electrical loading axis was oriented perpendicular to the X-ray beam (along the $\eta = 0°$ axis of the detector, Figure 3-2 and 3-3). High energy (80 keV, $\lambda = 0.0153$ Å) X-rays were selected for maximum penetrating power, and a large 100 x 50 $\mu m^2$ beam was used to insure complete powder average statistics. Data were collected on a Mar345 digital image plate detector (MarUSA, Inc., 1840 Oak Ave., Evanston, IL 60201 USA) with an active area diameter of 345 mm. This allowed for the capture of full Debye rings from *d*-spacing ranges of approximately 1.3 - 4.2 Å. Experimental geometry was calibrated using the $CeO_2$ standard diffraction patterns and the Fit-2D program [18]. Specifically, the $CeO_2$ standard calibrates the conversion of radial distances on the detector into *d*-spacing, thus providing an absolute *d*-spacing scale for sample measurements.

The sample was initially poled using a high voltage source to apply electric fields in steps of -0.09 kV/mm to a maximum field of -0.9 kV/mm (the poling field). Subsequently, the field was varied in steps of ± 0.09 kV/mm to complete one full polarization cycle ranging from -0.9 to 0.9 kV/mm. Diffraction patterns were recorded while the specimen was held at constant electrical field level. Exposure time was 1 minute per pattern, but due to data throughput limitations the sample was held at each field value for approximately 3 minutes prior to new data acquisition. Thus the electrical field cycling frequency corresponded to approximately $4 \times 10^{-4}$ Hz.

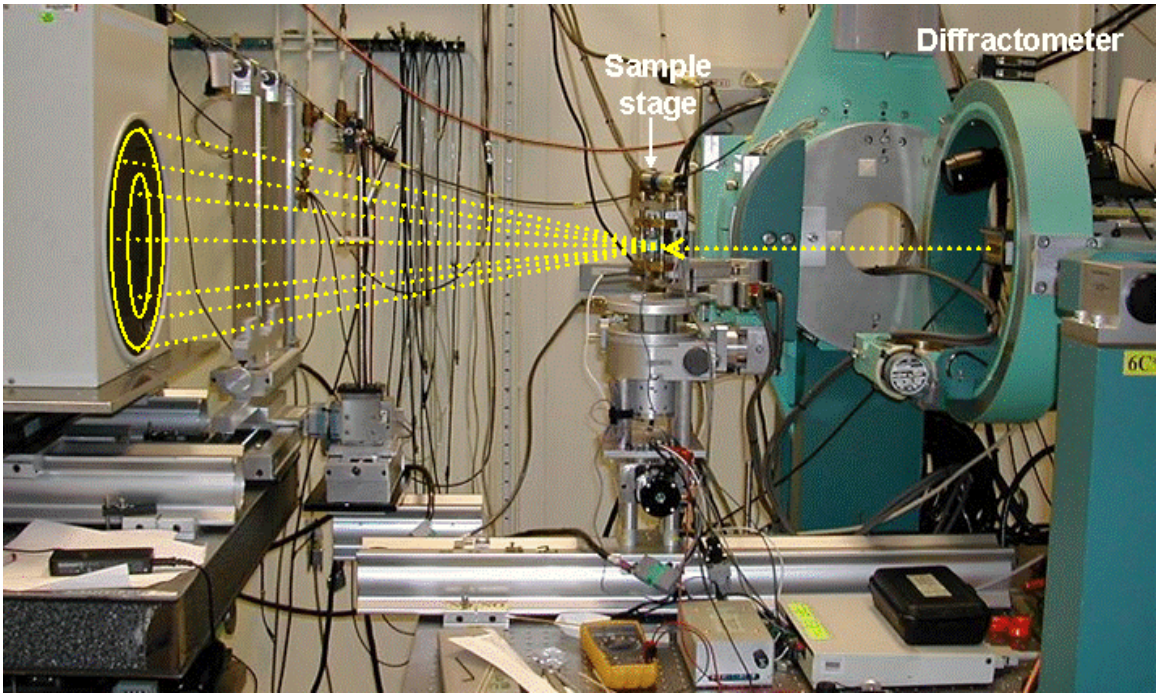


Figure 3-2: Experimental geometry for transmission mode 2-D diffraction experiments. High energy monochromatic beam is normal to sample surface, and the image plate dector captures the full Debye rings.

Using the program Fit-2D, each pattern of Debye rings was divided into 36 azimuthal slices by integrating across 10° ranges in η (Figure 3-3). Each integration produced a diffraction pattern indicating intensity as a function of *d*-spacing for a given angle η. This process essentially creates 36 virtual detectors, each of which corresponds to a specific 10° angular range of material structural behavior. These diffraction patterns were then analyzed using the Rietveld method [19] and the GSAS software package [20]. Details of the analysis are given in the following sections.

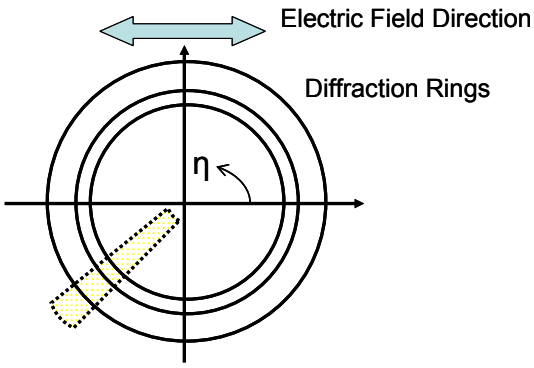


Figure 3-3: Coordinates for Debye ring "caking" of 10° azimuth ranges, resulting in 36 total virtual detectors.

## 3.2 Data Analysis and Discussion

### 3.2.1. Whole Pattern Analysis of PLZT

Initial attempts at full pattern crystal structure refinements met with mixed success. Without La doping, $Pb(Zr_{0.65}Ti_{0.35})O_3$ lies squarely in the rhombohedral phase region of the PZT phase diagram [21]. As in any PZT system, rhombohedral and tetragonal phases are known to coexist at compositions near the morphotropic phase boundary [21]. The addition of La shifts the morphotropic phase boundary for undoped-PZT (normally lying at a zirconium-titanium ratio of ~ 52/48) to a region near the 8/65/35 PLZT composition [22]. While both tetragonal and rhombohedral distortions have been clearly identified in certain compositions of PLZT possessing LRO [15, 23], as mentioned above, compositions which are composed of a nanodomain microstructure (as is the case in 8/65/35) are observed to have an average cubic crystal symmetry [11].

Upon initial inspection, the structure of the PLZT specimen appeared generally cubic in the zero field condition ($E = 0$) with well defined peaks (Figure 3-4). Thus diffraction patterns for the $\eta = 0°$ azimuth at $E = 0$ were first simulated using the standard

cubic perovskite space group *P4mm*, with imposed restrictions on the atomic positions and lattice parameters which would insure a cubic structure. A thorough refinement of the cubic lattice parameter, background, absorption, peak shape, and thermal parameters produced accurate peak positions. Peak intensities, however, were poorly modeled for certain reflections (Fig. 3-4). The best refinement for $\eta = 0°$ at $E = 0$ yielded residuals of $R_p \sim 15\%$ and $R_{wp} \sim 20\%$. These numbers are clearly unsatisfactory in terms of regular Rietveld refinements, prompting the investigation of several other possible space group descriptions to improve fitting residuals. Fits using the slight distortions of the cubic unit cell into the orthorhombic *Amm2* ($R_p = 14\%$ and $R_{wp} = 19\%$) and rhombohedral *R3c* ($R_p = 38\%$ and $R_{wp} = 52\%$) structures were unsatisfactory in addition to being highly unstable (convergence was not regularly achieved). Combinations of cubic, orthorhombic, and rhombohedral phases did not significantly improve upon the basic cubic model. The structural disorder in ZFC 8/65/35 PLZT noted in previous studies may have significant impact on the apparent structure factors associated with certain lattice reflections. Without strict crystallographic order existing on significant length scales, scattering events would not necessarily conform to the kinematic approximation, and thus the total diffracted intensity for any given peak may not match simulations employing kinematic diffraction physics (such as Rietveld). In order to check whether the influence of electric field could activate a LRO rhombohedral phase transformation, a diffraction pattern taken from the poled state was also analyzed using the above method. Here again, the cubic approximation yielded the most satisfactory results. Thus it seems that the presence of polar nanodomains significantly clouds the use of any single space group for accurate

crystal structure identification; a concept which will be examined more thoroughly in the next section.

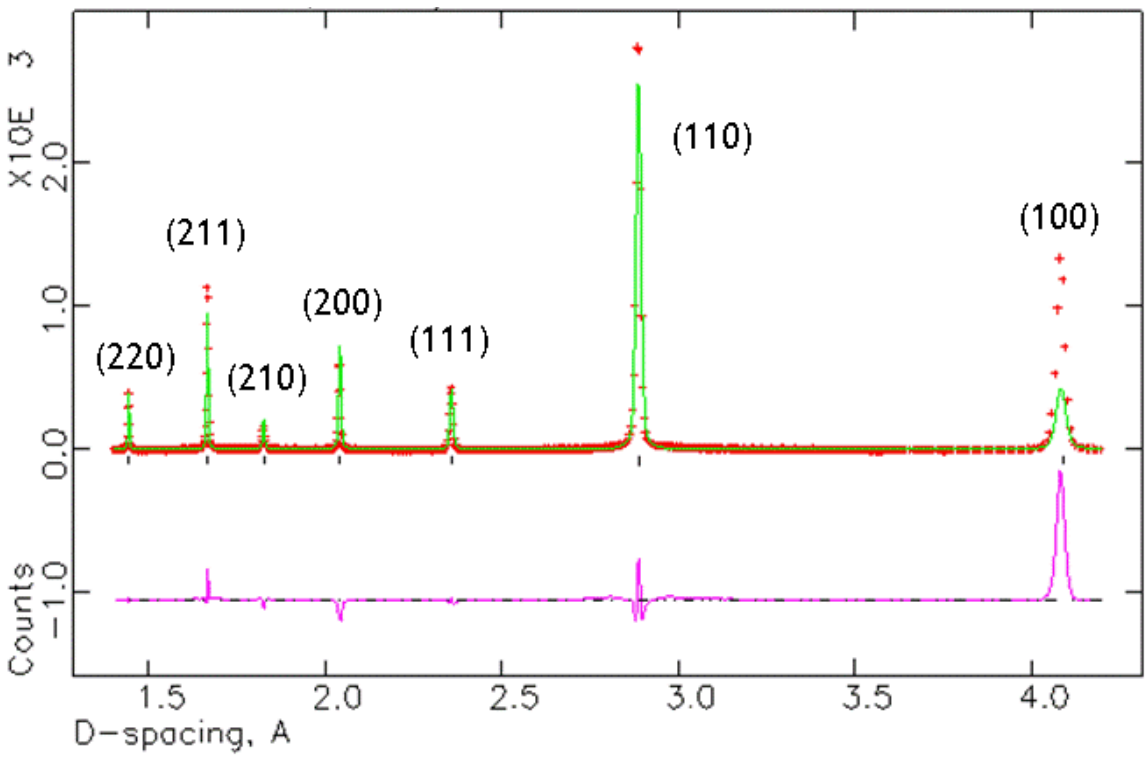


Figure 3-4: Typical diffraction pattern for the unpoled 8/65/35 PLZT sample. Labels indicate pseudo-cubic reflection indices. Crosses are the raw diffraction data, curve fit is from the simplified cubic crystal structure model, and lower curve is the difference between observed and simulated patterns.

Despite the cubic model's shortcomings in simulating certain peak intensities, the peak positions were satisfactorily accurate. Thus in an effort to estimate the PLZT specimen's strain response to electrical field, the cubic structure approximation was applied to all electrical loading data. While the structure of the PLZT specimen cannot be claimed to be strictly cubic, the simplicity and stability of the cubic model allowed for consistent, comparable refinements for all electrical loads and the entire 360° range of η. When considered as a whole, the average fitting residuals for all azimuthal angles and all

electrical loads were $R_p \sim 12\%$ and $R_{wp} \sim 18\%$. Strains for each angle η were calculated relative to the zero field lattice parameters obtained for that angle. Calculating strains in this manner eliminates any systematic error induced by the $CeO_2$ calibration, grinding and polishing effects, and "graininess" of the material. Any of these effects may cause *d*-spacing error from one azimuthal angle to the next due to slight differences in diffraction peak location, thus it is important to calculate strains for each azimuthal angle from a reference obtained for that azimuthal angle. In this way, the strains at different η angles may be compared.

Strain results from the initial poling process using the cubic approximation are displayed in Figure 3-5. Each curve represents an angle η with respect to the direction of the applied electric field (applied at $\eta = 0°$, Fig. 3-3). The lattice strains remain nearly constant near zero level until a field of approximately -0.33 kV/mm is reached, at which point they diverge. For $\eta < 45°$, the electric field induces tensile strains corresponding to the average elongation of the unit cell as the electric field is increased. The maximum tensile strain observed in the poled material is 0.22%, and occurs in the parallel direction of the electric field at $\eta = 0°$. Material aligned at angles corresponding to $\eta > 45°$ experiences compressive strains due to the Poisson effect. Note that the curve corresponding to $\eta = 90°$ does not display the maximum compressive strains achieved after poling (the max is -0.1% for $\eta = 80°$) suggesting that the applied electric field may not be exactly parallel with the $\eta = 0°$ axis. Since the $\eta = 0°$ lattice strain measurement does exhibit the maximum tensile strain, the field cannot be more than 10° askew. Thus the best estimate that can be formed is that the electric field axis truly lies at an angle of -3° to -7°.

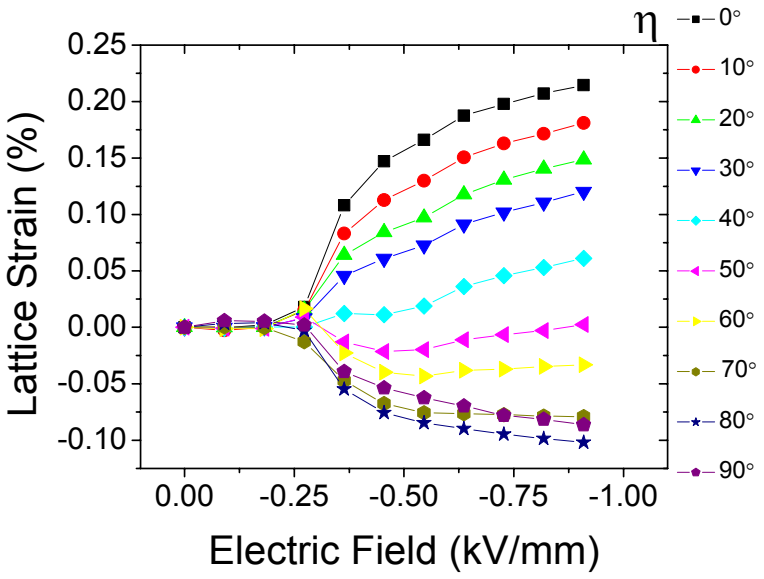


Figure 3-5: Cubic lattice strains as a function of angle with respect to the electric field (η) measured during the initial poling process. Error bars for all curves are approximately 2 times the symbol size, and have been omitted for clarity.

Measuring the total strain induced at -0.9 kV/mm (the furthest points in Fig. 3-5) as a function of azimuthal angle yields the polar plot shown in Figure 3-6. The results are symmetric in shape regardless of angular quadrant, with maximum tensile strains occurring around $\eta = 0°$ and 180°, and maximum compressive strains near $\eta = 90°$ and 270°. The crossover from tensile to compressive behavior occurs at roughly $\eta \approx 55°$, 125°, 235° and 295° (as estimated by the half point between two azimuthal measurements). With the exception of the crossover at 295°, all of the zero strain points lie at relative angles of ±55° to the electric field axis. After the poling of the PLZT specimen was finished, a complete electrical cycle was undertaken. Strain results using the cubic approximation are shown in Figure 3-7 for the two representative angles $\eta = 0°$ and 90°. The traditional ferroelectric "butterfly loop" shape is evident in both tension and compression, with coercive fields occurring at approximately ± 0.33 kV/mm (as measured by the inflection points on the butterfly loops). While this value is small

compared to the macroscopically obtained measurements of 0.5 kV/mm observed by Li *et al* [2], it is only slightly smaller than value of 0.36 kV/mm reported by Lynch [24]. Variations in the measured $E_c$ of relaxor materials as a function of applied field frequency have been observed in previous studies, in addition to long relaxation times for polarization equilibrium in PLZT under dc fields less than the coercive field [25, 26]. Because of the relatively slow cycling time (~ 4 x $10^{-4}$ Hz) and long times spent at each load level, we would expect to measure somewhat low coercive fields in our experiment. Additionally, it has been shown that 8/65/35 PLZT needs several electrical cycles before fully relaxing into highly repeatable hysteretic behavior [24]. Still, Figure 3-7 demonstrates the power of the 2-D X-ray diffraction technique, as it represents only a sample of the 36 butterfly loops obtained. By taking 1 minute exposures at each electrical load, the complete biaxial strain behavior of the material can be obtained. Through using the virtual detector setup, we can simultaneously measure the response of PLZT poled in 36 different directions to cyclic electric fields.

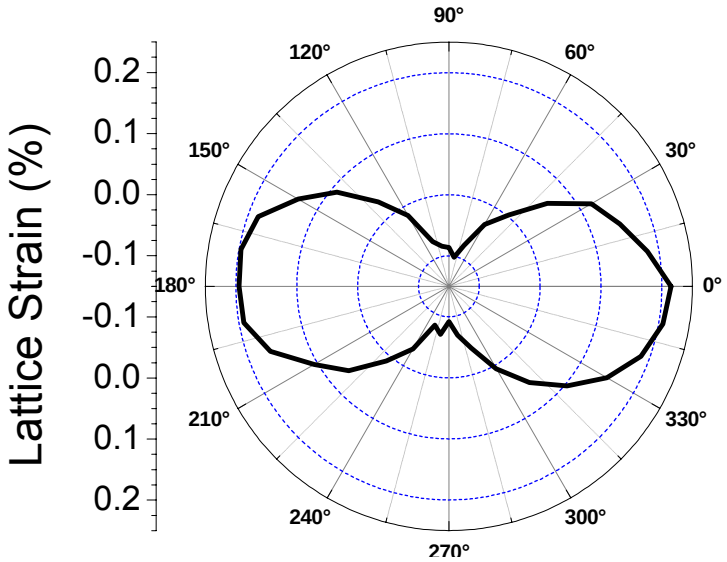


Figure 3-6: Distribution of cubic lattice strains as a function of angle with respect to the electric field (η) measured at the maximum poling field (~0.9 kV/mm). Matching radial distances along the 90° axis to the scale (left) gives strain values. Note that the circle origin does not correspond to "zero" strain, but rather -0.15 % strain, so that both tensile and compressive strains may be displayed simultaneously.

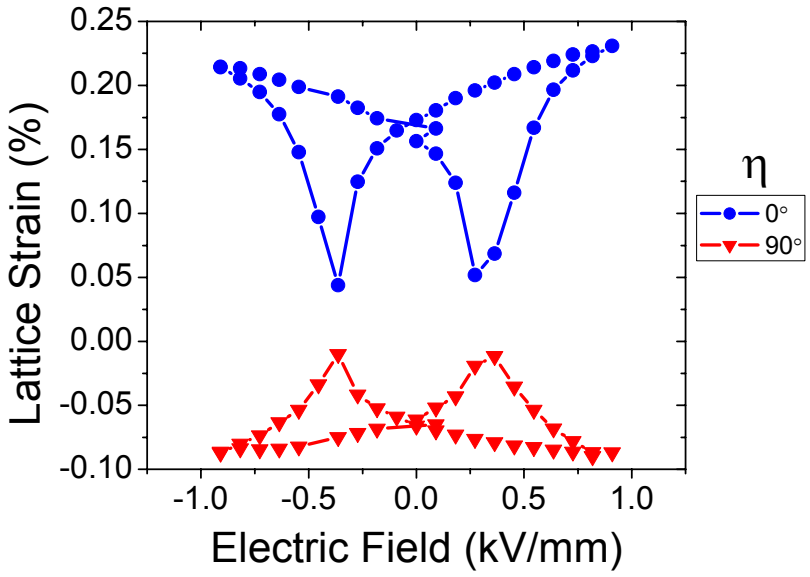


Figure 3-7: Cubic lattice strains as a function of electric field measured during electric cycling for directions parallel (η = 0°) and perpendicular (η = 90°) to the electric field direction. Error bars for all curves are approximately 2 times the symbol size, and have been omitted for clarity.

Despite the lack of a clear crystal space group for PLZT and the deficiencies of the cubic approximation, several aspects of the constitutive behavior of this material may be analyzed using this simplification. The 2-D X-ray diffraction experimental technique is capable of simultaneously probing the *in situ* multiaxial behavior of ferroelectrics over a wide degree of angular space. Much specific information concerning the behavior of PLZT, however, is unavailable due to the lack of long-range crystal structure. Material texture, which is measured from peak intensity changes, cannot be reliably extracted from a Rietveld analysis which incorrectly models peak intensities. The imposition of a cubic structure also prevents the absolute correct modeling of peak positions if a phase transformation, ferroelectric ordering, or other asymmetric strain processes occur which would induce peak shape distortions. In order to probe more deeply into the specifics of

this material's response to electrical load, single peak analysis was undertaken to address these issues.

### 3.2.2 Single Peak Analysis of PLZT

All seven major peaks recorded in the diffraction spectra were fit individually resulting in data for position, intensity, and width. All peaks will be referred to their cubic indexations (Figure 3-4) for simplicity and clarity. Results for single peak strains and normalized intensity variations at $\eta = 0°$ observed during the initial poling process are shown in Figures 3-8 a and b. Two immediate conclusions may be drawn from these results. The first is that the structure of PLZT is, as expected, not an ideal cubic perovskite as evidenced by the differences between strains in harmonic peaks. Because strain is a unitless, normalized quantity, the pseudo-cubic (100) and (200) strain as well as the (110) and (220) strain curves should display identical values if crystal structure were truly cubic. The second conclusion is that the material does not exhibit behavior consistent with a rhombohedral structure at any point in the electrical cycling.

Previous studies using a multitude of techniques have shown that $(Pb_{1-x}La_x)(Zr_{0.65}Ti_{0.35})O_3$ compositions with x between 0.07 and 0.09 may undergo an electric field driven transition from the random nanopolar domain state to a textured nanodomain state (tweed) [8, 17], and it has been suggested that a LRO rhombohedral ferroelectric state may even form [1, 10]. Here again, it is useful to employ the concept of a pseudo-cubic unit cell to discuss the diffraction phenomena in the rhombohedral phase. The pseudo-cubic unit cell is defined as the room-temperature distortion in the high-temperature cubic phase unit cell induced by the cubic-to-rhombohedral phase

transition. As noted in Chapter 2, regular rhombohedral ferroelectrics possess polarizations along their [111] pseudo-cubic unit cell directions due to the displacement of positive and negative charge centers in the unit cell. Electric fields interact with these [111] dipoles through the piezoelectric effect to induce large strains for any domains oriented such that their [111] directions are parallel (or near parallel) with the field direction. Additionally, above the $E_c$, rhombohedral ferroelectric domains will switch orientations in an attempt to more closely align their [111] directions with the electric field, producing a greater number of (111) scattering sites and yielding intensity increases in the (111) diffraction peak measured with a diffraction vector ($Q$) parallel to the electric field direction. Thus if a LRO rhombohedral ferroelectric phase developed during the application of electric field, at $\eta = 0°$ ($Q$ vector parallel to the electric field) we would expect to observe large tensile strains in the (111) cubic peak accompanied by a significant increase in peak intensity. In Fig. 3-7 b, no such increase with electric field is observed.

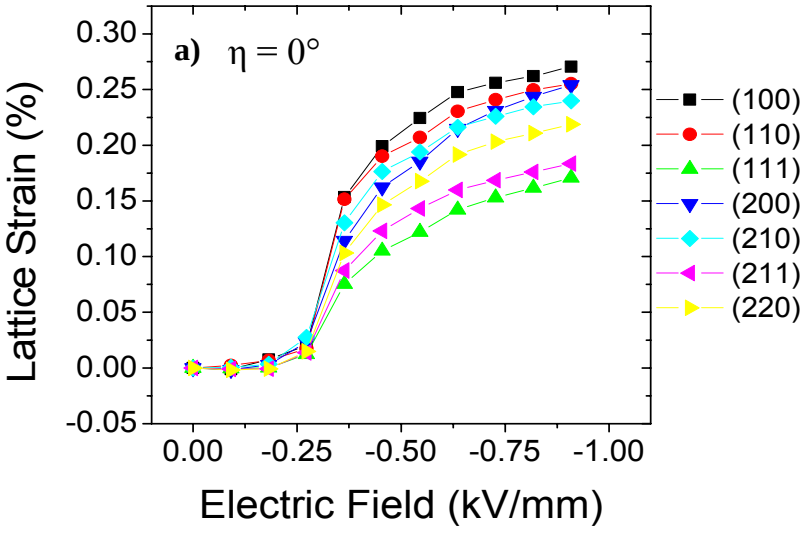


Figure 3-8: a) Single peak strains as a function of electric field measured during electrical poling along the $\eta = 0°$ direction. b) (next page) Normalized intensity as a function of electric field measured during electrical poling process along the $\eta = 0°$ direction. Error bars for all curves are approximately two times the symbol size, and have been omitted for clarity.

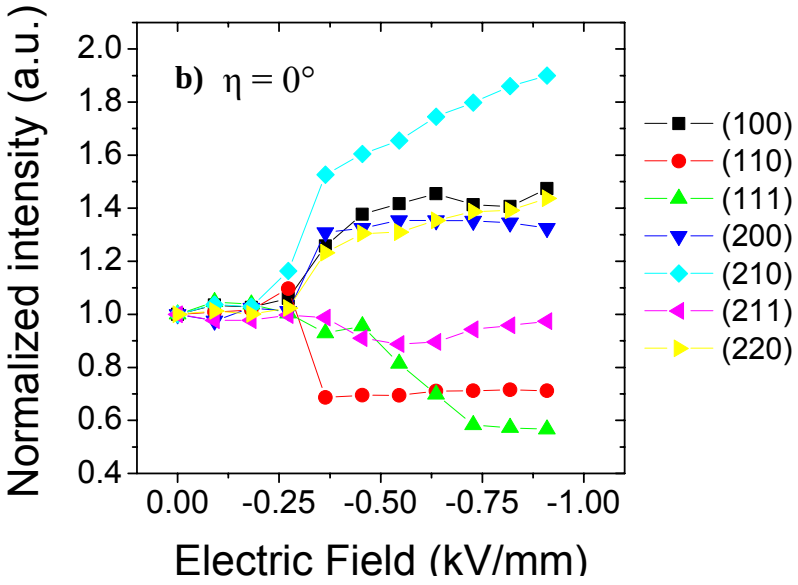


In Figure 3-8 a, the (111) strain curve does not exhibit the maximum observed strains (it in fact maps the lowest measured values). If a LRO transformation occurred (i.e. μm sized ferroelectric domains formed from a nanodomain matrix) drastic tensile strains would be observed in the (111) peak associated with the lengthening of the unit cell dipoles in this direction due to the piezoelectric effect. The intensity results (Fig. 3-8 b), which indicate material texture and thus are a measure of ferroelectric switching, lend credence to the concept that 8/65/35 PLZT does not undergo a systematic long range ferroelectric ordering transition under electric field. A LRO ferroelectric crystal will produce well defined structure factors and predictable intensity fluctuations as a result of material texture. After poling was complete, no evidence of pseudo-cubic [111] direction alignment with the electric field is observed in the $\eta = 0$ normalized intensity plot (Figure 3-8 b). If macroscopic ferroelectric rhombohedral domains formed from a nanodomain matrix, we would expect their pseudo-cubic [111] directions to align with the electric field and contribute disproportionate intensity to the (111) peak in the $\eta = 0°$ range.

Instead, we observe a roughly constant normalized intensity for the (111) diffraction peak.

Comparing the results of the poling strains and intensities for $\eta = 0°$ and $\eta = 90°$ (Figure 3-9), it is evident that the nature of the material response parallel to the electric field is quite different than that perpendicular to the field. The relative order of strains exhibited by each pseudo-cubic diffraction peak in the tensile $\eta = 0°$ data are not reproduced in the compressive $\eta = 90°$ results. For example, while the (110) diffraction peak displays large tensile strains parallel to the electric field, perpendicular to the field only a relatively small compressive strain is observed. In addition to the previously noted divergence of strains in harmonic reflections, this is clear evidence that there is a significant anisotropic strain process at work during the poling procedure (with respect to a cubic setting).

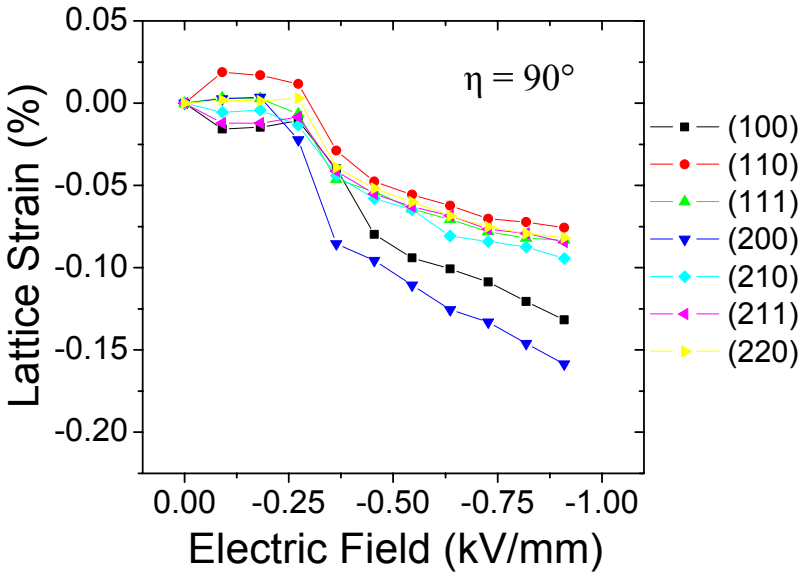


Figure 3-9: Pseudo-cubic single peak strains as a function of electric field measured during electrical poling along the $\eta = 90°$ direction. Error bars for all curves are approximately two times the symbol size, and have been omitted for clarity.

The information obtained from single peak width measurements convolutes the general picture thus far sketched. Here again, data were normalized by the ZFC peak width results for each individual peak in order to allow for direct comparison between the various reflections (Figure 3-10). As the sample is poled, there is a marked separation in trends of the normalized peak widths measured parallel to the electric field. Of specific interest are the dramatic increases in the width of the (200) peak and {110} family peaks. The broadening in the {110} family of peaks has been observed in previous studies of relaxor PLZT compositions and is commonly attributed to a developing rhombohedral phase [14, 15]. During a cubic (space group *Cm*) to LRO rhombohedral (space group *R3c*) phase transition, the cubic (220) peak (denoted $(220)_C$) splits to form the (220)-(208) doublet of the rhombohedral phase ($(220)_R$ and $(208)_R$). It is important to realize, however, that the psueo-cubic-to-rhombohedral transformation is *not* expected to produce doubling of the $(200)_C$ peak (where $(200)_C \rightarrow (20\bar{4})_R$).

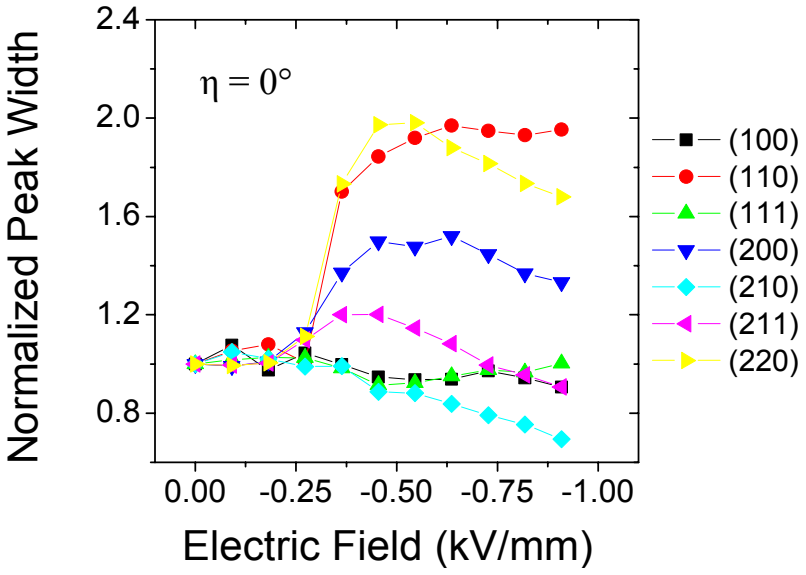


Figure 3-10: Normalized pseudo-cubic single peak widths as a function of electric field measured during electrical poling along the η = 0° direction. Error bars for all curves are approximately two times the symbol size, and have been omitted for clarity.

Visual examination of the $(220)_C$ peak at various electrical field levels confirmed the presence of the "shoulder" noted by other authors (not shown), but the degree of peak overlap prevented an accurate modeling of the $(220)_C$ peak as the $(220)_R$ - $(208)_R$ doublet peak of an emerging rhombohedral phase. In order to examine the behavior of single reflections across all azimuthal angles, raw peak width data are appropriate. Figure 3-11 displays the raw peak width measurements for the $(220)_C$ reflection before and after poling. The inner curve represents the zero-field width measurements, which display no significant dependence on $\eta$, while the outer curve plots the poled condition width measurements and exhibits a "dog-bone" shape. Note that the maximum peak widths observed in the dog-bone occur approximately between the values of $\eta = \pm 20°$ to $\pm 30°$ to the electric field direction. If we assume that the rhombohedral distortion is vanishingly small (approaching the perfectly cubic case), then the angle between the $(111)_C$ and $(220)_C$ crystal planes is ~ 35°. Therefore, if the application of an electric field causes the formation of crystal regions exhibiting rhombohedral symmetry aligned with their $(111)_C$ dipole directions along the electric field axis, the $(220)_C$ diffraction information from these crystallites would lie at $\eta \approx \pm 35°$ relative to this axis. In reality, if a rhombohedral distortion of the cubic unit cell is activated, the angle between the $(111)_C$ and $(220)_C$ pseudo-cubic lattice planes will shrink, bringing the magnitude of this angle closer to the observed $\eta = \pm 20°$ and $\pm 30°$ range. However, because the diffraction pattern as a whole exhibits a pseudo-cubic structure throughout the electrical loading range, any rhombohedral distortion of the crystal structure is expected to be vanishingly small. Thus the increased rhombohedral peak splitting observed in Figure 3-11 is somewhat ambiguous. It seems to suggest the presence of regions experiencing rhombohedral

crystal distortions, but the expected magnitude of these distortions appear to contradict the whole-pattern Rietveld results indicating an average cubic symmetry.

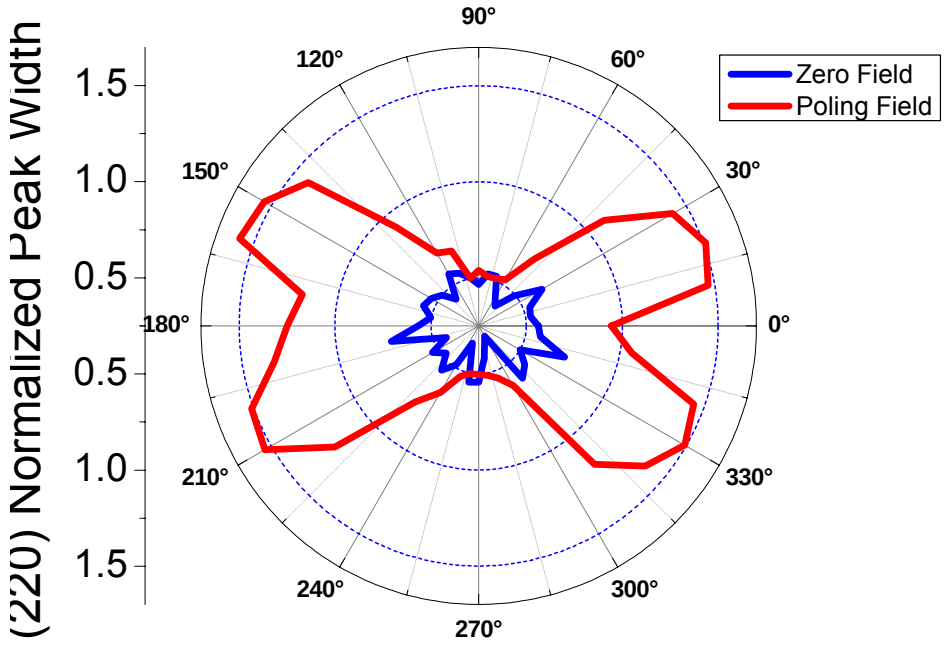


Figure 3-11: Distribution of (220) peak widths as a function of angle with respect to the electric field (η) measured at zero field (inner curve) and the maximum poling field (~0.9 kV/mm, outer curve).

For the case of the $(200)_C$ peak, a rhombohedral transformation would not be expected to induce peak splitting. Our data confirm that no shoulder or splitting occurred for the $(200)_C$ diffraction peak (not shown), but instead a general broadening of the peak width with increased electric field was observed. Figure 3-12 displays the angular structure of the peak broadening observed in the $(200)_C$ reflection before and after poling. $(200)_C$ peak broadening may also be visualized using the crystallography of a rhombohedral unit cell, in which the $(200)_C \rightarrow (20\bar{4})_R$. Again assuming a vanishingly small rhombohedral distortion approaching the cubic approximation, the angle between

the $(200)_C$ and the $(111)_C$ lattice planes would be ~ 55°. As $[111]_C$ dipoles aligned with the electric field direction along η = 0°, the $\{204\}_R$ family of planes would lie at locations of approximately η = 55°, 125°, 235°, and 305°. While these values are in the vicinity of the angular peak width maxima observed in Fig 3-12, here again we do not observe strict correspondence. Additionally, in this case if there were any rhombohedral distortions of the unit cell it would be expected to reduce the magnitude of the angle between the $(200)_C$ and the $(111)_C$, pushing the theoretical location of maximum broadening further from the observed ~ ±60° from the electric field axis.

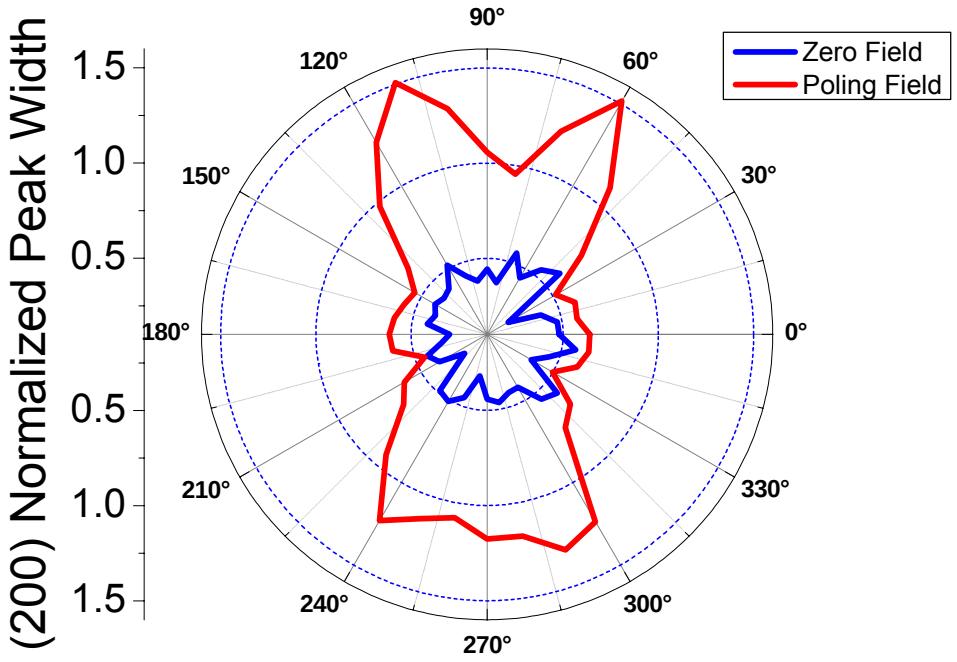


Figure 3-12: Distribution of (200) peak widths as a function of angle with respect to the electric field (η) measured at zero field (inner curve) and the maximum poling field (~0.9 kV/mm, outer curve).

It is thus difficult to attribute dog-bone shapes in Figs. 3-11 and 3-12 strictly to the development of macroscopic rhombohedral domains. As mentioned above, no rhombohedral phase strain behavior or texture development was observed in the whole-pattern Rietveld analysis, or the single peak position and intensity results. The single peak width data are understandable, however, as the development of "tweed" microstructure from a nanodomain matrix. The tweed microstructure is known to exist for the composition 7/65/35 PLZT at room temperature. In rhombohedrally ordered materials, tweed domains have been observed to form boundaries parallel to the [110] and [100] pseudo-cubic crystal directions [8]. The reason for the increased peak widths of the $(220)_C$ and $(200)_C$ reflections at high electric fields may be due to an asymmetric strain process occurring in directions corresponding to tweed domain wall orientations. While any significant and consistent rhombohedral distortion of the crystal structure would be expected to have effects on the entire diffraction pattern (not observed), an asymmetric strain process active only in relation to tweed domain walls may selectively broaden the $(220)_C$ and $(200)_C$ peaks.

Tweed domain structures exhibit periodicity on the order of tens of nanometers [8], thus distinguishing between the crystal variants using a macroscopic X-ray probe is impossible. Because the X-ray beam is so large, structural distortions (strains) occurring over tweed domain length scales would present a small continuum of lattice parameters and thus broaden X-ray diffraction peaks significantly along the direction of modulation. Randall reports that in PLZT, tweed structures are induced parallel with $(110)_C$ planes, and elongation of TEM diffraction spots in directions perpendicular to the planes (along the direction of modulation) [8]. The data shown in Fig. 3-11 are consistent then, with

Randall's results, in that we observe a generalized broadening of the $(220)_C$ diffraction peaks corresponding to the formation of tweed microstructure as a result of applied electric load. An analogous argument may be formed for the $(200)_C$ peak width data in Fig. 3-12.

### 3.3 Conclusions

High-energy synchrotron radiation was used to study the the *in situ* biaxial bulk crystallographic behavior of a polycrystalline PLZT composition under electrical loading at room temperature. Structural analysis indicated that the material exhibited pseudo-cubic symmetry. Despite the shortcomings of the cubic approximation (namely peak intensity errors), significant two-dimensional data for the strain response under electrical loading were obtained through the use of 36 virtual detectors. Multiple poling curves and butterfly loops may be simultaneously measured using this experimental design.

Single peak analysis indicated that the macroscopic material response was neither strictly cubic nor rhombohedral in nature. Significant asymmetries were observed in strain response relative to the pseudo-cubic description (Fig. 3-8 a and 3-9). Measuring the changes in certain peak widths as a function of electric field seemed to indicate the development of tweed microstructure from a nanodomain state. Still, it is only possible to speculate whether the geometrical shape of the single peak width results can be directly correlated to the micromechanics of tweed formation. Without direct measurements of tweed orientation distributions and periodicity, it is impossible to discern the effects of intrinsic tweed properties from any effects they may have on the constitutive response of a sample under electrical field.

**Chapter References**


1. Dai, X.H., Z. Xu, J.F. Li, and D. Viehland, *Effects of Lanthanum Modification on Rhombohedral Pb($Zr_{1-x}Ti_x$)$O_3$ Ceramics .1. Transformation from Normal to Relaxor Ferroelectric Behaviors.* Journal of Materials Research, 1996. **11**(3): p. 618-625.

2. Li, J.F., X.H. Dai, A. Chow, and D. Viehland, *Polarization Switching Mechanisms and Electromechanical Properties of La-Modified Lead-Zirconate-Titanate Ceramics.* Journal of Materials Research, 1995. **10**(4): p. 926-938.

3. Tan, Q. and D. Viehland, *AC-Field-Dependent Structure-Property Relationships in La- Modified Lead Zirconate Ritanate: Induced Relaxor Behavior and Domain Breakdown in Soft Ferroelectrics.* Physical Review B, 1996. **53**(21): p. 14103-14111.

4. Teslic, S., T. Egami, and D. Viehland, *Local Atomic Structure of PZT and PLZT Studied by Pulsed Neutron Scattering.* Journal of Physics and Chemistry of Solids, 1996. **57**(10): p. 1537-1543.

5. Egami, T., S. Teslic, W. Dmowski, D. Viehland, and S. Vakhrushev, *Local Atomic Structure of Relaxor Ferroelectric Solids Determined by Pulsed Neutron and X-ray Scattering.* Ferroelectrics, 1997. **199**(1-4): p. 103-113.

6. Xu, Z., M.C. Kim, J.F. Li, and D. Viehland, *Observation of a Sequence of Domain-Like States with Increasing Disorder in Ferroelectrics.* Philosophical Magazine a-Physics of Condensed Matter Structure Defects and Mechanical Properties, 1996. **74**(2): p. 395-406.

7. Dai, X.H., Z. Xu, and D. Viehland, *The Spontaneous Relaxor to Normal Ferroelectric Transformation in La-Modified Lead-Zirconate-Titanate.* Philosophical Magazine B-Physics of Condensed Matter Statistical Mechanics Electronic Optical and Magnetic Properties, 1994. **70**(1): p. 33-48.

8. Randall, C.A., D.J. Barber, and R.W. Whatmore, *Insitu TEM Experiments on Perovskite-Structured Ferroelectric Relaxor Materials.* Journal of Microscopy-Oxford, 1987. **145**: p. 275-291.

9. Akbas, M.A., I.M. Reaney, and W.E. Lee, *Domain Structure-Property Relations in Lead Lanthanum Zirconate Titanate Ceramics.* Journal of Materials Research, 1996. **11**(9): p. 2293-2301.

10. Xi, Y., C. Zhili, and L.E. Cross, *Polarization and Depolarization Behavior of Hot Pressed Lead Lanthanum Zirconate Titanate Ceramics.* Journal of Applied Physics, 1983. **54**(6): p. 3399-3403.

11. Viehland, D., Z. Xu, and D.A. Payne, *Origin of F Spots and Stress Sensitivity in Lanthanum Lead Zirconate Titanate.* Journal of Applied Physics, 1993. **74**(12): p. 7454-7460.

12. El Marssi, M., R. Farhi, J.L. Dellis, M.D. Glinchuk, L. Seguin, and D. Viehland, *Ferroelectric and Glassy States in La-Modified Lead Zirconate Titanate Ceramics: A General Picture.* Journal of Applied Physics, 1998. **83**(10): p. 5371-5380.

13. Viehland, D., S.J. Jang, and L.E. Cross, *Internal Strain Relaxation and the Glassy Behavior of La-Modified Lead Zirconate Titanate Relaxors.* Journal of Applied Physics, 1991. **69**(9): p. 6595-6602.

14. Dai, X., Z. Xu, and D. Viehland, *Long-Time Relaxation From Relaxor to Normal Ferroelectric States in $Pb_{0.91}La_{0.06}(Zr_{0.65}Ti_{0.35})O_3$.* Journal of the American Ceramic Society, 1996. **79**(7): p. 1957-1960.

15. Dai, X.H., Z. Xu, J.F. Li, and D. Viehland, *Field-Induced Strains and Polarization Switching Mechanisms in La-Modified Lead Zirconate Ttitanate Ceramics.* Journal of Applied Physics, 1996. **79**(4): p. 2023-2028.

16. Keve, E.T. and K.L. Bye, *Phase Iidentification and Ddomain Structure in PLZT Ceramics.* Journal of Applied Physics, 1974. **46**(2): p. 810-818.

17. Michel, C. and Sicignan.A, *Observation of Field-Induced Microstructure in Beta Phase of 8/65/35 PLZT Electrooptic Ceramics.* Applied Physics Letters, 1974. **24**(11): p. 559-562.

18. Hammersley, A.P., *Fit2D*, Grenoble, France, 1987.

19. Rietveld, H.M., *A Profile Refinement Method for Nuclear and Magnetic Structures.* Journal of Applied Crystallography, 1969. **2**: p. 65-&.

20. Larson, A.C. and R.B. Von Dreele, *GSAS: General Structure Analysis System*. 1986: Los Alamos National Laboratory, Report No. LAUR 86-748.

21. Jaffe, B., W.R. Cook, and H. Jaffe, *Piezoelectric Ceramics*. 1971, London: Academic Press.

22. Haertling, G.H. and C.E. Land, *Hot-Pressed $(Pb,La)(Zr,Ti)O_3$ Ferroelectric Ceramics for Electooptic Applications.* Journal of the American Ceramic Society, 1971. **54**(1): p. 1-11.

23. Gupta, S.M., J.F. Li, and D. Viehland, *Coexistence of Relaxor and Normal Ferroelectric Phases in Morphotropic Phase Boundary Compositions of*

*Lanthanum-Modified Lead Zirconate Titanate.* Journal of the American Ceramic Society, 1998. **81**(3): p. 557-564.

24. Lynch, C.S., *The Effect of Uniaxial STress on The Electro-Mechanical Response of 8/65/35 PLZT.* Acta Material, 1996. **44**(10): p. 4137-4184.

25. Viehland, D. and Y.H. Chen, *Random-Field Model for Ferroelectric Domain Dynamics and Polarization Reversal.* Journal of Applied Physics, 2000. **88**(11): p. 6696-6707.

26. Jullian, C., J.F. Li, and D. Viehland, *Polarization Dynamics Over Broad Time and Field Domains in Modified Ferroelectrics.* Applied Physics Letters, 2003. **83**(6): p. 1196-1198.

# Chapter 4

## Microscopic Single-Crystal Experiments

### 4.0 Introduction: Scanning X-ray Microdiffraction of Single-Crystal $BaTiO_3$

Chapters 2 and 3 dealt with macroscopic average behavior of ferroelectrics to applied mechanical and electrical loads. On the most basic level, polycrystals are composed of single-crystal grains which possess different domain variants. It is well known that the application of mechanical stress or electric field can alter the domain structure in ferroelectrics [1-6]. Indeed, the constitutive behavior of a ferroelectric is largely governed by the formation, movement and interaction of its domains. It is desireable, then, to understand the microscopic strain effects related to domain wall formation and interaction. Studies have shown that large strains (up to 0.8%) can be induced in $BaTiO_3$ single-crystals by activating 90° domain switching [1, 4]. Additionally, crystals with engineered domain configurations exhibit high piezoelectric responses [3]. For these reasons, $BaTiO_3$ ceramics are a good candidate for sensor and actuator applications. However, $BaTiO_3$ is susceptible to fatigue and cracking under cyclic electromechanical loading, which currently limits its incorporation into such devices [1, 4]. Therefore, the successful application of $BaTiO_3$ as well as other ferroelectrics requires a detailed understanding of the micromechanics of its domains and their effect on internal stresses, in addition to their influence on fatigue and damage evolution.

Ferroelectric domains have been observed using various techniques including transmission electron microscopy (TEM) [7], optical microscopy [8] and atomic force microscopy (AFM) [2, 7, 9, 10]. Models of 90° domain boundaries based on X-ray diffraction and high-resolution TEM (HRTEM) have been proposed [11]. TEM and HRTEM methods are hindered by the necessity for extremely thin sample dimensions, and offer limited quantification of strain. Although AFM studies have been successful in outlining the extent of polarization variations across domain boundaries, they offer no information on the value and distribution of lattice strain. Studies using optical birefringence [11-13] have been more promising in this regard, because they yielded some local strain data around domains. Although they offer good spatial resolution, birefringence experiments are only applicable to transparent specimens, and rely on a set of assumptions to obtain a strain value indirectly. Moreover, they cannot distinguish tensile from compressive strain. X-ray diffraction avoids these pitfalls and yields a direct measure of strain by tracking changes in the lattice constants of a crystal. Synchrotron X-ray diffraction has been used to image domains by topography [14] and phase contrast [15]. However, no direct measurement of the strain field around a ferroelectric domain has been previously performed.

In this chapter it will be demonstrated that the emerging technique of scanning X-ray microdiffraction [16] is aptly suited to study the microscopic strain states associated with domain configurations in single-crystal $BaTiO_3$. The local triaxial strain fields around 90° domains in single-crystal $BaTiO_3$ are reported [17]. Specifically, residual strain maps in a region surrounding an isolated, approximately 40 μm wide, 90° domain were obtained with 3 μm resolution, revealing significant residual strains. Additionally,

separate measurements of the domain configuration and three-dimensional strain fields formed during indentation-induced fracture in this material are presented. This information is critical for developing accurate micromechanical modeling of domain behavior in ferroelectrics.

### 4.1 Scanning X-ray Microdiffraction Experimental Technique

All scanning X-ray microdiffraction (μSXRD) experiments were performed at end station 7.3.3 of the Advanced Light Source (ALS) at the Lawrence Berkeley National Laboratory (Berkeley, USA). μSXRD at the ALS employs a polychromatic "white" X-ray beam consisting of X-rays at medium energies (5–14 keV). These X-ray energies assured that in single-crystal $BaTiO_3$, 99% of the diffraction data will originate from an approximately 70 μm deep layer beneath the sample surface [18]. Such penetration depths are several orders of magnitude larger than those achievable by electron microscopy and yield data less influenced by surface effects. The white X-ray beam is micro-focused using two Kirkpatrick-Baez (K-B) mirrors to a final size approaching 1 $\mu m^2$ (Figure 4-1). The sample is placed at a 45° angle with respect to the incoming beam, so that diffraction occurs in reflection mode. In the case of a single-crystal sample, the range of X-ray energies produces a Laue pattern projected 90° from the incoming beam. This Laue pattern is recorded on a CCD camera (Bruker 6000, with an active area of 90 x 90 $mm^2$), and subsequently imported into the custom written X-ray Microdiffraction Analysis Software (XMAS) [16, 19].

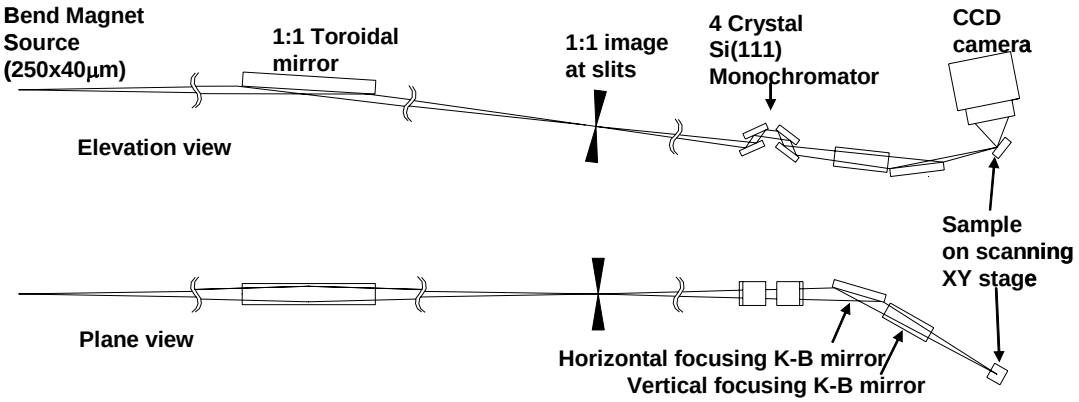


Figure 4-1: Schematic of microdiffraction Endstation 7.3.3 at the ALS (Courtesy of N. Tamura). For polychromatic radiation mode, monochromater is removed.

The XMAS package is a multifunctional analysis tool designed specifically for the interpretation of microdiffraction data. The basic function of the software in the context of these experiments was to calculate the strained lattice parameters observed in Laue patterns recorded from various locations of $BaTiO_3$ specimens. This requires a precise calibration of experimental geometry, which XMAS also accomplishes. For detailed information on the underlying mathematical basis, computational implementation, and wide variety of available tools not used in the reported experiments, the interested reader is referred to the thesis of B.C. Valek [20] and the original technique development work at Oak Ridge National Laboratory [21-23]. Once strained lattice parameter values have been established, it is possible to calculate the three-dimensional *deviatoric* portion of the strain tensor (Figure 4-2) in the local crystal coordinate system [20]. It is important to note that only the deviatoric portion of the strain tensor can be calculated by the relative angular differences between diffraction spots in a Laue pattern. Because these Laue patterns are produced by white beam radiation, volumetric changes

in the unit cell alter the specific X-ray energies which contribute intensity to a diffraction spot, but not the relative positions of the recorded reflections (thus a unit cell defined by $a_1$ x $a_2$ x $a_3$ will have a Laue pattern identical to a unit cell of $2a_1$ x $2a_2$ x $2a_3$). In order to interpret the microdiffraction data, the volumetric (dilatational) contribution to the strain tensor is removed using the following formalism:

$$\varepsilon_{ij} = \begin{pmatrix} \varepsilon'_{11} & \varepsilon_{12} & \varepsilon_{13} \\ \varepsilon_{21} & \varepsilon'_{22} & \varepsilon_{23} \\ \varepsilon_{31} & \varepsilon_{32} & \varepsilon'_{33} \end{pmatrix} + \begin{pmatrix} \delta & 0 & 0 \\ 0 & \delta & 0 \\ 0 & 0 & \delta \end{pmatrix} \tag{4.1}$$

$$\text{where} \quad \delta = \frac{\varepsilon_{11} + \varepsilon_{22} + \varepsilon_{33}}{3} \tag{4.2}$$

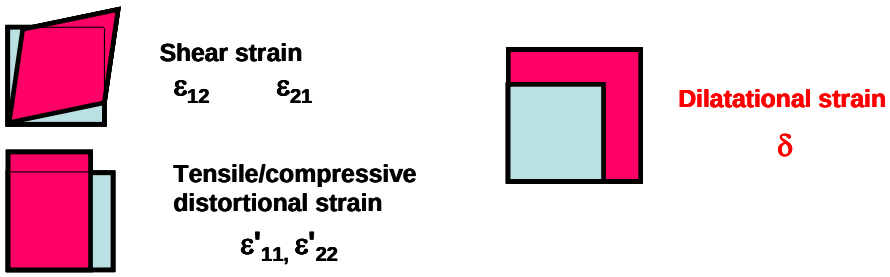


Figure 4-2: Deviatoric and volumetric (dilatational) strain components in a 2-D unit cell (courtesy of N. Tamura).

In tandem with the deviatoric strain calculation, crystal orientation with respect to the laboratory coordinate system is calculated. With the crystal orientation and deviatoric strain in the crystal coordinate system known, the strain tensor can be mapped to the laboratory coordinate system, yielding a real space representation for the strains in the sample. The final results of interest to this study are the in-plane and out-of-plane crystal orientation, along with the deviatoric strain components measured in the laboratory frame (Figure 4-3).

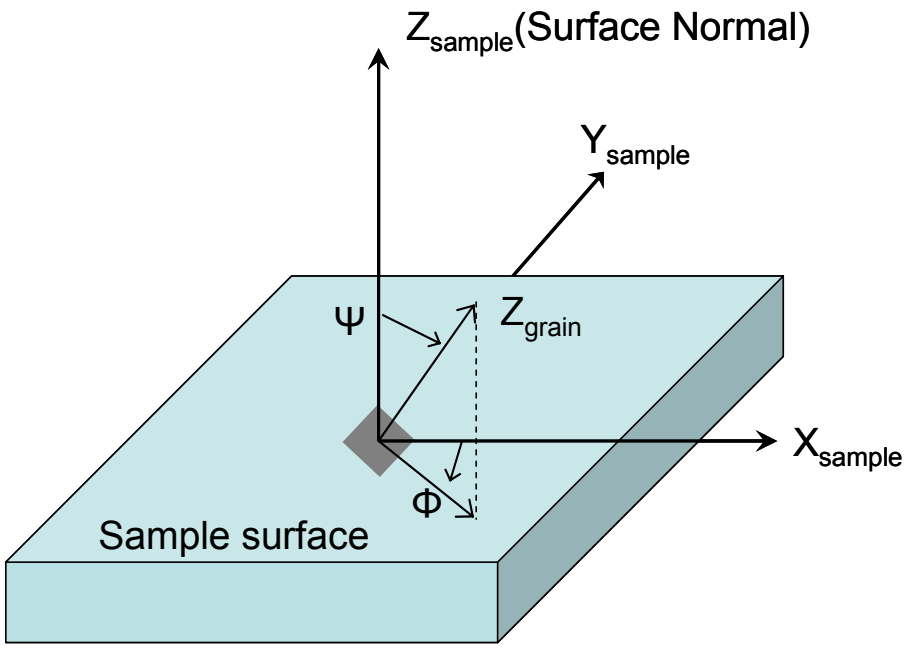


Figure 4-3: Initial deviatoric strain calculations are performed in the coordinate system of the local crystal (e.g., $Z_{grain}$). Using the measured crystal orientation (Ψ, Φ), strain results are transformed from the crystal coordinate system to the laboratory coordinate system (X,Y,Z)

## 4.2 μSXRD Investigation of a Single Domain in $BaTiO_3$

### 4.2.1 Experimental Details

The present study used a single-crystal of $BaTiO_3$ obtained from the MTI Corporation (Richmond, California 94804, USA). The sample measured 5 x 5 x 1 $mm^3$, and was grown in the [001] orientation (normal parallel with the short sample dimension). Its purity was 99.99%, and had a density of 6.02 g $cm^{-3}$. Both of its (001) faces were polished to a final roughness of less than 15 Å. The presence of 90° domains was confirmed with polarized light microscopy prior to μSXRD studies. The sample was mounted on a translation stage with its (001) face at an angle of ~45° with respect to the horizontal incident beam. Figure 4-4 shows the laboratory coordinate system and its orientation with respect to the $BaTiO_3$ single-crystal axes. Here, *z* is the normal direction

to the sample surface and *x* and *y* are the in-plane orthogonal directions. At each *x*-*y* position, the crystal was exposed to X-rays for 1 second. The reflection Laue patterns produced by the polychromatic radiation were recorded using the CCD detector.

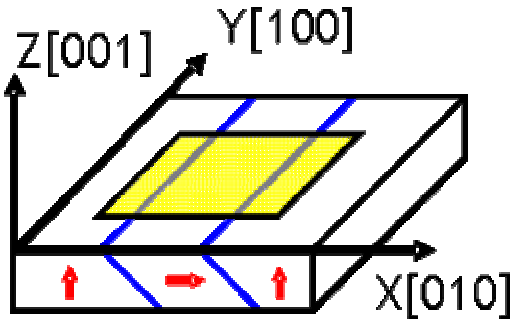


Figure 4-4: Single-crystal orientation of the $BaTiO_3$ sample. Solid lines indicate domain walls, arrows show the direction of unit cell polarizations (along *c* direction), and outlined area delineates scanned region.

Geometrical calibration parameters (sample-to-detector distance, CCD center positions, detector pitch and yaw) were determined by using a section of the $BaTiO_3$ crystal far from any domain boundary, a region that also served as a reference for strain calculations. In this experiment, literature values of the $BaTiO_3$ lattice constants at room temperature were assumed for calibration and strain analysis [24]: $a$ = 3.9947 Å and $c$ = 4.0336 Å. After several indexation and subsequent calibration refinement cycles, the final geometrical calibration parameters were obtained. It is important to note that the assumption of literature values for the strain free lattice constants has a direct impact on strain results. This will be discussed in more detail below.

After calibration was complete, preliminary line scans across small regions of the sample were performed to locate regions of interest. As a result, an isolated, approximately 40 μm wide 90° domain was identified in the crystal with its *c* axis parallel to sample surface (an "*a*"domain). As depicted schematically in Figure 4-4, this

*a* domain was surrounded by a "matrix" region where the *c* axis was perpendicular to sample surface (a "*c*"domain). A two-dimensional scan of the area around this isolated domain was performed (Fig. 4-4). Step sizes in both the *x* and *y* directions were 3 μm and the total scanned area measured 150 x 200 $\mu m^2$. The indexation of the Laue patterns showed that the *c* domain had a crystal orientation of approximately [010]|| *x*, [100] || *y*, and [001] || *z*, whereas the *a* domain had the approximate orientation of [001] || *x*, [100] || *y*, and [010] || *z* (The reader should note the usual 180° ambiguity in diffraction data when interpreting these results). The exact value of the angular separation between the *c* axes in both domains was 88.5°, which compares well to the theoretical value of $2\tan^{-1}(a/c) = 89.4°$ (calculated using the lattice constants given above).

### 4.2.2 Results and Discussion

Figure 4-5 a is a three-dimensional representation of the local distribution of the deviatoric component of the residual strain tensor along the *x* axis ( $\varepsilon'_{xx}$) obtained from the two-dimensional scan of the top surface. The maximum observed residual strain ($\varepsilon'_{xx}$) at the domain boundary exceeded 0.15%. This strain remains substantial inside the *a* domain, indicating that the domain itself is under a general tensile stress. The peak strains observed upon "entering" and "exiting" the domain reached different values, creating an asymmetric shape. In general, this profile exhibited minimal variation parallel to the domain boundaries on the sample surface (that is, along the *y* axis). By integrating the strain results along the *y* axis, an average profile of the strain variation across the domain can be constructed (Figure 4-5 b). The asymmetry of the *y*-integrated profile was also observed in line scans of other domains in this and other samples (data

not shown). However, this asymmetry was not always present, nor was it always in the same direction across domain boundaries. Its physical cause is undocumented in previous literature and currently unknown to the author. The often observed surface relief that accompanies 90° domains [2, 25] may have an influence on this strain asymmetry.

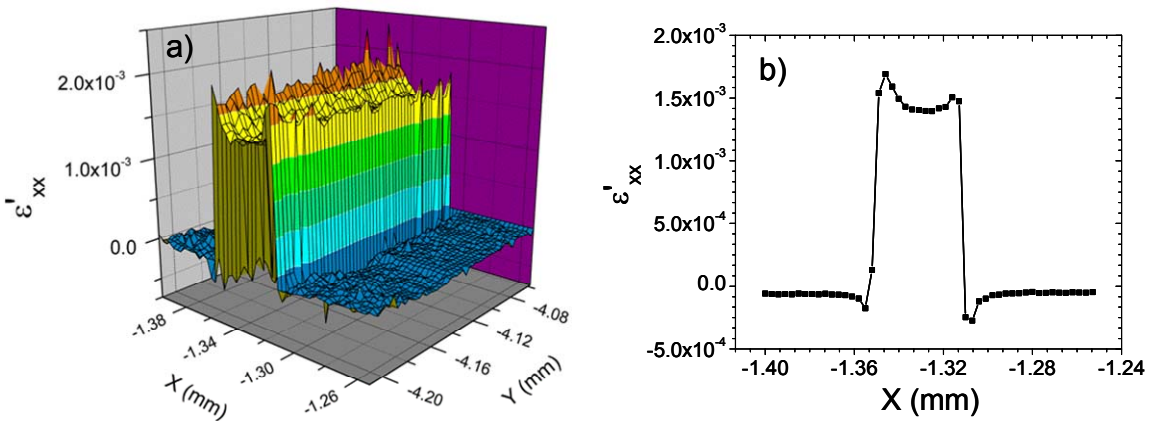


Figure 4-5: Variation of $\varepsilon'_{xx}$ around a single 90° domain in $BaTiO_3$. a) Two-dimensional variation; b) y-integrated average. The least-squares fitting routine estimated a typical strain error of about $10^{-5}$ for all strain data.

The only other deviatoric strain-tensor components that displayed significant values above noise levels for this domain were the normal component $\varepsilon'_{zz}$ and the shear component $\varepsilon'_{xy}$. Their *y*-integrated strain profiles along the *x* axis are displayed in Figure 4-6 a and b, respectively. It is seen that strain along *z* is negative corresponding to compression within the *a* domain. Slight asymmetry can also be seen in this profile. The shear strain is positive inside the *a* domain and negative around the domain boundaries. Asymmetry along the *x* direction is not noted at the domain walls, however there is an additional third asymmetric peak centered at x = -1.32 mm which makes the profile asymmetric as a whole. The author believes that this extra feature in the shear data may be tied to the asymmetry of the normal strain components, although the details of these relationships are not well understood at this time. Preliminary modeling of a similar

domain structure using the energy minimization method largely confirmed the observed strain state (positive $\varepsilon'_{xx}$ and negative $\varepsilon'_{zz}$) [26]. However, the origin of the strain asymmetry is remains unexplained by these calculations, and the shear strain profile could not be reproduced.

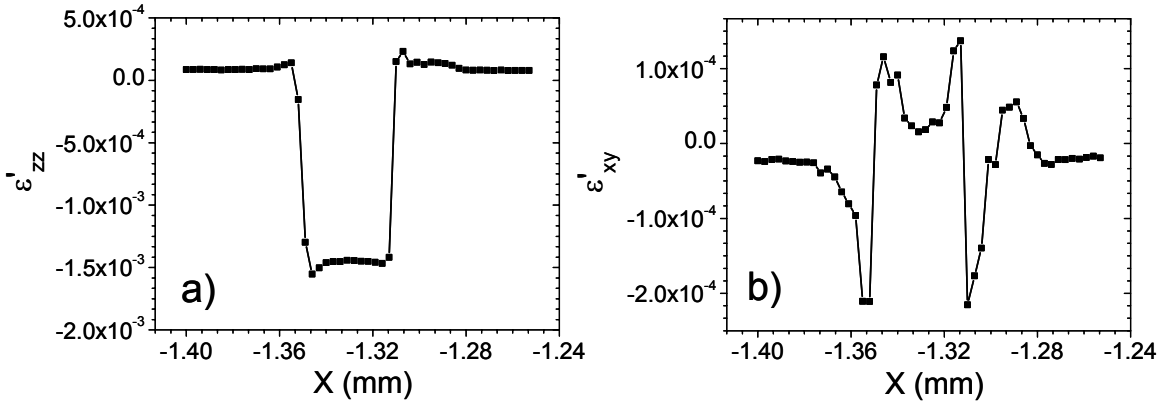


Figure 4-6: y-integrated average of the two strain components in the same region as in Fig. 4-5. a) $\varepsilon'_{zz}$ (along surface normal; b) $\varepsilon'_{xy}$ (in-plane shear). Note that the strain axis in (b) is different than in (a).

As mentioned previously, the assumption of literature values for the strain free lattice parameters has a direct impact on the reported strains, i.e., the assumption of different strain free lattice parameters would produce different magnitudes in the measured strains. In order to surmount this uncertainty, an accurate measurement of the sample lattice parameters must be performed. Recently developed μSXRD methods have addressed this need, and preliminary experiments exploiting this development have been performed but will not be reported here. Still, assuming literature lattice parameters allows for the quantification of three-dimensional strain and orientation within single-crystal ferroelectrics. These values are of specific interest to the ferroelectrics fracture community, as ferroelastic switching and the piezoelectric effect can have significant

impacts on crack propagation. The next section describes a μSXRD experiment designed to gain insight into fracture processes in ferroelectric materials.

### 4.3 Introduction: Indentation-Induced Fracture in Single-crystal $BaTiO_3$

A significant liability in using ferroelectric ceramics for structural applications is their inherent brittleness. The lack of fracture resistance in ferroelectrics leads to cracking at electrode interfaces, within ceramic layers, and near electrode tips. In the absence of applied electric fields the Mode I fracture toughness for most PZT ferroelectric ceramics is on the order of $K_{Ic} \approx 1$ MPa$\sqrt{m}$ [27-30]. Electrical coupling further complicates the situation, as the application of modest electric fields to ferroelectrics can reduce or increase measured fracture toughness levels by as much as 30%, while remanent polarizations induce fracture toughness anisotropy [31-33].

In the same way that plasticity and other irreversible deformation mechanisms increase the fracture toughness of materials, it can be argued that domain switching is responsible for the fracture toughness anisotropy in ferroelectrics. Recently, several studies have focused on the use of indentation techniques to induce cracks into polycrystalline piezoelectric specimens to investigate this anisotropy (see [34] for a review). Without the influence of grain boundaries and resulting residual stresses, single-crystals offer clear information on fracture toughness of anisotropic materials [35]. A few experiments are noted which applied indentation techniques to analyze fracture processes in single-crystal ferroelectrics [35-38]. Of particular interest to the current investigation is the initial work of Busche and Hsia examining Vickers indentation induced fracture in single-crystal $BaTiO_3$ [35], and subsequent experiments by Fang and

Yang probing the influence of poling direction on indentation fracture behavior [36]. Both of these studies clearly demonstrate that the fracture resistance in $BaTiO_3$ is anisotropic, and indicate that domain switching occurs in order to accommodate fracture induced stresses. In order to fully understand fracture mechanisms in ferroelectrics and formulate successful models for predicting crack behavior, it is critical that the strains associated with fracture processes be understood.

The following section details a first of its kind investigation applying μSXRD to the study of indentation induced strain and fracture in single-crystal $BaTiO_3$. By mimicking the indentation geometry of previous studies [35, 36], complementary high resolution data for the crystal orientation and deviatoric strains due to the fracture process are presented.

## 4.4 μSXRD Study of Indentation Induced Fracture in Single-Crystal $BaTiO_3$

### 4.4.1 Experimental Considerations

Single-crystal $BaTiO_3$ was obtained from the MTI Corporation (Richmond, California, 94804, USA). The specimen measured 10x10x1 $mm^3$, and was grown in the [100] orientation (normal parallel with the short sample dimension). Its purity was 99.99% and had density of 6.02 g $cm^{-3}$. Both of the (100) faces were polished to a final roughness of less than 15 Å. The sample initially consisted almost entirely of a large, single-domain region. Vickers indentation was performed using a 200 g load applied with a total contact time of ~10 s. The indentor's diagonals were macroscopically aligned with the [010] and [001] crystal axes [35]. SEM (LEO 1550VP FESEM, Oxford EDS) and

polarized light optical analysis confirmed the successful initiation of fracture in regions surrounding the indentation.

The sample was mounted on a translation stage at ALS end station 7.3.3 (stepping resolution < 1 μm) with its (100) surface at an angle of ~45° to the incident beam. The sample was rastered under white beam illumination over an area of 300 x 300 $\mu m^2$ surrounding the indentation, using a step size of 5 μm. At each position, the sample was exposed to X-rays for 1 s. The reflection Laue patterns produced by the polychromatic radiation were recorded using a CCD detector (Bruker 6000, active area of 90 x 90 $mm^2$). The data were analyzed using the XMAS software package [16, 19]. Experimental geometry was calibrated using a single-crystal pattern obtained far from the Vickers indentation, in a nominally strain free region. Literature values of the $BaTiO_3$ lattice constants were assumed to define the strain free condition [24]: $a$ = 3.9947 and $c$ = 4.0336 Å.

Figure 4-7 displays a SEM image of the indentation and surrounding region. The square perimeter of the indentation measured approximately 22 μm on a side, yielding an indentation depth of roughly 15.6 μm. Four prominent cracks emanate from the two of the indentation corners, while much shorter cracks emanate from the remaining corners. Two of these longer cracks span a length of approximately 280 μm, while the opposite pair spans only 205 μm. Near the indentation on the interior of both sets of long cracks, significant surface deformation was noted in both SEM and optical analysis (not shown in detail). This is from the process known as “pile-up”, which results from the displacement of material within the indentation zone to regions above the original surface height [39].

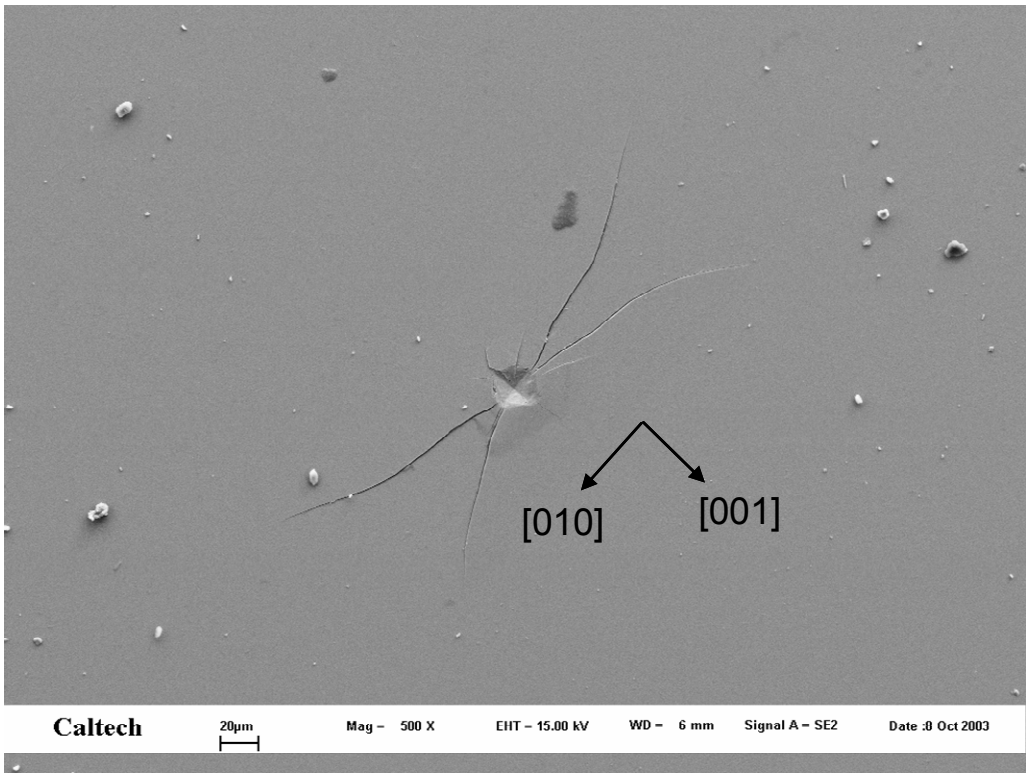


Figure 4-7: SEM image of the Vickers indentation zone.

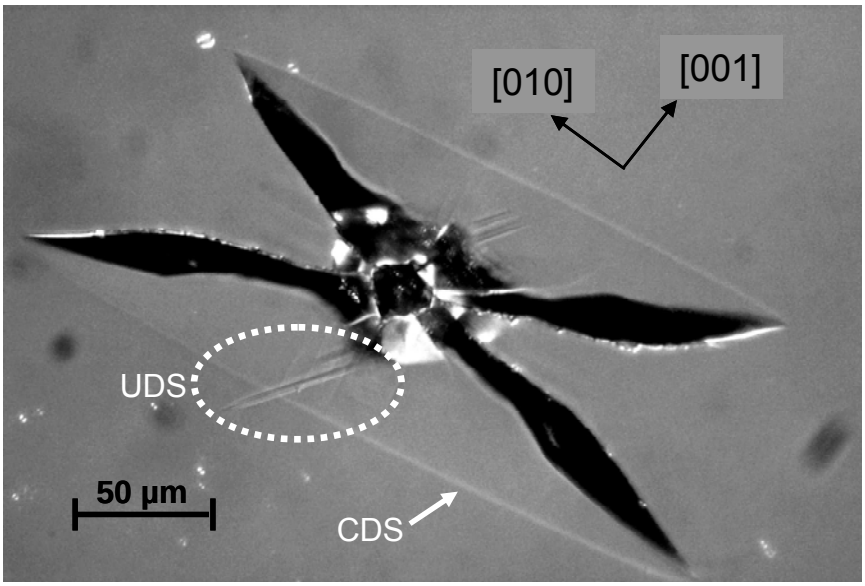


Figure 4-8: Polarized light microscopy image of the indentation zone formed from a 200g load. Dark areas are indentation and resulting crack surfaces. Fine lines of lighter contrast indicate 90° domain switching.

Figure 4-8 shows a polarized light microscopy image of the indentation zone, which bears a strong resemblance to the results of previous studies [35, 36]. Note the fine parallel lines on the interior area of the long cracks at 45° to the diagonal of the indentation (parallel to the <110> crystal directions). These are attributed to "unconventional" 90° domain switching (UDS) [35, 36]. Additional contrast in the optical images is noted along the [010] crystal direction, as fine lines connecting the tips of the long cracks. Fang *et al* used etching techniques to demonstrate that this contrast is attributable to subsurface conventional domain switching (CDS) several μm beneath the crystal surface [36]. The unconventional/conventional designation refers to the specific geometry of domain wall formation with reference to the macroscopic bulk crystal orientation. CDS in a (100) grown $BaTiO_3$ crystal (direction normal to crystal surface, such as the one used in this experiment) repositions the polarization in an anti-plane orientation, exchanging, for example, the [100] direction for the [001] direction ([*hkl*] → [*lkh*]). The boundaries formed by this type of domain switching insure that neighboring domains are in a low-energy electrostatic configuration, with polarization rotations conforming to head-to-tail ordering (Figure 4-9). The isolated domain examined in Section 4.2 was produced by conventional domain switching.

UDS, on the other hand, reorients the polarization within the surface plane, implying that the [010] direction changes into the [001] direction ([*hkl*] → [*hlk*]) in a [100] grown single-crystal. Because the [010] and [0-10] directions in the crystal are energetically indistinguishable, a 2-D symmetry is available for UDS (Figure 4-9). This implies that regions of oppositely directed polarizations may form and intersect. At these intersections, 180° domain walls separate domains with polarizations in a head-to-head

(or tail-to-tail) arrangement, instead of the lower energy head-to-tail ordering for conventional 90° domain boundaries (Figure 4-9) [36]. UDS regions have been associated with arresting crack development in $BaTiO_3$ [36].

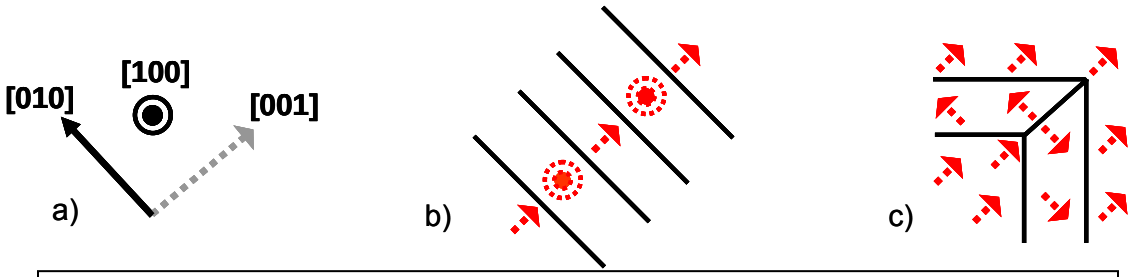


Figure 4-9: Schematic of conventional and unconventional domain switching manifested in the bulk crystal orientation depicted by a). b) Conventional domain switching rotates the polarization direction (dashed line) out of plane, and does not allow for the formation of high energy head-to-head or tail-to-tail domain boundaries. c) Unconventional domain switching rotates the polarization direction in-plane, and can create high energy domain walls.

### 4.4.2 Microdiffraction Results and Discussion

Microdiffraction measurements for the crystal orientation are shown in Figures 4-10 a and b (not in same orientation as SEM image). Figure 4-10 a displays the in-plane (surface parallel) angular orientation of the (001) pole with respect to the laboratory *x*-axis. Note that no significant variations outside of the error level (~0.1°) are observed, and that the crystal lies with its [001] direction at approximately 42.7° to the *x*-direction, implying that the (010) planes lie at an angle of 132.7° as indicated schematically in Figure 4-10 a. Figure 4-10 b displays the out-of-plane (surface normal) orientation of the (100) poles with respect to the laboratory coordinate system. Here we can clearly observe the effects of material pile-up, as near the indentation there is almost a 1° change in the orientation localized in on the interior of the short set of cracks. Additionally, the

cracks relieve sections of crystal, creating the anisotropic crack pattern observed in previous work [35, 36]. Conspicuously absent from presented crystal orientation data is evidence for 90° domain walls in the region of the indentation, despite their identification during optical microscopy analysis.

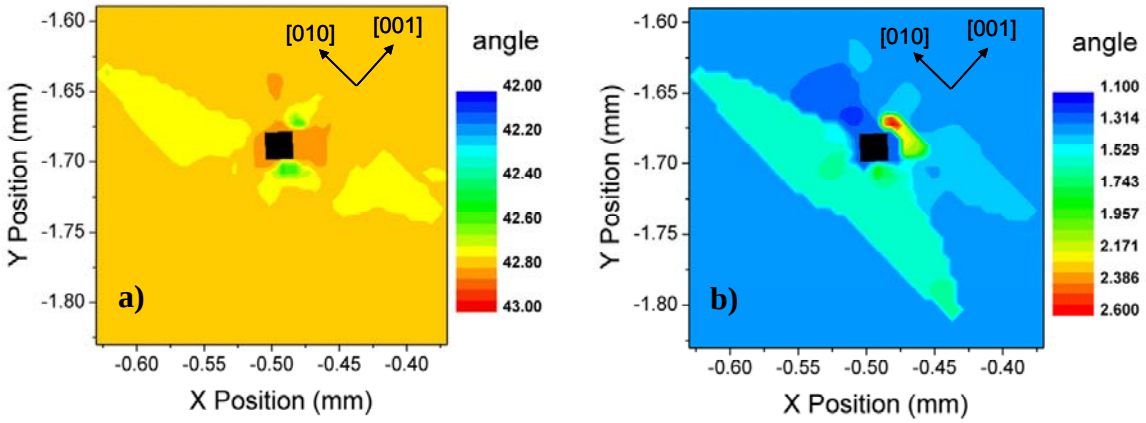


Figure 4-10: a) In-plane orientation of the (001) crystal pole, and b) out-of-plane orientation of the (100) crystal pole. Black squares mark approximate location of the Vickers indentation.

In Section 4.2 it was demonstrated that μSXRD is capable of detecting the orientation and strain differences surrounding 90° domains in single-crystal $BaTiO_3$ [17]. Domain identification is also possible in the case of the indented sample, and is a point which warrants clarification. White beam radiation incident on a single-crystal produces a single reflection for each (*hkl*) plane, i.e., in the resulting Laue pattern a single spot will correspond to a given lattice plane spacing. In the case $BaTiO_3$, the situation is somewhat more complex as the X-ray beam may illuminate multiple domain orientations within the same single-crystal. Thus each domain will contribute its own Laue pattern to the final diffracted image. Due to the small *c*/*a* ratio of $BaTiO_3$ and the 90° orientation difference between domains, the general effect of illuminating two different domains is a

"doubling" of the Laue pattern. Thus when the X-ray beam encounters two domains formed by conventional switching, e.g., the Laue (630) spot from the original domain is accompanied by a nearby (036) spot from the second, switched domain (for unconventional switching the (603) spot is present instead).

While multiple diffraction patterns may be evident for any *x*-*y* location in the scan, a single Laue pattern is chosen by XMAS to represent the general state of the crystal at a single spatial location. This process is automated by the XMAS package, which selects the Laue pattern with the maximum number of identifiable peaks exhibiting the greatest total integrated intensity. Orientation results from these most intense Laue patterns are presented in Figures 4-10 a and b. In the case of our indented specimen, the crystal domain variant corresponding to the bulk crystal orientation always exhibited the strongest diffracted Laue pattern, and as a result only minor orientation changes appear within this domain variant, instead of the drastic 90° fluctuations between different domain variants. Through careful analysis, however, two other distinct sets of Laue spots were identified. By tracking the presence of these spots as a function of *x*-*y* position, information could be gleaned about the domain switching caused by indentation. Specifically, the presence of (036) reflection (conventional switching) and (603) reflection (unconventional switching) were measured.

Figure 4-11 displays the integrated intensity of the (036) peak as a function of scan location. Note that the (036) peak is detected only in regions between the long cracks (forming a "wing-shape"), indicating that CDS has been confined to these areas surrounding the indentation. Because the incident X-ray beam penetrates multiple depths within the crack geometry, several neighboring domain variants may simultaneously

contribute diffracted intensity to the observed pattern. Thus it was not possible to identify the locations of single domain walls or the spacing between domain variants. The presence of the (603) reflection associated with UDS was only observed within the region outlined in Figure 4-11. Diffracted intensities for this peak were very weak, preventing accurate modeling of peaks due to background noise levels. While the area in Figure 4-11 certainly possessed unconventional domains, optical microscopy results suggest that these domain formations are present on both sides of the indentation. It appears that the small volume fraction of unconventional domains does not provide sufficient diffracted intensity in the (603) peak for a completely accurate spatial mapping. Still, UDS was detected in an expected location based on previous studies [35, 36].

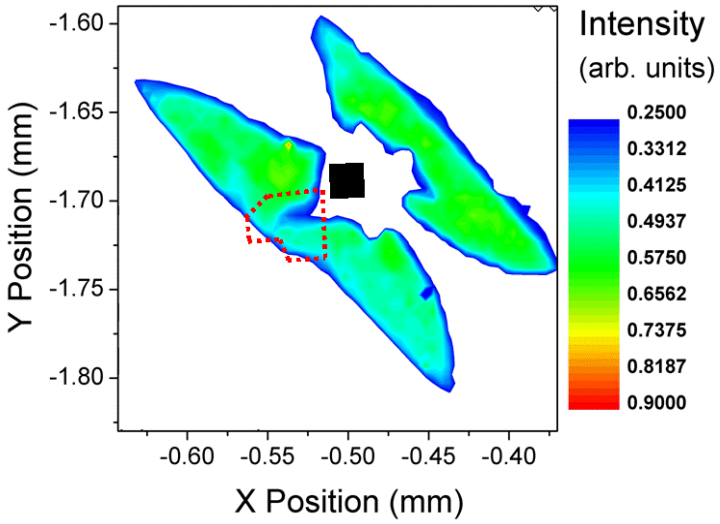


Figure 4-11: Intensity as a function of position for the (036) reflection corresponding to CDS (near zero values have been omitted for clarity). Dotted curve outlines area where (603) reflection corresponding to UDS was detected. Black square indicates approximate location of Vickers indentation.

Deviatoric strain results were calculated for all *x-y* locations in the scan. As noted previously, the bulk crystal domain variant presented the strongest Laue patterns at each scan location. Thus in regions where CDS or UDS were identified, strain results reflect the effects of domain switching on the volume of crystal remaining in the "un-switched" orientation (bulk orientation). Normal deviatoric strain results are plotted in Figures 4-12 a – c. A median smoothing function was applied to the raw strain data to remove outlying values. Both $\varepsilon'_{xx}$ and $\varepsilon'_{yy}$ represent strains in the surface plane of the sample, while $\varepsilon'_{zz}$ measures strain in the direction of the sample surface normal. $\varepsilon'_{zz}$ results indicate tensile strains throughout the CDS region, with almost zero strain observed in the undamaged region (area between wing-shapes). Tensile strain concentrations of at least 2500 με (1 με = $10^{-6}$ strain) for $\varepsilon'_{zz}$ are noted at all four crack initiation sites, with an anomalously high 3500 με concentration occurring at one nucleation area. In areas along the indenter axis parallel to the [001] crystal direction, significant relaxation is observed in the center of the wing-shapes relative to the values observed near crack nucleation sites. For the left wing-shape, this relaxation zone occurs in the same vicinity as UDS. Because both CDS and UDS are present in this region, the strain relaxation suggests that the combined effects of both switching processes may reduce strains relative to regions where only CDS exists. Without a completely accurate mapping of the UDS region, however, rigorous conclusions about the source of the relaxation zone cannot be made. For $\varepsilon'_{xx}$, compressive strains of roughly -800 με appear in all regions relieved by the cracks. Strain concentrations peaking at values of -2000 με are observed near two opposite crack nucleation sites. The $\varepsilon'_{yy}$ results are qualitatively analogous, although the average strain in the wing-shapes is roughly -1000 με, while the remaining opposite two

crack nucleation sites exhibit strain concentrations peaking at -1700 με. All shear strain components ($\varepsilon_{xy}$, $\varepsilon_{xz}$, and $\varepsilon_{yz}$) did not display consistent significant features above noise levels (not shown), though it is possible that shear strains play a more important role for different indentation geometries in single-crystal ferroelectrics [37].

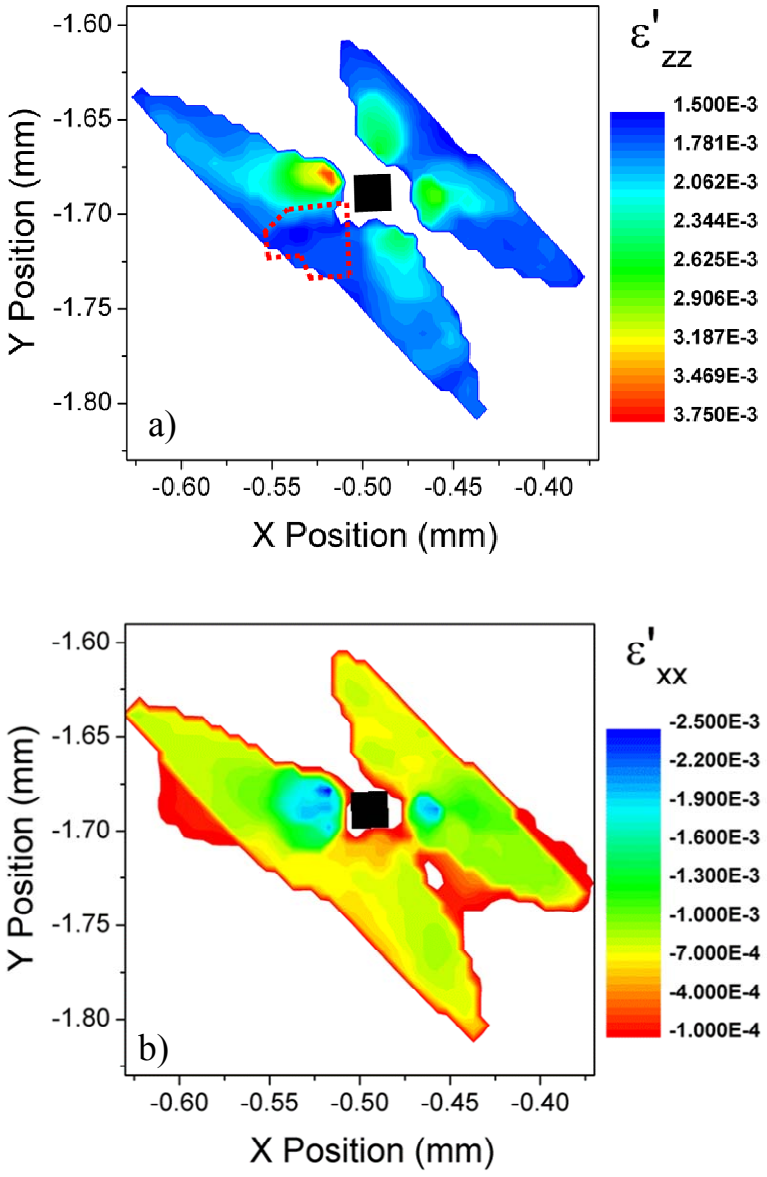


Figure 4-12: a) $\varepsilon'_{zz}$ normal deviatoric strain component measured surrounding the indentation. Near-zero strain levels in the single-crystal region have been omitted for clarity. Relaxation occurs in the left wing-shape in the UDS region (dashed outline). b) $\varepsilon'_{xx}$ and c) $\varepsilon'_{yy}$ results for the same region (following page). Note that the strain scales are different for each plot.

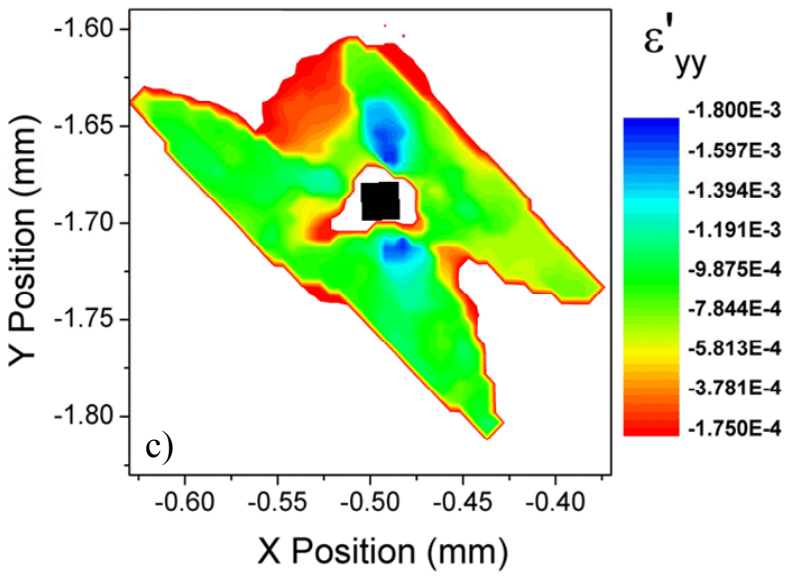


Based on the optical microscopy observations of domain structures in previous studies, it is expected that the indentation will induce both CDS and UDS in order to accommodate compressive stresses within the wing-shapes formed by cracking [35, 36]. While the μSXRD technique applied in this study cannot distinguish between surface or subsurface domain switching, both CDS and UDS were detected and spatially mapped. Deviatoric strain results unambiguously assert the presence of a radial in-plane compressive strain field as a result of the indentation (as evidenced by the similarity in the perpendicular $\varepsilon'_{xx}$ and $\varepsilon'_{yy}$ results) [35]. Naturally, if a radial compressive strain exists for the in-plane direction, then a tensile strain will be induced in the surface normal crystal direction due to the Poisson effect, as confirmed by the the $\varepsilon'_{zz}$ results. The formation of strain concentrations and relaxation zones within the wing-shapes indicates that a complicated stress relief mechanism is at work. This mechanism includes the effects of fracture toughness anisotropy combined with either CDS, UDS, or both.

## 4.5 Conclusions of μSXRD Investigations of Single-crystal $BaTiO_3$

Polychromatic μSXRD provided direct measurements of lattice distortions in the vicinity of 90° domain boundaries in $BaTiO_3$ for the first time. Residual strain fields were observed to extend several micrometers from domain walls, in contrast to both theoretical calculations and TEM measurements, which indicate that the total domain wall width would not exceed 100 Å (12). A previously un-noted asymmetry as a function of position was observed in some components of the deviatoric strain tensor. In the future, it is envisaged that comprehensive μSXRD studies of multiple domains will probe the nature and preponderance of the observed asymmetries, and offer insight into the regulating mechanisms of domain equilibrium near surfaces.

μSXRD studies of Vickers indentation induced fracture in single cyrstal $BaTiO_3$ yielded first-of-their-kind results for the residual strains and domain configurations. Both conventional and unconventional domain switching were detected and mapped in the areas surrounding an indentation site. Significant localization of the deviatoric strain components near crack initiation sites was observed. This localization may be the result of a superposition of the two available domain switching processes (CDS and UDS). Future studies will focus on accurately mapping UDS to form a clear understanding of the stress relief geometry, and measuring the effects of crystal orientation on the indentation fracture process.

**Chapter References**


1. Burcsu, E., G. Ravichandran, and K. Bhattacharya, *Large Strain Electrostrictive Actuation in Barium Titanate.* Applied Physics Letters, 2000. **77**(11): p. 1698-1700.

2. Munoz-Saldana, J., G.A. Schneider, and L.M. Eng, *Stress Induced Movement of Ferroelastic Domain Walls in $BaTiO_3$ Single Crystals Evaluated by Scanning Force Microscopy.* Surface Science, 2001. **480**(1-2): p. L402-L410.

3. Wada, S., S. Suzuki, T. Noma, T. Suzuki, M. Osada, M. Kakihana, S.E. Park, L.E. Cross, and T.R. Shrout, *Enhanced Piezoelectric Property of Barium Titanate Single Crystals With Engineered Domain Configurations.* Japanese Journal of Applied Physics Part 1-Regular Papers Short Notes & Review Papers, 1999. **38**(9B): p. 5505-5511.

4. Jaffe, B., W.R. Cook, and H. Jaffe, *Piezoelectric Ceramics*. 1971, London: Academic Press.

5. Li, X.P., W.Y. Shih, J.S. Vartuli, D.L. Milius, I.A. Aksay, and W.H. Shih, *Effect of a Transverse Tensile Stress on the Electric-Field- Induced Domain Reorientation in Soft PZT: In Situ XRD Study.* Journal of the American Ceramic Society, 2002. **85**(4): p. 844-850.

6. Kim, S., V. Gopalan, and A. Gruverman, *Coercive Fields in Ferroelectrics: A Case Study in Lithium Niobate and Lithium Tantalate.* Applied Physics Letters, 2002. **80**(15): p. 2740-2742.

7. Arlt, G., D. Hennings, and G. Dewith, *Dielectric-Properties of Fine-Grained Barium-Titanate Ceramics.* Journal of Applied Physics, 1985. **58**(4): p. 1619-1625.

8. Merz, W.J., *Domain Formation and Domain Wall Motions in Ferroelectric $BaTiO_3$ Single Crystals.* Physical Review, 1954. **95**(3): p. 690-698.

9. Arlt, G., *Twinning in Ferroelectric and Ferroelastic Ceramics - Stress Relief.* Journal of Materials Science, 1990. **25**(6): p. 2655-2666.

10. Hamazaki, S.I., F. Shimizu, S. Kojima, and M. Takashige, *Afm Observation of 90-Degrees Domains of $BaTiO_3$ Butterfly Crystals.* Journal of the Physical Society of Japan, 1995. **64**(10): p. 3660-3663.

11. Floquet, N., C.M. Valot, M.T. Mesnier, J.C. Niepce, L. Normand, A. Thorel, and R. Kilaas, *Ferroelectric Domain Walls in $BaTiO_3$: Fingerprints in XRPD Diagrams and Quantitative HRTEM Image Analysis.* Journal De Physique Iii, 1997. **7**(6): p. 1105-1128.

12. Yang, T.J. and U. Mohideen, *Nanoscale Measurement of Ferroelectric Domain Wall Strain and Energy by Near-Field Scanning Optical Microscopy.* Physics Letters A, 1998. **250**(1-3): p. 205-210.

13. Yang, T.J., V. Gopalan, P.J. Swart, and U. Mohideen, *Direct Oobservation of Pinning and Bowing of a Single Ferroelectric Domain Wall.* Physical Review Letters, 1999. **82**(20): p. 4106-4109.

14. Kim, S., V. Gopalan, and B. Steiner, *Direct X-ray Synchrotron Imaging of Strains at 180 degree Domain Walls in Congruent $LiNbO_3$ and $LiTaO_3$ Crystals.* Applied Physics Letters, 2000. **77**(13): p. 2051-2053.

15. Hu, Z.W., P.A. Thomas, A. Snigirev, I. Snigireva, A. Souvorov, P.G.R. Smith, G.W. Ross, and S. Teat, *Phase-Mapping of Periodically Domain-Inverted $LiNbO_3$ with Coherent X-rays.* Nature, 1998. **395**(6699): p. 306-306.

16. Tamura, N., R.S. Celestre, A.A. MacDowell, H.A. Padmore, R. Spolenak, B.C. Valek, N.M. Chang, A. Manceau, and J.R. Patel, *Submicron X-ray Diffraction and Its Applications to Problems in Materials and Environmental Science.* Review of Scientific Instruments, 2002. **73**(3): p. 1369-1372.

17. Rogan, R.C., N. Tamura, G.A. Swift, and E. Ustundag, *Direct Measurement of Triaxial Strain Fields Around Ferroelectric Domains Using X-ray Microdiffraction.* Nature Materials, 2003. **2**(6): p. 379-381.

18. Noyan, I.C. and J.B. Cohen, *Residual Stress: Measurement by Diffraction and Interpretation*. 1987, New York: Springer Verlag. 110.

19. Tamura, N., A.A. MacDowell, R. Spolenak, B.C. Valek, J.C. Bravman, W.L. Brown, R.S. Celestre, H.A. Padmore, B.W. Batterman, and J.R. Patel, *Scanning X-ray Microdiffraction with Submicrometer White Beam for Strain/Stress and Orientation Mapping in Thin Films.* J. of Synchrotron Radiat., 2003. **10**: p. 137-143.

20. Valek, B.C., *X-ray Microdiffraction Studies of Mechanical Behavior and Electromigration in Thin Film Structures*. PhD. Thesis, 2003, Stanford University.

21. Tamura, N., J.S. Chung, G.E. Ice, B.C. Larson, J.D. Budai, J.Z. Tischler, M. Yoon, E.L. Williams, and W.P. Lowe, *Strain and Texture in Al Interconnect Wires Measured by X-ray Microbeam Diffraction.* Materials Research Society Symposium Proceedings, 1999. **563**: p. 175-180.

22. Chung, J.S. and G.E. Ice, *Automated Indexing for Texture and Strain Measurement with Broad-Bandpass X-ray Microbeams.* Journal of Applied Physics, 1999. **86**(9): p. 5249-5255.

23. Chung, J.S., N. Tamura, G.E. Ice, B.C. Larson, J.D. Budai, and W.P. Lowe, *X-ray Microbeam Measurment of the Local Texture and Strain in Metals.* Materials Research Society Symposium Proceedings, 1999. **563**: p. 169-174.

24. Wyckoff, R.W.G., *Crystal Structures*. 1964, New York: Wiley.

25. Ganpule, C.S., V. Nagarajan, B.K. Hill, A.L. Roytburd, E.D. Williams, R. Ramesh, S.P. Alpay, A. Roelofs, R. Waser, and L.M. Eng, *Imaging Three-Dimensional Polarization in Epitaxial Polydomain Ferroelectric Thin Films.* Journal of Applied Physics, 2002. **91**(3): p. 1477-1481.

26. Zhang, W. and K. Bhattacharya, Unpublished, 2002.

27. Meschke, F., O. Raddatz, A. Kolleck, and G.A. Schneider, *R-Curve Behavior and Crack-Closure Stresses in Barium Titanate and (Mg,Y)-PSZ Ceramics.* Journal of the American Ceramic Society, 2000. **83**(2): p. 353-361.

28. Heyer, V., G.A. Schneider, H. Balke, J. Drescher, and H.A. Bahr, *A Fracture Criterion for Conducting Cracks in Homogeneously Poled Piezoelectric PZT-PIC 151 ceramics.* Acta Materialia, 1998. **46**(18): p. 6615-6622.

29. Kolleck, A., G.A. Schneider, and F.A. Meschke, *R-Curve Behavior of BaTiO3- and PZT Ceramics under the Influence of an Electric Field Applied Parallel to the Crack Front.* Acta Materialia, 2000. **48**(16): p. 4099-4113.

30. Pohanka, R.C. and P.L. Smith, *Recent Advances in Piezoelectric Cermaics*, in *Electronic Ceramics*. 1998, Marcel Dekker Inc.: New York. p. 45-145.

31. Park, S.B. and C.T. Sun, *Effect of Electric-Field on Fracture of Piezoelectric Ceramics.* International Journal of Fracture, 1995. **70**(3): p. 203-216.

32. Schneider, G.A. and V. Heyer, *Influence of the Electric Field on Vickers Indentation Crack Growth in $BaTiO_3$.* Journal of the European Ceramic Society, 1999. **19**(6-7): p. 1299-1306.

33. Lynch, C.S., *Fracture of Ferroelectric and Relaxor Electro-Ceramics: Influence of Electric Field.* Acta Materialia, 1998. **46**(2): p. 599-608.

34. Shindo, Y., M. Oka, and K. Horiguchi, *Analysis and Testing of Indentation Fracture Behavior of Piezoelectric Ceramics under an Electric Field.* Journal of Engineering Materials and Technology, 2001. **123**: p. 293-300.

35. Busche, M.J. and K.J. Hsia, *Fracture and Domain Switching by Indentation in Barium Titanate Single Crystals.* Scripta Materialia, 2001. **44**(2): p. 207-212.

36. Fang, F. and W. Yang, *Indentation-Induced Cracking and 90 degree Domain Switching Pattern in Barium Titanate Ferroelectric Single Crystals under Different Poling.* Materials Letters, 2002. **57**(1): p. 198-202.

37. Shang, J.K. and X. Tan, *Indentation-Induced Domain Switching in Pb(Mg1/3Nb2/3)O3-PbTiO3 Crystal.* Acta Materialia, 2001. **49**: p. 2993-2999.

38. Park, E.T., J.L. Routbort, Z. Li, and P. Nash, *Anisotropic Microhardness in Single-Crystal and Polycrystalline $BaTiO_3$.* Journal of Materials Science, 1998. **33**(3): p. 669-673.

39. Walls, M.G., M.M. Chaudhri, and T.B. Tang, *STM Profilometry of Low-Load Vickers Indentations in a Silicon Crystal.* Journal of Physics D-Applied Physics, 1992. **25**(3): p. 500-507.

# Chapter 5

## Ongoing Work and Conclusions

### 5.0 Ongoing Investigation: Overview of 3-D XRD Mesoscopic Studies

A recent XRD method (called "3-D XRD") can complement the methods described in previous chapters by probing the *mesoscale* constitutive behavior of ferroelectrics. This method has been pioneered by Dr. H. Poulsen from Risø and is implemented at ESRF Beamline ID-11. Using a focused, monochromatic high energy (e.g., 80 keV) X-ray beam and specialized peak indexing software, this technique is capable of isolating the strain and orientation information of a *single embedded grain* from that of its neighbors [1-5].

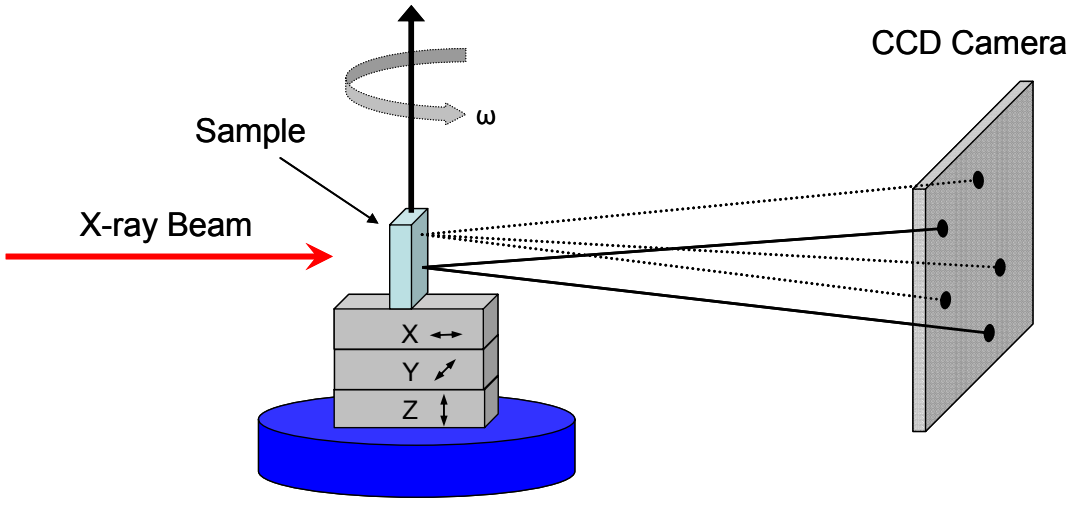


Figure 5-1: Experimental geometry for 3-D XRD experiments at end station ID-11 of the ESRF. The X-ray beam penetrates through the sample, producing diffraction from multiple grains (dotted lines correspond to one grain, solid lines to a second). For the $BaTiO_3$ experiment, electric field was applied along the Y direction, so that when the sample surface is normal to the X-ray beam, the electric field is perpendicular to the transmission axis. Rotations occur about the ω axis, generating a unique spot pattern for each step in ω.

The beam penetrates the whole sample cross section and generates diffraction data from several grains, producing an array of "spots" which are collected on an area detector (Fig. 5-1). Each spot in a single image may come from *separate* grains in the sample. When the specimen is rotated around the $\omega$ axis, some of these spots disappear and others are added as the diffraction conditions for various (*hkl*)'s in different grains are fulfilled. Provided that the $\omega$ angle rotation range is large enough, eventually several diffraction spots from a single grain will be recorded. Using a customized software, GRAINDEX [6], the entire collection of spots from all $\omega$ rotation steps are ray-traced to their point of origin within the specimen. In this way, sets of diffraction spots are identified which originate from the *same* grain within the polycrystal. With the diffraction angle of each spot and its location in the $\omega$ rotation, the orientation of these grains and their relative strain may be calculated. Thus it is possible to measure the three-dimensional strain tensor from individual grains within a polycrystalline sample. This technique can also be used to produce three-dimensional maps of grain boundaries [5].

3-D XRD has so far been used in investigations of deformation in metals. An added complication for ferroelectrics is the presence of domains. However, just like twins, domains yield unique diffraction patterns that can easily be resolved by this method. In a similar fashion to other texture quantifications described in Chapter 2, measuring the relative intensities of certain reflections allows for the quantification of domain variant volume fractions within a single grain. To evaluate the feasibility of 3-D XRD in ferroelectrics research, the author and colleages have performed an experiment on a polycrystalline BTO under electrical loading. For the first time, the *in-situ* evolution

of the volume fractions of domains in an embedded, individual grain as a function of applied electric field was studied. Additionally, the triaxial strain state of each variant can be measured *in situ*. Thus, it will be possible to calculate the critical driving force for activating a given switching system by observing characteristic evolution of strains as a function of applied loading.

The data analysis for this experiment is currently underway. Initial results from the GRAINDEX ray-tracing procedure have already identified several grains which are suitable for full 3-D strain tensor analysis. Figure 5-2 schematically depicts the evolution of a set of diffraction spots from one such grain. Each spot represents one of the domain variants present within grain. Since the sample was poled to –1.0 kV/mm before placing it in the beam, the 0 kV/mm image corresponds to a poled state. Initially, the (200) diffraction spot is of higher intensity, indicating that the majority of domains in this grain are of the *a* type as a result of poling. At 0.23 kV/mm, intensity is quickly reallocated to the (002) spot of the *c* variant, corresponding to domain switching from *a* to *c*. This occurs well below the macroscopic $E_c$ value of this $BaTiO_3$ sample (~ 0.5 kV/mm). It is interesting to note that due to internal stresses around the grain and its specific orientation with respect to the poling field both *a* and *c* variants are always present, i.e., the grain is never completely poled so as only to possess a single domain variant. Also note that the relative positions of the diffraction peaks change with electric field. This is a direct result of lattice strain evolution under electric field. These preliminary observations verify the power of 3-D XRD for quantifying constitutive behavior in ferroelectrics. Single grains within a ferroelectric polycrystal can be unambiguously located by this technique. Additionally, changes in the volume fraction of domain variants within a grain and

effects of the strain evolution resulting from domain switching under electrical loading can be measured. When full analysis of these data is complete, it is expected that ~50 grains within the material will be isolated for full strain tensor and domain fraction measurements. From these grains we will be able to determine the relationship between orientation within the polycrystal and ferroelectric switching behavior. This information is crucial to multiaxial models for ferroelectric behavior, and has been previously unattainable.

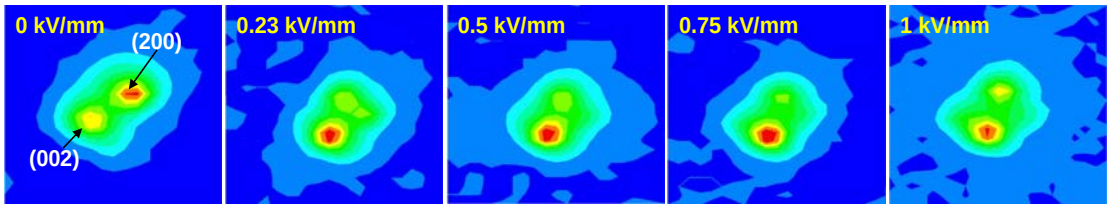


Figure 5-2: Raw diffraction data for a single embedded grain of BTO within a polycrystalline specimen under electrical load.

## 5.1 Summary of Results and Conclusions

The first experiments presented in Chapter 2 were studies of the *in situ* response of several PZT compositions to mechanical stress. A neutron diffraction technique was employed which allowed for the simultaneous measurement of material texture (domain switching) and crystal lattice strains in directions parallel and transverse to the loading axis [7]. By comparing the behaviors of single phase tetragonal, single phase rhombohedral, and dual phase morphotropic compositions, information concerning the intergranular micromechanics was inferred. Specifically, in the morphotropic ceramics, the addition of rhombohedral grains in the tetragonal grain matrix softens the switching

threshold for both phases, allowing for significant domain alignment during application of electric field. Additionally, the tetragonal phase likely experiences internal load transfer from switched domains to pinned domains, as evidenced by temporary softening in the *c* axis of the pinned domains. It is also possible that internal loads produced by tetragonal phase domain switching are also transferred to the rhombohedral phase domains, consequently lowering the macroscopic load threshold to induce switching of rhombohedral domains relative to their single phase counterparts. The result is that the morphotropic composition exhibits superior piezoelectric qualities compared to either of the single phase compositions.

In an effort to probe more of the multiaxial constitutive behavior (i.e., the average effects of grain orientation on ferroelectric response), a high-energy X-ray diffraction experiment was presented in Chapter 3. A complicated PLZT relaxor material was chosen for this work. Using transmission geometry and a 2-D image plate detector, complete Debye rings could be captured representing the crystallographic state of all grains lying in a sample plane. By creating "virtual detectors", these Debye rings could be broken down to study 36 different directions of sample behavior simultaneously. The specimen was then poled *in situ* using high electric fields, and subsequently cycled through positive and negative electric fields. Diffraction results indicated an overriding pseudo-cubic structure consistent with the presence of nano- or tweed domains throughout the electrical cycling procedure, with no development of long range ferroelectric order observed. A total of 36 butterfly loops were recorded for the electrical field cycle (using the pseudo-cubic approximation), representing a complete two-dimensional data set of the ferroelectric constitutive behavior. Individual peak fitting

yielded angularly dependant peak widths exhibiting symmetry with respect to the applied electric field. These peak width results seem to indicate the development of tweed domains from a nanodomain initial state, which is in general agreement with several previous studies.

Chapter 4 focused on a polychromatic X-ray diffraction technique capable of measuring the full three-dimensional strain tensor in single crystal and large grained materials. Experiments in this chapter used single crystal specimens of BTO. One investigation yielded the first ever direct measurement of the tri-axial strain fields associated with single domain walls in ferroelectrics [8]. Significant residual strains were observed for three of the deviatoric strain tensor components, each of which displayed unexpected asymmetric profiles.

The second investigation recorded the domain switching mechanisms activated to accommodate indentation-induced fracture stresses. Both conventional and unconventional domain switching were successfully detected in the vicinity of the indentation. Strain results indicated significant strain concentrations near crack nucleation sites, and relaxation zones between sites. The presence of both conventional and unconventional domain switching in the relaxations zones suggests that the interplay of these two mechanisms may provide significant stress relief and contribute to the fracture toughness anisotropy of $BaTiO_3$.

Chapters 2 and 3 dealt with multiaxial ferroelectric constitutive behavior on a *macroscopic* scale (or polycrystalline average). Chapter 4 presented data from a completely *microscopic* scale (or single domain variant behavior). In order to complete the continuum of length scales, information at the *mesoscale* of individual grains and

grain-to-grain interactions is needed. The 3-D XRD technique described in Section 5.1 will bridge this mesoscale gap. Preliminary work indicates that this technique will allow unprecedented access to intergranular interactions, i.e., the stochastic effects of grain orientation and neighborhood on constitutive behavior. Including this final section, the experimental methods described in this thesis provide access to *two-dimensional and three-dimensional multiaxial* constitutive strain behavior in ferroelectrics for each of the *microscopic, mesoscopic, and macroscopic* length scales. Results from each of these length scales will provide critical validation data for models attempting to accurately describe the behavior of ferroelectric materials.

**Chapter References**

1. Margulies, L., G. Winther, and H.F. Poulsen, *In Situ Measurement of Grain Rotation During Deformation of Polycrystals.* Science, 2001. **291**(5512): p. 2392-2394.

2. Margulies, L., T. Lorentzen, H.F. Poulsen, and T. Leffers, *Strain Tensor Development in a Single Grain in the Bulk of a Polycrystal Under Loading.* Acta Materialia, 2002. **50**(7): p. 1771-1779.

3. Poulsen, H.F., S.F. Nielsen, E.M. Lauridsen, S. Schmidt, R.M. Suter, U. Lienert, L. Margulies, T. Lorentzen, and D.J. Jensen, *Three-Dimensional Maps of Grain Boundaries and the Stress State of Individual Grains in Polycrystals and Powders.* Journal of Applied Crystallography, 2001. **34**: p. 751-756.

4. Poulsen, H.F., E.M. Lauridsen, S. Schmidt, L. Margulies, and J.H. Driver, *3D-Characterisation of Microstructure Evolution During Annealing of a Deformed Aluminum Single Crystal.* Acta Materialia, 2003. **51**(9): p. 2517-2529.

5. Poulsen, H.F. and X. Fu, *Generation of Grain Boundary Maps by an Algebraic Reconstruction Technique.* Journal of Applied Crystallography, 2003. **36**(4): p. 1062-1068.

6. Lauridsen, E.M., S. Schmidt, R.M. Suter, and H.F. Poulsen, *Tracking: A Method for Stuctural Characterization of Grains in Powders and Polycrystals.* Journal of Applied Crystallography, 2001. **34**: p. 744-750.

7. Rogan, R.C., E. Ustundag, B. Clausen, and M.R. Daymond, *Texture and Strain Analysis of the Ferroelastic Behavior of Pb(Zr,Ti)O-3 by In Situ Neutron Diffraction.* Journal of Applied Physics, 2003. **93**(7): p. 4104-4111.

8. Rogan, R.C., N. Tamura, G.A. Swift, and E. Ustundag, *Direct Measurement of Triaxial Strain Fields around Ferroelectric Domains using X-ray Microdiffraction.* Nature Materials, 2003. **2**(6): p. 379-381.